Article

IL-1β$^+$ macrophages fuel pathogenic inflammation in pancreatic cancer

https://doi.org/10.1038/s41586-023-06685-2

Received: 12 December 2022

Accepted: 27 September 2023

Published online: 1 November 2023

Check for updates

Nicoletta Caronni[1,14]✉, Federica La Terza[1,14], Francesco M. Vittoria[1,2,14], Giulia Barbiera[1,14], Luca Mezzanzanica[1,2], Vincenzo Cuzzola[1,2], Simona Barresi[1], Marta Pellegatta[3], Paolo Canevazzi[3], Garett Dunsmore[4], Carlo Leonardi[1], Elisa Montaldo[1], Eleonora Lusito[1], Erica Dugnani[5], Antonio Citro[5], Melissa S. F. Ng[6], Marco Schiavo Lena[3], Denise Drago[7], Annapaola Andolfo[7], Silvia Brugiapaglia[8], Alessandro Scagliotti[8], Alessandra Mortellaro[1], Vincenzo Corbo[9], Zhaoyuan Liu[10], Anna Mondino[3], Paolo Dellabona[3], Lorenzo Piemonti[2,5], Carla Taveggia[3], Claudio Doglioni[2,3], Paola Cappello[8], Francesco Novelli[8], Matteo Iannacone[2,3], Lai Guan Ng[11], Florent Ginhoux[4,6,10,12], Stefano Crippa[2,13], Massimo Falconi[2,13], Chiara Bonini[2,3], Luigi Naldini[1,2], Marco Genua[1] & Renato Ostuni[1,2]✉

Pancreatic ductal adenocarcinoma (PDAC) is a lethal disease with high resistance to therapies[1]. Inflammatory and immunomodulatory signals co-exist in the pancreatic tumour microenvironment, leading to dysregulated repair and cytotoxic responses. Tumour-associated macrophages (TAMs) have key roles in PDAC[2], but their diversity has prevented therapeutic exploitation. Here we combined single-cell and spatial genomics with functional experiments to unravel macrophage functions in pancreatic cancer. We uncovered an inflammatory loop between tumour cells and interleukin-1β (IL-1β)-expressing TAMs, a subset of macrophages elicited by a local synergy between prostaglandin E_2 (PGE_2) and tumour necrosis factor (TNF). Physical proximity with IL-1β$^+$ TAMs was associated with inflammatory reprogramming and acquisition of pathogenic properties by a subset of PDAC cells. This occurrence was an early event in pancreatic tumorigenesis and led to persistent transcriptional changes associated with disease progression and poor outcomes for patients. Blocking PGE_2 or IL-1β activity elicited TAM reprogramming and antagonized tumour cell-intrinsic and -extrinsic inflammation, leading to PDAC control in vivo. Targeting the PGE_2–IL-1β axis may enable preventive or therapeutic strategies for reprogramming of immune dynamics in pancreatic cancer.

The diverse functions of macrophages in tissue homeostasis, immunity and cancer underlie plastic adaptations to environmental cues via the selection of genomic programmes by lineage-determining and stimulus-responsive transcription factors[3,4]. TAMs are relevant targets in immune oncology, as their abundance generally correlates with resistance to therapy, metastasis and poor survival. However, single-cell RNA-sequencing (scRNA-seq) studies have shown that TAMs are highly heterogenous and include subsets with diverse ontogenies, functions and therapeutic potentials[2]. Furthermore, macrophage activities are under local influence by cellular, physical and chemical interactions within tissue niches[5].

In tumours, protective immunity triggered by sensing of cell death and danger-associated molecular patterns (DAMPs) co-exists with programmes that suppress cytotoxic responses and that stimulate tissue repair[6]. Exposure to these complex mixtures of signals in the tumour microenvironment (TME) underlies recurrent findings that rather than mirroring in vitro activation states, TAMs co-express genes encoding immune stimulatory, suppressive and reparative factors[7–9]. The pancreatic TME is enriched in factors that hamper the recruitment and/or activation of dendritic cells, cytotoxic natural killer (NK) cells and T lymphocytes[10]. By contrast, PDAC is infiltrated by resident and monocyte-derived TAMs that differentially fuel inflammation, angiogenesis and aberrant matrix deposition[11,12].

Inflammatory programmes can functionally cooperate with oncogenic mutations to increase the risk of cancer development[13]. For instance, inflammatory responses to pancreatic injury trigger persistent epigenetic changes in epithelial cells that underlie non-resolving metaplasia and accelerated tumorigenesis upon subsequent *Kras* activation[14,15].

[1]San Raffaele Telethon Institute for Gene Therapy (SR-Tiget), IRCCS San Raffaele Scientific Institute, Milan, Italy. [2]Vita–Salute San Raffaele University, Milan, Italy. [3]IRCCS San Raffaele Scientific Institute, Milan, Italy. [4]INSERM U1015, Gustave Roussy Cancer Campus, Université Paris-Saclay, Villejuif, France. [5]Diabetes Research Institute (DRI), IRCCS San Raffaele Scientific Institute, Milan, Italy. [6]Singapore Immunology Network (SIgN), A*STAR, Singapore, Singapore. [7]Center for Omics Sciences (COSR), IRCCS San Raffaele Scientific Institute, Milan, Italy. [8]Department of Molecular Biotechnology and Health Sciences, University of Turin, Turin, Italy. [9]University of Verona, Verona, Italy. [10]Shanghai Institute of Immunology, Department of Immunology and Microbiology, Shanghai Jiao Tong University School of Medicine, Shanghai, China. [11]Shanghai Immune Therapy Institute, Renji Hospital, Shanghai Jiao Tong University School of Medicine, Shanghai, China. [12]Translational Immunology Institute, SingHealth/Duke-NUS Academic Medical Centre, Singapore, Singapore. [13]Pancreas Translational and Clinical Research Center, IRCCS San Raffaele Scientific Institute, Milan, Italy. [14]These authors contributed equally: Nicoletta Caronni, Federica La Terza, Francesco M. Vittoria, Giulia Barbiera. ✉e-mail: caronni.nicoletta@hsr.it; ostuni.renato@hsr.it

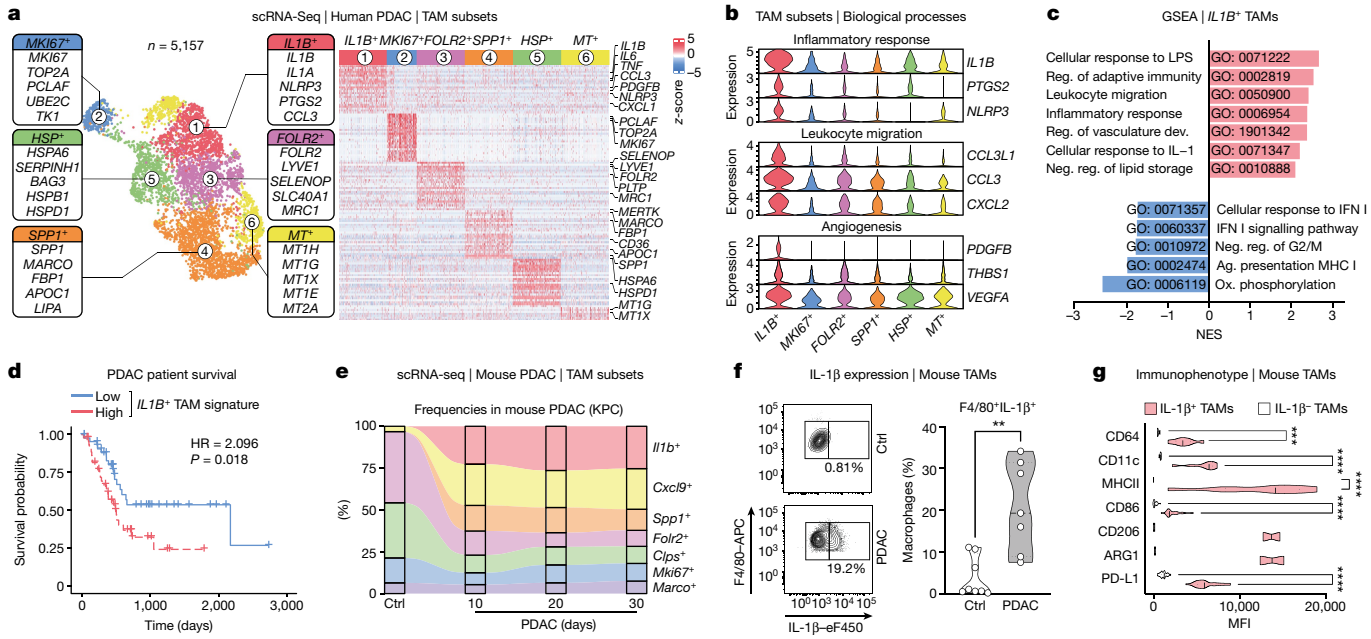

Fig. 1 | *IL1B*$^+$ TAMs correlate with poor prognosis in human PDAC and are conserved in mouse models. a, Uniform manifold approximation and projection (UMAP) of scRNA-seq data from TAMs from patients with PDAC ($n = 10$) (left) and heat map of scaled expression of the top 25 marker genes for each TAM cluster (right). Colours and numbers indicate scRNA-seq clusters. **b**, Expression (scRNA-seq) of selected genes belonging to the indicated categories in TAM subsets. **c**, Gene set enrichment analysis (GSEA) (GO biological processes) on genes ranked by $\log_2$ fold change between *IL1B*$^+$ TAMs and other TAM clusters. NES, normalized enrichment score. Ag., antigen; Dev., development; neg., negative; ox., oxidative; reg., regulation. **d**, Survival probability of patients with PDAC (from TCGA data) stratified by expression levels of the *IL1B*$^+$ TAM gene signature, normalized by *CD68*. Hazard ratio (HR) and *P* value of Cox regression fit are shown. **e**, Frequencies from scRNA-seq data of TAM subsets from control pancreas (Ctrl) and PDAC (orthotopic KPC) at the indicated time points. **f**, Contour plots (left) and frequency (right) of IL-1β$^+$ macrophages from control pancreas ($n = 8$) or PDAC (orthotopic KPC) ($n = 7$). Two-tailed Student's *t*-test. **g**, Expression (flow cytometry staining) of CD64, CD11c and MHCII ($n = 8$), CD206 and ARG1 (n = 2) and CD86 and PD-L1 ($n = 27$) within IL-1β$^+$ (red) and IL-1β$^-$ (white) TAMs (in subcutaneous KPC). Two-way ANOVA. MFI, median fluorescence intensity. $^*P < 0.05$, $^{**}P < 0.01$, $^{***}P < 0.001$ and $^{****}P < 0.0001$.

Here, we set out to elucidate the cellular and molecular determinants of pathogenic inflammation in pancreatic cancer.

Identification of IL-1β$^+$ TAMs in PDAC

We performed scRNA-seq of freshly dissociated tumour samples from naive or chemotherapy-treated patients with PDAC (Supplementary Table 1). The dataset contained 59,569 single-cell transcriptomes spanning tumour, epithelial, stromal and immune compartments across patients and treatments (Extended Data Fig. 1a,b and Supplementary Table 1). Sub-clustering of mononuclear phagocytes (MNPs) uncovered subsets of TAMs whose relative abundance and gene expression programmes were largely conserved between naive and chemotherapy-treated patients (Fig. 1a and Extended Data Fig. 1c–h). *SPP1*$^+$ TAMs expressed lipid metabolism (*FBP1* and *APOC1*) and phagocytic receptor (*MARCO* and *MERTK*) genes, corresponding to previously described populations[7–9]; *FOLR2*$^+$ TAMs expressed non-canonical myeloid marker (*LYVE1* and *SELENOP*) genes and matched resident macrophages[11,16]; other clusters of TAMs expressed metallothionein (*MT1G*, *MT1X* and *MT1E*), heat-shock protein (*HSP*) or cell cycle (*TOP2A* and *MKI67*) genes (Fig. 1a, Extended Data Fig. 1i and Supplementary Table 1). Our analysis uncovered *IL1B*$^+$ TAMs, a subset of PDAC macrophages whose transcriptome was enriched in inflammatory response (*IL1B*, *TNF*, *NLRP3* and *PTGS2*), leukocyte recruitment (*CXCL1*, *CXCL2* and *CCL3*) and angiogenesis (*VEGFA*, *THBS1* and *PDGFB*) programmes but depleted of interferon response and antigen presentation Gene Ontology (GO) terms (Fig. 1b,c and Supplementary Table 1). We next computed gene signatures for TAM subsets by selecting marker genes in scRNA-seq data and filtering out non-MNP-specific transcripts. Expression of the *IL1B*$^+$ TAM signature in RNA-sequencing (RNA-seq) data from The Cancer Genome Atlas (TCGA) was associated with poor patient survival, but not with overall macrophage abundance (Fig. 1d, Extended Data Fig. 1j and Supplementary Table 1). Re-analysis of bulk[17] and scRNA-seq data showed up-regulation of the *IL1B*$^+$ TAM gene signature in blood monocytes from patients with PDAC, although at lower levels than in tumour-infiltrating cells (Extended Data Fig. 1k). These data uncover *IL1B*$^+$ TAMs as a subset of PDAC macrophages expressing inflammatory and non-cytotoxic programmes, whose abundance correlates with poor prognosis.

IL-1β$^+$ TAMs are conserved in mouse PDAC

We performed longitudinal scRNA-seq analyses on blood, pancreas, and tumours isolated from an orthotopic model of pancreatic cancer[18] (*Kras*$^{G12D/+}$*Trp53*$^{R172H/+}$ *Pdx1*$^{cre/+}$, hereafter referred to as KPC) (Extended Data Fig. 2a–c and Supplementary Table 2). Annotation of macrophage transcriptomes revealed broad mouse–human conservation of marker genes and transcriptional programmes of *Il1b*$^+$ TAMs as well as of *Folr2*$^+$, *Spp1*$^+$ and *Mki67*$^+$ TAMs (Extended Data Fig. 2d–f and Supplementary Table 2). These subsets were consistently identified by scRNA-seq in orthotopic or subcutaneous *Kras*$^{G12D/WT}$*Pdx1*$^{cre/WT}$ (hereafter KC) models, or in autochthonous tumours from KPC mice (Extended Data Fig. 2g and Supplementary Table 2). Having observed an early and persistent accumulation of *Il1b*$^+$ TAMs in mouse PDAC (Fig. 1e), we set out to characterize the phenotype of these cells. In keeping with scRNA-seq analyses, IL-1β was expressed by a subset of TAMs in PDAC but not by pancreatic macrophages from control mice (Fig. 1f). Mouse IL-1β$^+$ TAMs expressed CD64, CD11c, major histocompatibility complex class II (MHCII) and the costimulatory molecules CD80 and CD86, together with markers of immune dysfunction in cancer such as CD206, arginase

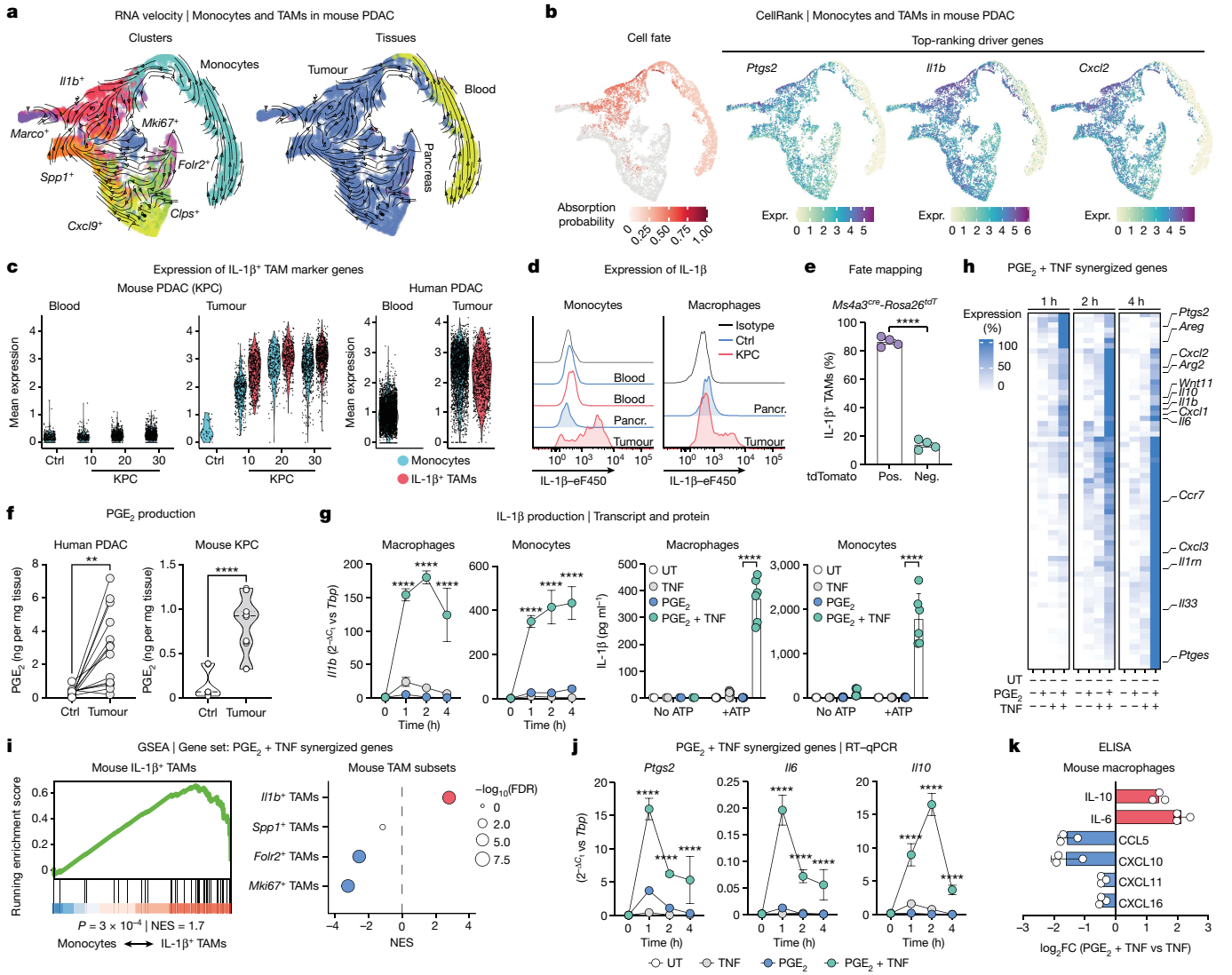

Fig. 2 | PGE$_2$ and TNF cooperatively elicit the IL-1β$^+$ TAM state. a, RNA velocity vectors of macrophages and monocytes from blood, pancreas and PDAC (orthotopic KPC) on *t*-distributed stochastic neighbour embedding. Colours indicate cluster (left) or tissue (right) identity. **b**, Absorption probability towards *Il1b*$^+$ TAMs (left) and expression (expr.) of top-ranking driver genes of the monocyte-to-*Il1b*$^+$ TAM trajectory (right). **c**, Expression (scRNA-seq) of IL-1β$^+$ TAM marker genes in monocytes and IL-1β$^+$ TAMs from control pancreas and PDAC (orthotopic KPC) at the indicated time points (left) or in human monocytes and IL-1β$^+$ TAMs from blood and tumour samples of patients with PDAC (right). **d**, Expression (intracellular staining) of IL-1β in monocytes and macrophages from blood, pancreas (pancr.) and PDAC (orthotopic KPC, end stage) of control (blue) or tumour-bearing (red) mice. **e**, Frequencies (mean ± s.e.m.) of tdTomato$^+$ and tdTomato$^-$ IL-1β$^+$ TAMs from PDAC (orthotopic KPC, end stage, $n = 4$). Unpaired Student's two-tailed *t*-test. Pos., positive. **f**, Quantification of PGE$_2$ in human PDAC ($n = 14$) and normal adjacent tissue (Ctrl) ($n = 14$) by enzyme-linked immunoassay (ELISA) (left; paired Student's two-tailed *t*-test) or mouse control pancreas ($n = 3$) and PDAC (orthotopic KPC, end stage) ($n = 5$) (mass spectrometry) (right; unpaired Student's two-tailed *t*-test). **g**, Transcript (left; $n = 3$) or protein (ELISA) (right; $n = 6$) expression (mean ± s.d.) of IL-1β in BMDMs or bone marrow monocytes. Two-way ANOVA. UT, untreated. **h**, Relative expression of genes synergized by PGE$_2$ plus TNF (Methods) in BMDMs. **i**, GSEA of genes synergized by PGE$_2$ plus TNF, on genes ranked by correlation with absorption probability of the monocyte-to-*Il1b*$^+$ TAM trajectory (left) or genes ranked by log$_2$ fold change between TAM subsets versus other TAMs (right). FDR, false discovery rate. **j**, Expression of the indicated genes (mean ± s.d.) in BMDMs ($n = 3$). Two-way ANOVA. **k**, Quantification (ELISA; mean ± s.d.) of the indicated proteins in the supernatant of BMDMs ($n = 3$), shown as log$_2$ fold change (FC) of concentration values following treatment with PGE$_2$ plus TNF versus TNF only.

1 (ARG1) and the immune checkpoint inhibitor PD-L1 (Fig. 1g and Extended Data Fig. 2h). Thus, IL-1β$^+$ TAMs are a conserved macrophage population that co-expresses inflammatory and immune inhibitory markers.

A monocytic origin of IL-1β$^+$ TAMs

Data from scRNA-seq of mouse monocytes and macrophages from blood, pancreas and tumours were integrated and subjected to optimal transport analysis to infer ancestor–descendant relationships[19]. We found that IL-1β$^+$ TAMs had a higher probability of being derived from monocytes than bona fide resident *Clps*$^+$ or *Folr2*$^+$ macrophages (Extended Data Fig. 3a–j). CellRank analyses[20] also uncovered a trajectory linking tumour-infiltrating monocytes and IL-1β$^+$ TAMs, with key marker genes of IL-1β$^+$ TAMs (*Il1b*, *Ptgs2* and *Cxcl2*) driving the predicted transition (Fig. 2a,b, Extended Data Fig. 3k and Supplementary Table 3). Monocytes entering the tumour readily up-regulated these transcripts and progressively acquired IL-1β$^+$ TAM identity in

mouse and human PDAC (Fig. 2c and Extended Data Fig. 3l). Accordingly, protein levels of IL-1β were low in circulating monocytes from control and tumour-bearing mice but increased substantially upon recruitment to tumours (Fig. 2d). We next performed lineage tracing with *Ms4a3*^{cre}-*Rosa*^{TdT} mice, in which granulocyte-monocyte precursors (GMP) and their progeny are irreversibly marked by tdTomato[21]. The vast majority of IL-1β$^+$ TAMs were tdTomato$^+$ (Fig. 2e), indicating that these cells originate from circulating monocytes that infiltrate the tumour and become exposed to local factors in the TME.

PGE_2 and TNF elicit IL-1β$^+$ TAMs

We observed an enrichment of IL-1 and TNF response GO terms among driver genes of the monocyte-to-IL-1β$^+$ TAM transition (Extended Data Fig. 4a and Supplementary Table 3). The transcriptome of IL-1β$^+$ TAMs was enriched in genes induced by IL-1β or TNF in mouse macrophages[22], and both molecules were detectable in human PDAC (Extended Data Fig. 4b,c and Supplementary Table 4). However, treatment of mouse bone marrow-derived macrophages (BMDMs) with IL-1β or TNF did not elicit IL-1β synthesis, highlighting a requirement for additional factors (Extended Data Fig. 4d). The eicosanoid PGE_2, a known regulator of the immune TME[23], can stimulate IL-1β production while suppressing interferon responses in macrophages[24–26]. We detected high levels of PGE_2 in biopsies of human and mouse PDAC or in culture supernatant of tumour cells, and PGE_2-induced genes[25] were over-represented in IL-1β$^+$ TAMs (Fig. 2f, Extended Data Fig. 4e,f and Supplementary Table 4). We thus tested whether PGE_2 contributed to elicit the IL-1β$^+$ TAM state. PGE_2 alone had limited effects, but its co-administration with TNF—and not with IL-1β—triggered potent IL-1β synthesis in BMDMs and monocytes (Fig. 2g and Extended Data Fig. 4g,h). RNA-seq analyses in BMDMs identified dozens of transcripts synergistically induced by PGE_2 plus TNF, which were over-represented in IL-1β$^+$ TAMs and among the driver genes of monocyte-to-IL-1β$^+$ TAM transition; these genes encoded for factors that elicit tumour-promoting inflammation (*Il1b* and *Il6*) while suppressing cytotoxic immunity (*Il10*), or that stimulate prostaglandin synthesis (*Ptges* and *Ptgs2*), myeloid cell recruitment (*Cxcl1*, *Cxcl2* and *Cxcl3*) and tissue repair (*Areg*, *Arg2*, *Wnt11* and *Il33*) (Fig. 2h–j and Supplementary Table 4). Multiplexed analyses of proteins in the supernatant confirmed elevated synthesis of IL-6 and IL-10 by co-stimulated macrophages, and revealed PGE_2-driven suppression of CCL5, CXCL10, CXCL11 and CXCL16—chemokines with key roles in recruitment of cytotoxic T and NK cells (Fig. 2k). These data identify PGE_2 and TNF as TME factors that are able to cooperatively elicit the IL-1β$^+$ TAM state in PDAC.

IL-1β$^+$ TAMs accumulate in hypoxic areas

Immunofluorescence analyses of orthotopic PDAC highlighted a preferential distribution of IL-1β$^+$ TAMs in fibroblast-rich stromal regions surrounding the tumour core; differential distribution of TAM subsets was detectable at early time points in mouse tumours as well as in human PDAC (Extended Data Fig. 5a–c). We next performed paired single-cell and spatial transcriptome analyses of mouse PDAC. Transcript-based deconvolution of cell subsets was concordant with protein expression (Extended Data Fig. 5d–g and Supplementary Table 5). Spatial principal components (sPC) analyses discriminated spots enriched in IL-1β$^+$, FOLR2$^+$ or SPP1$^+$ TAMs (Extended Data Fig. 5h–k). Projection of signatures of genes synergized by PGE_2 plus TNF showed broad overlap with spots enriched in IL-1β$^+$ TAMs (Extended Data Fig. 5l). IL-1β$^+$ TAM regions were enriched in GO terms associated with inflammation, hypoxia, angiogenesis and wound healing (Extended Data Fig. 5m,n and Supplementary Table 5), as validated by immunofluorescence analyses showing the proximity of IL-1β$^+$ TAMs to CD31$^+$VEGFR2$^+$ endothelial cells and hypoxic areas (Extended Data Fig. 5o–p). We conclude that IL-1β$^+$ TAMs undergo local specification in inflamed, angiogenic and hypoxic regions of PDAC associated with high PGE_2 and TNF synergistic activity.

PDAC-derived PGE_2 promotes tumour growth

To assess the role of PGE_2 in PDAC, we treated immune-competent mice with celecoxib, a selective inhibitor of the prostaglandin biosynthetic enzyme cyclo-oxygenase-2 (COX2), concomitant with tumour challenge. This treatment lowered PGE_2 levels in tumours and was associated with reduced accumulation of IL-1β$^+$ TAMs and monocytes, increased infiltration of cytotoxic GZMB$^+$CD8$^+$ T cells and delayed tumour growth (Extended Data Fig. 6a–d). Because cancer cells produce high levels of PGE_2 (Extended Data Fig. 4e), we generated COX2-knockout (KO) PDAC lines that were unable to produce PGE_2 but did not show defects in viability or proliferation in vitro (Extended Data Fig. 6e–h and Supplementary Table 6). COX2-KO PDAC cells or spheroids engrafted in immune-competent mice but their growth was controlled in a CD8$^+$ T cell- and NK cell-dependent manner, in keeping with an observed increase of lymphocyte activation in tumour-draining lymph nodes (Fig. 3a,b and Extended Data Fig. 6i,j). Although neutrophil frequencies were reduced, immune cell composition was largely comparable between control and COX2-KO tumours at early disease stages (Extended Data Fig. 6k). We next performed scRNA-seq to assess the effect of PGE_2 on the pancreatic TME and found marked gene expression changes in selected cell populations, such as macrophages, activated T cells and fibroblasts (Extended Data Fig. 6l,n and Supplementary Table 6). More specifically, IL-1β$^+$ TAMs isolated from COX2-KO tumours showed reduced expression of key identity genes and inflammatory response markers and acquired interferon response signatures (Fig. 3c and Extended Data Fig. 6o). COX2-KO tumours were, however, controlled in mice lacking a key subunit of the IFNα and IFNβ receptor (*Ifnar1*$^{-/-}$ mice) (Extended Data Fig. 6p). These data identify a key role of tumour-derived PGE_2 in driving the IL-1β$^+$ TAM state in vivo and show that targeting COX2 leads to TME reprogramming and disease control in an interferon-independent manner.

Pathogenic IL-1β signalling in PDAC cells

Antibody-mediated targeting of IL-1β in vivo led to delayed PDAC growth, concomitant with reduced IL-1β expression by monocytes and TAMs and increased activation of cytotoxic T cells in draining lymph nodes (Fig. 3d–f and Extended Data Fig. 7a–c). Re-analysis of patient scRNA-seq data highlighted tumour monocytes and *IL1B*$^+$ TAMs as the major sources of IL-1β in human PDAC (Extended Data Fig. 7d and Supplementary Table 1). To determine the cellular targets of IL-1β in the TME, we performed tumour challenge experiments in haemato-chimeric mice in which bone marrow cells from *Il1r1*$^{-/-}$ donors, which lack a key signalling subunit of the IL-1 receptor, or from wild-type control were transplanted into irradiated wild-type or *Il1r1*$^{-/-}$ recipients, respectively. No defect in tumour growth was observed in the two groups (Extended Data Fig. 7e), indicating that the cancer-promoting effects of IL-1β are not driven by signalling in haematopoietic or stromal cells. Instead, IL1R1-KO KPC cells showed a markedly reduced capacity to form tumours in immune-competent mice, concomitant with reduced infiltration of IL-1β$^+$ monocytes and increased activation of CD8$^+$ T cells (Fig. 3g, Extended Data Fig. 7f–i and Supplementary Table 7). Re-expression of IL1R1 in gene-targeted PDAC cells rescued tumour growth in vivo (Fig. 3h and Extended Data Fig. 7j). Finally, stimulation with IL-1β promoted organoid generation by control PDAC cells, and not by IL1R1-KO PDAC cells, and explants of IL1R1-KO tumours showed defective organoid-forming efficiency (Fig. 3i and Extended Data Fig. 7k). These data highlight a requirement for tumour cell-intrinsic IL-1β signalling for PDAC growth.

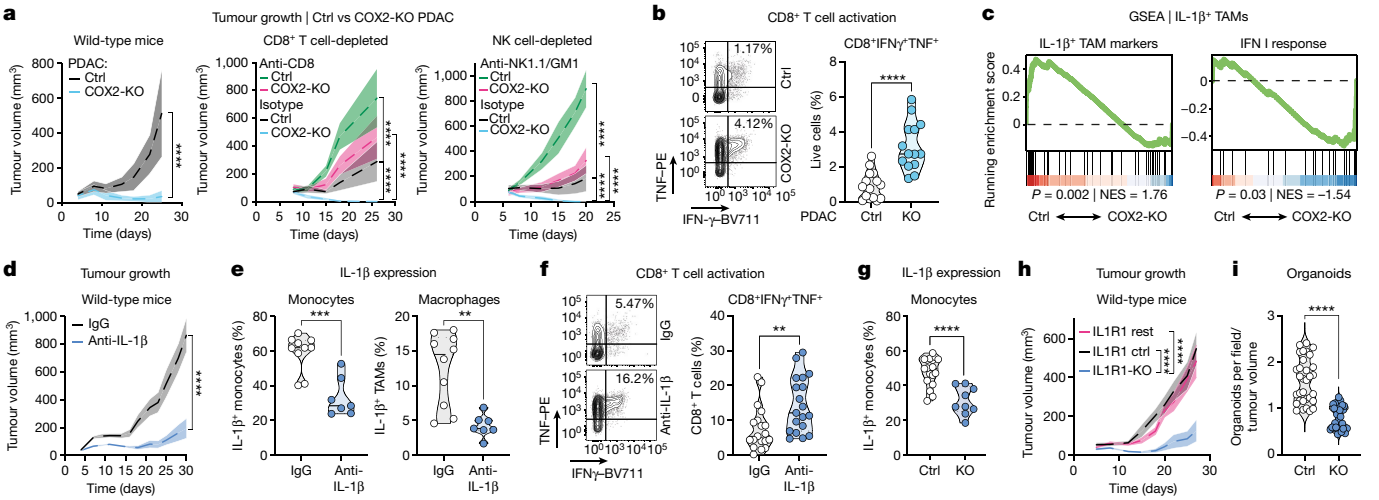

Fig. 3 | The PGE_2–IL-1β axis elicits IL-1β$^+$ TAMs and promotes PDAC growth. a, Growth curves (mean ± s.d.) of control and COX2-KO PDAC cells (subcutaneous KPC) in wild-type ($n = 5$ per group), $CD8^+$ T cell-depleted ($n = 5$ per group) or NK cell-depleted ($n = 9$ per group) mice. Two-way ANOVA. **b**, Contour plots (left) and frequency (right) of activated $CD8^+$ T cells in tumour-draining lymph nodes of mice inoculated with control ($n = 15$) or COX2-KO ($n = 14$) PDAC (subcutaneous KPC). Unpaired *t*-test. **c**, GSEA of IL-1β$^+$ TAM marker genes and type I interferon (IFN I) response genes on genes ranked by $\log_2$ fold change between IL-1β$^+$ TAMs from control versus COX2-KO PDAC (subcutaneous KPC, day 7). **d**, Growth curves (mean ± s.e.m.) of PDAC cells (subcutaneous KPC) in mice treated with anti-IL-1β or isotype control (IgG) ($n = 10$ per group). Two-way ANOVA. **e**, Frequency of tumour-infiltrating (subcutaneous KPC) IL-1β$^+$ monocytes or macrophages in mice treated with anti-IL-1β ($n = 7$) or IgG ($n = 10$). Unpaired Student's two-tailed *t*-test. **f**, Contour plots (left) and frequency (right) of activated $CD8^+$ T cells in tumour-draining lymph nodes (subcutaneous KPC, end stage) of mice treated with anti-IL-1β or IgG ($n = 19$ per group). Unpaired Student's two-tailed *t*-test. **g**, Frequency of tumour-infiltrating IL-1β$^+$ monocytes in mice inoculated with control ($n = 18$) or IL1R1-KO ($n = 9$) PDAC (subcutaneous KPC, end stage). Unpaired Student's two-tailed *t*-test. **h**, Growth curves (mean ± s.e.m.) of control, IL1R1-KO and IL1R1-reconstituted IL1R1-KO (IL1R1 rest) PDAC (subcutaneous KPC) in wild-type mice ($n = 10$ per group). Two-way ANOVA. **i**, Organoid-forming efficiency (organoids per field divided by tumour volume) of explanted control and IL1R1-KO PDAC (subcutaneous KPC, day 11). Tumours ($n = 4$ per group) were plated in 8 wells, 4 fields per well were counted. Unpaired Student's two-tailed *t*-test with Welch's correction.

Inflamed PDAC and TAMs engage in a loop

RNA-seq analyses of KPC cells treated with IL-1β revealed marked up-regulation of genes encoding myeloid growth factors (*Csf1* and *Csf2*), chemokines (*Ccl2*), cytokines (*Tnf*) and enzymes with immune regulatory functions (*Ptgs2* and *Nos2*) (Extended Data Fig. 8a and Supplementary Table 8). These results were confirmed by quantification of proteins in the supernatant, with CCL2 and CSF-1 being robustly induced by IL-1β in tumour cells (Extended Data Fig. 8a). To assess the functional relevance of these molecules, we performed tumour challenge experiments in *Ccr2*$^{-/-}$ mice, which lack the CCL2 receptor, and in wild-type mice treated with a neutralizing antibody against CSF-1. Both experiments led to impaired disease growth, highlighting a key role of monocyte-derived macrophages in PDAC (Extended Data Fig. 8b). We next focused on IL-1β-induced factors that drive macrophage conditioning. Among the most enriched GO terms in the transcriptome of cytokine-treated tumour cells were those associated with inflammation and prostaglandin secretion, in line with the finding that stimulation of KPC cells with IL-1β led to increased production of PGE_2 and TNF (Extended Data Fig. 8a,c and Supplementary Table 8). We next performed supernatant transfer experiments whereby tumour-conditioned medium (TCM) from KPC cells treated with IL-1β in the absence or presence of COX2 inhibitor (COX2i) were incubated with a blocking antibody against TNF and subsequently transferred onto BMDMs. Whereas TCM from untreated KPC cells did not trigger *Il1b* in macrophages, this gene was induced in response to TCM of IL-1β-stimulated tumour cells (Extended Data Fig. 8d). Inhibition of COX2 in KPC cells treated with IL-1β led to lower induction of *Il1b* in BMDMs exposed to the corresponding TCM, with this occurrence being even more evident upon neutralization of TNF (Extended Data Fig. 8d). These data highlight a self-sustaining loop between PDAC cells and macrophages, whereby IL-1β signalling in tumour cells triggers the release of factors that recruit monocytes to tumours and elicit the IL-1β$^+$ TAM state.

Early inflammatory reprogramming of PDAC

We integrated RNA-seq data from cytokine-treated PDAC cells and organoids to define a tumour-intrinsic IL-1β response signature (T1RS) (Extended Data Fig. 9a,b and Supplementary Table 9). This gene module was enriched in mouse[15] and human[27] PDAC transcriptomes, and it correlated with abundance of IL-1β$^+$ TAMs and poor survival in TCGA (Fig. 4a, Extended Data Fig. 9c and Supplementary Table 9). Longitudinal scRNA-seq analyses of orthotopic PDAC revealed up-regulation of T1RS in tumour cells at early time points, anticipating exponential disease growth and acquisition of proliferation, epithelial-to-mesenchymal transition (EMT) and extracellular matrix remodelling programmes (Extended Data Fig. 9d,e). To assess inflammatory reprogramming of tumour cells in vivo, we analysed gene expression data from mouse models of pancreatic tumorigenesis[28]. These studies revealed the highest T1RS expression in cells from mice with benign pancreatic intraepithelial neoplasia (PanIN), with levels of the signature remaining high in established PDAC and distal metastasis (Fig. 4b). Spatial transcriptome data from donor and patient samples[29] confirmed robust expression of the T1RS genes in human PanIN and PDAC lesions (Extended Data Fig. 9f). Inflammatory responses to tissue damage functionally cooperate with oncogenes to enhance pancreatic tumorigenesis via long-term reprogramming of epithelial cells[14,15]. We detected a subset of macrophages from patients with hereditary or idiopathic chronic pancreatitis[30] displaying a gene expression programme analogous to that of IL-1β$^+$ TAMs (Extended Data Fig. 9g,h). Analysis of RNA-seq data of normal or *Kras*-mutated cells from mice with caerulein-driven pancreatitis revealed marked T1RS

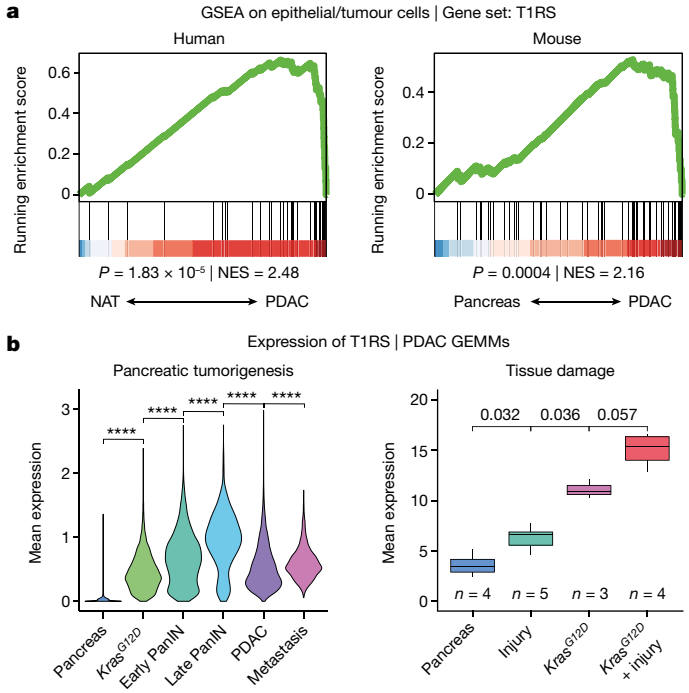

Fig. 4 | Inflammatory reprogramming occurs early during pancreatic tumorigenesis. a, GSEA of T1RS genes on genes ranked by log_2FC between human PDAC and normal adjacent tissue (NAT) or between mouse PDAC and control pancreas. NES, normalized enrichment score. **b**, Expression of T1RS genes in pancreatic cells from the indicated mouse models of tumorigenesis (left) or tissue damage and oncogene activation (right). Boxes extend from the bottom quartile to top quartile values, with a line at the median. Whiskers extend from the box to show the range of the data no further than 1.5 times the inter-quartile range from the hinges. Two-sided Mann–Whitney test. Sample size (right) is indicated.

expression as a consequence of oncogene activation, with levels of the module further increased upon injury (Fig. 4b). Analogous findings were obtained in cells from mice treated with the alarmin IL-33, which mediates tissue damage responses in the pancreas[15] (Extended Data Fig. 9i). Furthermore, T1RS expression remained elevated in pancreatic spheroids generated from caerulein-treated mice months after resolution of the injury[14] (Extended Data Fig. 9i). Thus, inflammatory reprogramming is an early event in pancreatic tumorigenesis leading to persistent transcriptional changes associated with disease progression and poor patient outcome.

IL-1β$^+$ TAMs colocalize with T1RS$^+$ PDAC

We next explored whether local interactions with IL-1β$^+$ TAMs underlie transcriptional heterogeneity and inflammatory reprogramming of tumour cells. Analysis of scRNA-seq data from patients with PDAC uncovered a subset of cancer cells expressing high levels of the T1RS (Fig. 5a, Extended Data Fig. 10a and Supplementary Table 10). Pseudotime analyses[31] identified T1RS$^+$ PDAC cells as endpoints of a transcriptional trajectory driven by increasing expression of the T1RS itself and of known IL-1β target genes, such as *NFKBIA*, *IL1RN* and *CXCL1* (Fig. 5a–c and Supplementary Table 10). The predicted development of T1RS$^+$ PDAC cells was also associated with increased expression of tumour markers (*CEACAM6*, *CEACAM7* and *KRT19*) and enrichment of GO terms associated to pancreatic tumorigenesis such as KRAS signalling, hypoxia, EMT, p53 pathway and TGFβ signalling, among others (Fig. 5c,d and Supplementary Table 10). These data highlight an intrinsic correlation between inflammatory reprogramming and acquisition of pathogenic programmes by tumour cells. We next set out to identify local interactions between macrophages and tumour cells using single-cell spatial gene expression in human PDAC. These analyses identified IL-1β$^+$ TAMs, as well as subsets of macrophages, immune, epithelial and stromal cells. We also detected putative T1RS$^+$ PDAC cells characterized by expression of KRT19 and CXCL1 and weak positivity for *IL1B* (Fig. 5e, Extended Data Fig. 10b and Supplementary Table 10). Overall, there was a clear spatial co-expression of *CXCL1* with *KRT19* and genes marking macrophages (*CD68*), as well as IL-1β (*IL1B*, *IL1A* and *THBS1*) and PGE_2 (*PTGS2* and *PTGER1*) programmes; correlation values were higher for marker genes of IL-1β$^+$ TAMs than for other macrophage subsets (Extended Data Fig. 10c and Supplementary Table 10). Indeed, T1RS$^+$ PDAC cells and IL-1β$^+$ TAMs were significantly and selectively enriched in each other's spatial neighbourhoods (Fig. 5f,g and Extended Data Fig. 10d,e). Ligand–receptor interaction analysis[32] between tumour cells and IL-1β$^+$ TAMs identified the IL-1–IL1R1 axis as the top-ranking driver of T1RS$^+$ PDAC cell gene expression (Fig. 5h and Extended Data Fig. 10f–h). These data highlight a spatially confined crosstalk between IL-1β$^+$ TAMs and T1RS$^+$ PDAC cells sustained by the PGE_2–IL-1β axis.

Discussion

Tissue-resident macrophages contribute to PDAC development and progression[11,12]. Here we report a pathogenic role of IL-1β$^+$ TAMs—a subset of monocyte-derived macrophages endowed with inflammatory, but not cytotoxic, programmes—in pancreatic cancer. IL-1β$^+$ TAMs engage in a spatially confined interaction with a subset of PDAC cells expressing an IL-1β response signature (T1RS) associated with poor patient survival. Our data indicate that tumour-infiltrating monocytes differentiate into IL-1β$^+$ TAMs upon exposure to PGE_2 and TNF and drive inflammatory reprogramming of neighbouring PDAC cells, promoting synthesis of PGE_2, TNF and other factors that further reinforce the IL-1β$^+$ TAM state. Local elicitation of a positive feedback loop between IL-1β$^+$ TAMs and T1RS$^+$ PDAC cells maintains a functional TME niche despite the labile biological activities of inflammatory mediators[33,34]. In this context, that T1RS$^+$ PDAC cells express genes of the IL-1β$^+$ TAM programme—*CXCL1* and, at low levels, *IL1B* itself—highlights spatially coordinated gene expression programmes across cell types in the TME, in line with a recent report[9]. Our data establish the PGE_2–IL-1β axis as a driver of the spatial and transcriptional heterogeneity of immune and tumour cells in PDAC.

The biological effects of PGE_2—suppression of cytotoxic immunity and enhancement of tumour-promoting inflammation[35]—reflect divergent control of gene modules in macrophages. PGE_2 limits interferon responses by targeting MEF2A and promoting IL-10 release[25], while boosting expression of inflammatory factors with roles in tissue repair, such as IL-1β. The molecular mechanisms underlying PGE_2-mediated synergisms remain to be elucidated. We found that IL-1β$^+$ TAMs accumulate in hypoxic areas of the tumour where inflammation, tissue repair and immune suppression co-exist[36]. In this context, PGE_2 was found to stabilize HIF-1α[37], a transcription factor that drives IL-1β synthesis in macrophages[38]. Future studies should examine whether and how hypoxia or other factors, such as physical tension or local interaction with stromal cells such as fibroblasts[39], contribute to the establishment or maintenance of IL-1β$^+$ TAM niches.

Inflammatory signalling in epithelial cells sustains tissue repair but can enhance tumorigenesis upon oncogene activation[14,15]. Reciprocally, driver mutations that accumulate in healthy tissues may never give rise to tumours in the absence of sustained injury[13]. Macrophages from patients with pancreatitis acquire a gene expression programme analogous to that of IL-1β$^+$ TAMs, possibly sustained by PGE_2 released from damaged cells[40]. Furthermore, *Kras* mutations are sufficient to trigger PGE_2 synthesis[23] and T1RS expression in epithelial cells, at levels that are increased upon tissue injury. Elicitation of a self-feeding loop via the PGE_2–IL-1β axis would thus integrate and stabilize the consequences of tissue injury and activated oncogenes.

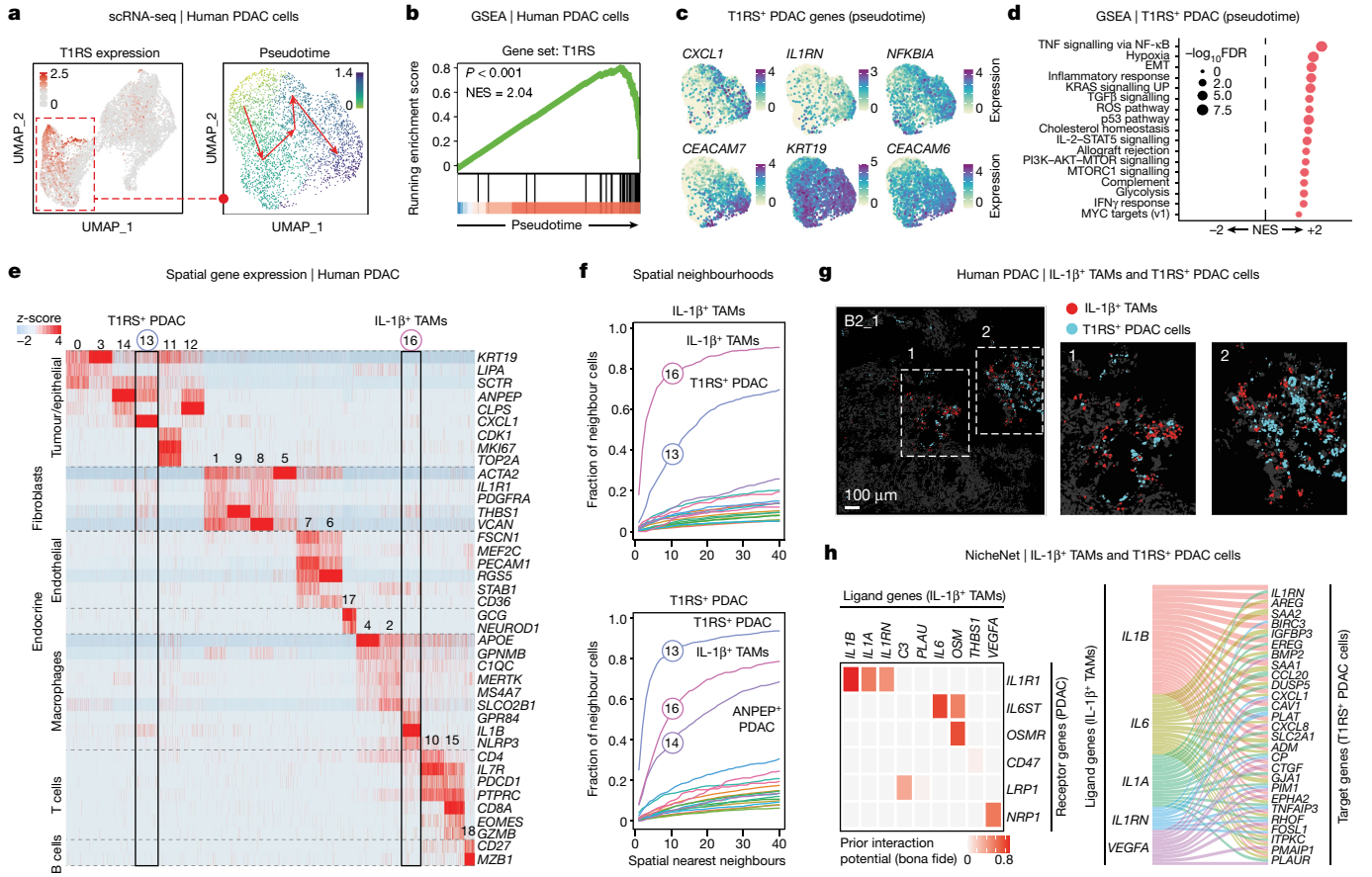

Fig. 5 | IL-1β$^+$ TAMs spatially colocalize with T1RS$^+$ PDAC cells in patients with PDAC. a, UMAP of scRNA-seq data of PDAC cells from chemotherapy-naive patients showing mean expression of T1RS genes (left) and pseudotime analyses (right). **b**, GSEA of T1RS genes on pseudotime-ordered genes of the computed developmental trajectory of T1RS$^+$ PDAC cells. **c**, Expression of selected pseudotime-correlated T1RS genes and/or IL-1β targets in PDAC cells. **d**, GSEA of MSigDB hallmark genes on pseudotime-ordered genes of the computed developmental trajectory of T1RS$^+$ PDAC cells. ROS, reactive oxygen species. **e**, Heat map of scaled expression (in situ RNA hybridization) of marker genes for clusters identified by spatial transcript analyses (Methods). Numbers refer to cluster identity. T1RS$^+$ PDAC cells (cluster 13) and IL-1β$^+$ TAMs (cluster 16) are highlighted. **f**, Fraction of cells belonging to each cluster identified by spatial transcript analyses (Methods) found in the spatial neighbourhood of IL-1β$^+$ TAMs (top) or T1RS$^+$ PDAC cells (bottom). Numbers and colours refer to cluster identity. **g**, Selected regions of interest (ROIs) (LPDAC30 B2_1) showing co-localization of IL-1β$^+$ TAMs and T1RS$^+$ PDAC cells in spatial gene expression analyses. The numbered regions of interest (left) are magnified (right). **h**, Left, heat map of interaction potential (NicheNet) between top-ranking ligands (Methods) expressed by IL-1β$^+$ TAMs and cognate receptors on PDAC cells. Right, alluvial plot showing the top five ligands expressed by IL-1β$^+$ TAMs ranked by overall regulatory potential, and their connection with predicted target genes expressed by T1RS$^+$ PDAC cells.

The pathogenic effects of inflammation in mutated cells underlie the resurgence of stem cell programmes, lineage infidelity or increased cell fitness[13]. We observed that inflammatory reprogramming of PDAC was required for disease growth and organoid formation, and it was associated with the acquisition of pathologic programmes such as EMT, in keeping with recent reports in kidney cancer[41,42]. We posit that activation of the PGE_2–IL-1β axis represents a physiological response to injury whose co-optation by cancer promotes disease progression.

The work described in this Article and other studies[43–48] establish the PGE_2–IL-1β axis as a driver of tumour-promoting inflammation. Although macrophages are a key source of IL-1β in pancreatic cancer, subsets of tumour cells[43]—namely, T1RS$^+$ PDAC cells—or other populations in the niche may also contribute to cytokine synthesis, highlighting broad targeting of the pathway as a strategy to overcome compensatory effects. Given the self-amplifying nature of the loop, inhibition of the PGE_2–IL-1β axis should have maximal therapeutic efficacy during early stages or in preventive settings, while boosting immunotherapy in advanced disease[46–48].

Targeting IL-1β might yield variable therapeutic outcomes according to the cell type- and tissue-specific activities of this cytokine[46]. Indeed, IL-1β supports cytotoxic T cell activation in tumour-draining lymph nodes[49] and the CANTOS trial in patients treated with the IL-1β blocking antibody canakinumab showed a reduced incidence of lung, but not colorectal, cancer[50]. Having resolved the molecular, spatial and functional regulation of IL-1β$^+$ TAMs, our study should inform the design and interpretation of clinical trials targeting IL-1β and/or COX2 as preventive or combination immunotherapies.

Online content

Any methods, additional references, Nature Portfolio reporting summaries, source data, extended data, supplementary information, acknowledgements, peer review information; details of author contributions and competing interests; and statements of data and code availability are available at https://doi.org/10.1038/s41586-023-06685-2.

1. Halbrook, C. J., Lyssiotis, C. A., Pasca di Magliano, M. & Maitra, A. Pancreatic cancer: advances and challenges. *Cell* **186**, 1729–1754 (2023).
2. Mantovani, A., Allavena, P., Marchesi, F. & Garlanda, C. Macrophages as tools and targets in cancer therapy. *Nat. Rev. Drug. Discov.* **21**, 799–820 (2022).

3. Glass, C. K. & Natoli, G. Molecular control of activation and priming in macrophages. *Nat. Immunol.* **17**, 26–33 (2016).
4. Amit, I., Winter, D. R. & Jung, S. The role of the local environment and epigenetics in shaping macrophage identity and their effect on tissue homeostasis. *Nat. Immunol.* **17**, 18–25 (2016).
5. Salmon, H., Remark, R., Gnjatic, S. & Merad, M. Host tissue determinants of tumour immunity. *Nat. Rev. Cancer* **19**, 215–227 (2019).
6. Medzhitov, R. The spectrum of inflammatory responses. *Science* **374**, 1070–1075 (2021).
7. Mulder, K. et al. Cross-tissue single-cell landscape of human monocytes and macrophages in health and disease. *Immunity* **54**, 1883–1900.e1885 (2021).
8. Cheng, S. et al. A pan-cancer single-cell transcriptional atlas of tumor infiltrating myeloid cells. *Cell* **184**, 792–809.e723 (2021).
9. Bill, R. et al. CXCL9:SPP1 macrophage polarity identifies a network of cellular programs that control human cancers. *Science* **381**, 515–524 (2023).
10. Liudahl, S. M. et al. Leukocyte heterogeneity in pancreatic ductal adenocarcinoma: phenotypic and spatial features associated with clinical outcome. *Cancer Discov.* **11**, 2014–2031 (2021).
11. Baer, J. M. et al. Fibrosis induced by resident macrophages has divergent roles in pancreas inflammatory injury and PDAC. *Nat. Immunol.* **24**, 1443–1457 (2023).
12. Zhu, Y. et al. Tissue-resident macrophages in pancreatic ductal adenocarcinoma originate from embryonic hematopoiesis and promote tumor progression. *Immunity* **47**, 597 (2017).
13. Weeden, C. E., Hill, W., Lim, E. L., Gronroos, E. & Swanton, C. Impact of risk factors on early cancer evolution. *Cell* **186**, 1541–1563 (2023).
14. Del Poggetto, E. et al. Epithelial memory of inflammation limits tissue damage while promoting pancreatic tumorigenesis. *Science* **373**, eabj0486 (2021).
15. Alonso-Curbelo, D. et al. A gene-environment-induced epigenetic program initiates tumorigenesis. *Nature* **590**, 642–648 (2021).
16. Nalio Ramos, R. et al. Tissue-resident FOLR2^{+} macrophages associate with CD8^{+} T cell infiltration in human breast cancer. *Cell* **185**, 1189–1207.e1125 (2022).
17. Montaldo, E. et al. Cellular and transcriptional dynamics of human neutrophils at steady state and upon stress. *Nat. Immunol.* **23**, 1470–1483 (2022).
18. Hingorani, S. R. et al. *Trp53*^{R172H} and *Kras*^{G12D} cooperate to promote chromosomal instability and widely metastatic pancreatic ductal adenocarcinoma in mice. *Cancer Cell* **7**, 469–483 (2005).
19. Schiebinger, G. et al. Optimal-transport analysis of single-cell gene expression identifies developmental trajectories in reprogramming. *Cell* **176**, 928–943.e922 (2019).
20. Lange, M. et al. CellRank for directed single-cell fate mapping. *Nat. Methods* **19**, 159–170 (2022).
21. Liu, Z. et al. Fate mapping via *Ms4a3*-expression history traces monocyte-derived cells. *Cell* **178**, 1509–1525.e1519 (2019).
22. Ostuni, R. et al. Latent enhancers activated by stimulation in differentiated cells. *Cell* **152**, 157–171 (2013).
23. Zelenay, S. et al. Cyclooxygenase-dependent tumor growth through evasion of immunity. *Cell* **162**, 1257–1270 (2015).
24. Perkins, D. J. et al. Autocrine-paracrine prostaglandin E2 signaling restricts TLR4 internalization and TRIF signaling. *Nat. Immunol.* **19**, 1309–1318 (2018).
25. Cilenti, F. et al. A PGE2–MEF2A axis enables context-dependent control of inflammatory gene expression. *Immunity* **54**, 1665–1682 (2021).
26. Zaslona, Z. et al. The induction of pro-IL-1β by lipopolysaccharide requires endogenous prostaglandin E2 production. *J. Immunol.* **198**, 3558–3564 (2017).
27. Peng, J. et al. Single-cell RNA-seq highlights intra-tumoral heterogeneity and malignant progression in pancreatic ductal adenocarcinoma. *Cell Res.* **29**, 725–738 (2019).
28. Burdziak, C. et al. Epigenetic plasticity cooperates with cell-cell interactions to direct pancreatic tumorigenesis. *Science* **380**, eadd5327 (2023).
29. Carpenter, E. S. et al. Analysis of donor pancreata defines the transcriptomic signature and microenvironment of early neoplastic lesions. *Cancer Discov.* **13**, 1324–1345 (2023).
30. Lee, B. et al. Single-cell sequencing unveils distinct immune microenvironments with CCR6–CCL20 crosstalk in human chronic pancreatitis. *Gut* **71**, 1831–1842 (2022).
31. Street, K. et al. Slingshot: cell lineage and pseudotime inference for single-cell transcriptomics. *BMC Genomics* **19**, 477 (2018).
32. Browaeys, R., Saelens, W. & Saeys, Y. NicheNet: modeling intercellular communication by linking ligands to target genes. *Nat. Methods* **17**, 159–162 (2020).
33. Gong, Z. et al. Lung fibroblasts facilitate pre-metastatic niche formation by remodeling the local immune microenvironment. *Immunity* **55**, 1483–1500.e1489 (2022).
34. Roulis, M. et al. Paracrine orchestration of intestinal tumorigenesis by a mesenchymal niche. *Nature* **580**, 524–529 (2020).
35. Bonavita, E. et al. Antagonistic inflammatory phenotypes dictate tumor fate and response to immune checkpoint blockade. *Immunity* **53**, 1215–1229.e8 (2020).
36. Sattiraju, A. et al. Hypoxic niches attract and sequester tumor-associated macrophages and cytotoxic T cells and reprogram them for immunosuppression. *Immunity* **56**, 1825–1843 (2023).
37. Liu, X. H. et al. Prostaglandin E2 induces hypoxia-inducible factor-1alpha stabilization and nuclear localization in a human prostate cancer cell line. *J. Biol. Chem.* **277**, 50081–50086 (2002).
38. Tannahill, G. M. et al. Succinate is an inflammatory signal that induces IL-1β through HIF-1α. *Nature* **496**, 238–242 (2013).
39. Adler, M. et al. Principles of cell circuits for tissue repair and fibrosis. *iScience* **23**, 100841 (2020).
40. Hangai, S. et al. PGE_2 induced in and released by dying cells functions as an inhibitory DAMP. *Proc. Natl Acad. Sci. USA* **113**, 3844–3849 (2016).
41. Li, R. et al. Mapping single-cell transcriptomes in the intra-tumoral and associated territories of kidney cancer. *Cancer Cell* **40**, 1583–1599.e1510 (2022).
42. Chittezhath, M. et al. Molecular profiling reveals a tumor-promoting phenotype of monocytes and macrophages in human cancer progression. *Immunity* **41**, 815–829 (2014).
43. Das, S., Shapiro, B., Vucic, E. A., Vogt, S. & Bar-Sagi, D. Tumor cell-derived IL1β promotes desmoplasia and immune suppression in pancreatic cancer. *Cancer Res.* **80**, 1088–1101 (2020).
44. Hill, W. et al. Lung adenocarcinoma promotion by air pollutants. *Nature* **616**, 159–167 (2023).
45. Dmitrieva-Posocco, O. et al. Cell-type-specific responses to interleukin-1 control microbial invasion and tumor-elicited inflammation in colorectal cancer. *Immunity* **50**, 166–180.e167 (2019).
46. Garlanda, C. & Mantovani, A. Interleukin-1 in tumor progression, therapy, and prevention. *Cancer Cell* **39**, 1023–1027 (2021).
47. Bell, C. R. et al. Chemotherapy-induced COX-2 upregulation by cancer cells defines their inflammatory properties and limits the efficacy of chemoimmunotherapy combinations. *Nat. Commun.* **13**, 2063 (2022).
48. Nikolos, F. et al. Cell death-induced immunogenicity enhances chemoimmunotherapeutic response by converting immune-excluded into T-cell inflamed bladder tumors. *Nat. Commun.* **13**, 1487 (2022).
49. Zhivaki, D. et al. Inflammasomes within hyperactive murine dendritic cells stimulate long-lived t cell-mediated anti-tumor immunity. *Cell Rep.* **33**, 108381 (2020).
50. Ridker, P. M. et al. Effect of interleukin-1β inhibition with canakinumab on incident lung cancer in patients with atherosclerosis: exploratory results from a randomised, double-blind, placebo-controlled trial. *Lancet* **390**, 1833–1842 (2017).

Methods

Patient samples

Human samples from resected primary PDAC as well as peripheral blood samples were obtained from the Pancreatic Surgery Unit at the Pancreas Translational and Clinical Center of San Raffaele Hospital (Milan, Italy). The study was compliant with the Declaration of Helsinki and the General Data Protection Regulation and was approved by San Raffaele Hospital ethic committee (protocols: NEU-IPMN and LiMeT). Tissue specimens were confirmed to be tumour or adjacent normal tissue based on pathologist assessment. Informed consent was obtained by all participants, which received no compensation. Age and sex, as well as anonymized clinical information of participants are reported in Supplementary Table 1.

Mouse PDAC

KC (DT6606) and KPC (K8484) cell lines were previously established[18,51,52] from tumours arising in genetically engineered mouse models (GEMMs) carrying the G12D oncogenic mutation in the *Kras* gene (*Kras*$^{LSL\text{-}G12D/+}$;*Pdx1*$^{cre/WT}$ for KC) and the missense point R720H mutation in the *Tpr53* gene (*Kras*$^{LSL\text{-}G12D/+}$;*Tpr53*$^{LSL\text{-}R270H/+}$;*Pdx1*$^{cre/WT}$ for KPC). Panc02 cell line is derived from a methylcholanthrene-induced PDAC[53]. KC, KPC and Panc02 cell lines were kindly provided by L. Piemonti and not authenticated. All cell lines were cultured under standard conditions and periodically tested for mycoplasma.

CRISPR–Cas9-mediated gene targeting

Single guide RNAs (sgRNAs) were designed using CHOPCHOP[54] and synthetized by in vitro transcription using GeneArt Precision gRNA Synthesis Kit (Invitrogen), following manufacturer's instructions. Ribonucleoprotein complexes (Cas9–sgRNA) were generated by incubating 12 µg of sgRNA with 5 µg of Cas9 for 15 min at room temperature. KPC, KC or Panc02 cells (2.5×10^4) were resuspended in SF solution of SF Cell Line 4D Nucleofector X Kit S, mixed with ribonucleoprotein complexes and electroporated using EP-100 program of the 4D Nucleofector System (Lonza). Three days after nucleofection, single clones were sorted by fluorescence-activated cell sorting (FACS) in 96-well plates. Single-cell clones were screened to evaluate non-homologous end joining (NHEJ) efficiency on the targeted site with T7 endonuclease assay. In brief, genomic DNA was extracted using QuickExtract DNA Extraction Solution and targeted regions were amplified by PCR. PCR products were purified with Ampure XP beads and quantified by Nanodrop 8000. Purified PCR products were mixed 1:1 with corresponding products from wild-type cells. Annealed PCR products (400 ng) were digested with T7 Endonuclease for 30 min at 37 °C and subjected to capillary electrophoresis using D1000 TapeStation kit (Agilent 4200 TapeStation). NHEJ efficiency was defined by calculating the percentage of PCR product cleavage. Gene-edited clones were validated by Sanger sequencing using PCR products encompassing the target sequence. Polyclonal knockout pools were generated mixing an equal amount of at least five validated clones. The absence of the targeted protein was further validated by western blot analyses. A complete list of sgRNAs and primer pairs used for the NHEJ assay is reported in the Supplementary Tables 6 and 7.

In vivo animal studies

All experiments and procedures were performed according to protocols approved by the Institutional Animal Care and Use Committee (IACUC) at San Raffaele Scientific Institute animal facilities and authorized by the Italian Ministry of Health in accordance with the Italian Laws (D.L.vo 116/92), which enforce the EU 86/609 Directive (approval numbers 449/2018-PR, 962/2020-PR and 908/2021-PR). C57BL/6 N mice were purchased from Charles River Italy; IFNAR-KO and CCR2-KO mice were obtained from Matteo Iannacone (IRCCS San Raffaele Scientific Institute, Milan, Italy); IL1R1-KO mice were provided by C. Garlanda. All mice were maintained under pathogen-free conditions at the animal facility of San Raffaele Scientific Institute with a 12 h:12 h dark:light cycle and standardized temperature (22 ± 2 °C) and humidity (55 ± 5%). *Ms4a3*^{cre}-*Rosa*^{TdT} mice were maintained under pathogen-free conditions at Institute Gustave Roussy. Pancreatic tissue samples from GEMMs of PDAC (*Kras*$^{LSL\text{-}G12D/+}$;*Tpr53*$^{LSL\text{-}R270H/+}$;*Pdx1*$^{cre/WT}$) were provided by F. Novelli. No statistical method was used to predetermine sample size. Sample sizes were estimated based on preliminary experiments. Mice were allocated randomly to the experimental groups. Blinding was used to measure tumour growth curves, both when using digital calliper and ultrasound analyses.

Orthotopic tumours

To establish orthotopic models, 6- to 9-week-old female (KPC injection) and male (KC injection) mice were anaesthetized with isoflurane and subjected to surgical procedure. After left abdominal incision, pancreatic tails were exposed and injected with 5×10^5 tumour cells resuspended in cold PBS mixed at 1:4 dilution with Matrigel (Corning) in a final volume of 50 µl. Mice were monitored with ultrasound imaging to measure tumour progression. Experiments were terminated when tumours reached a size of 1,000 mm^3, as per the IACUC limit.

Heterotopic tumours

To establish heterotopic tumours, a total of 2×10^6 cancer cells were resuspended in 200uL of endotoxin-free PBS and injected subcutaneously in the right flank of mice. Female mice were used for KPC injection and male mice were used for KC and PANC02 injection. Tumour growth was monitored using a digital caliper. Tumour volume was estimated assuming ellipsoidal shape as $(a \times b)^2 \times \pi/6$, where a is the major diameter and b is the minor diameter. Experiments were terminated when tumours reached a size of 1,000 mm^3, as per IACUC limit.

In vivo treatments

The COX2 inhibitor celecoxib was prepared at a concentration of 2 mg ml^{-1} in a solution of 10% DMSO, 50% poly(ethylene glycol) (Average Mn 400 (PEG400) (Sigma)), and 40% Cell Culture Grade Water (Corning) and 200 µl (400 µg per mouse) were administered daily through oral gavage[55]. For IL-1β neutralization, mice were intraperitoneally injected with 50 µg per mouse of IL-1β monoclonal antibody (Clone B122, InVivoMAb, BioXCell) or isotype control (Polyclonal Armenian Hamster IgG, InVivoMAb, BioXCell) on the day of tumour inoculation and at 1 day post inoculation (dpi). Starting from day 4 dpi, mice were injected three times a week for the entire duration of the experiment. CD8$^+$ T cells depletion was achieved by injecting mice intraperitoneally with 300 µg per mouse of anti-mouse CD8α (Clone 2.43, BioXCell) or isotype control (Clone LTF-2, BioXCell) 2 days before tumour injection. Starting from day 4 dpi, mice were treated twice a week with 200 µg per mouse of antibody or isotype control for the entire duration of the experiment. Depletion of CD8$^+$ T cells was confirmed by FACS analysis on blood and tumour samples. NK cells depletion was achieved by injecting the mice with a combination of 200 µg per mouse of anti-mouse NK1.1 (clone PK136, BioXCell) and 50 µl per mouse of anti-ASIALO GM-1 (clone Poly21460, BioLegend) or isotype control (clone C1.18.4, BioXCell) 1 day before and 1 day after tumour inoculation. Starting from day 4 dpi, mice were injected twice a week for the entire duration of the experiment. Depletion of NK cells was confirmed by FACS analysis on blood and tumour samples. For CSF-1 neutralization, mice were intraperitoneally injected with 1 mg/mouse of mouse CSF-1 monoclonal antibody (Clone 5A1, BioXCell) or isotype control (clone HRPN, BioXCell) 3 days before tumour inoculation. Starting from day 1 dpi, mice were injected with 500 µg per mouse every 5 days. Depletion of monocytes was assessed by FACS analysis on blood and tumour samples.

Bone marrow chimeras

Recipient mice were lethally irradiated with two doses of radiations for a total of 935 cGy. The following day, irradiated mice were transplanted with 5×10^6 total bone marrow cells by intravenous injections. Bone marrow chimerism was checked by measuring the percentage of CD45.1/CD45.2 cells in blood samples by flow cytometry 4- and 10-weeks post transplantation. Bone marrow chimeras were inoculated with KPC cells 12-weeks post transplantation.

Tissue processing

Human and mouse peripheral blood samples were incubated with red blood cell (RBC) lysis buffer (Biolegend) for 10 min on ice and washed with PBS. Cells were centrifuged for 5 min at 450*g* and resuspended in the appropriate buffer for downstream application. Freshly resected human PDAC samples were minced in small pieces and digested with the Tumor Dissociation Kit, Human (Miltenyi Biotec). Similarly, mouse healthy pancreas and tumours were manually minced in small pieces and dissociated with the Tumor Dissociation Kit, Mouse (Miltenyi Biotec) following the manufacturer's instructions. The obtained single cells suspensions were filtered on 70-µm cell strainers, incubated with RBC lysis buffer for 10 min on ice and resuspended in the appropriate buffer for cell counting and downstream application. In selected experiments, mouse tumour-draining lymph nodes were smashed, filtered through a 70-µm cell strainer, and resuspended in the appropriate buffer for downstream application. For the collection of plasma samples, an aliquot of 300 µl of blood collected into EDTA tubes was centrifuged for 5 min at 10,000*g*. Plasma was transferred into a clean tube and re-centrifuged 5 min at 10,000*g*. Plasma samples were frozen and stored at −80 °C until use. Supernatants of human PDAC and normal adjacent tissues were generated by culturing weighted tissues (1 to 30 mg) in 1 ml of complete media in a 48-well plate. After 48 h, supernatants were collected, centrifuged for 5 min at 450*g* to remove cellular debris and stored at −80 °C until use. For mass spectrometry experiments, tissue samples were chopped, weighted and immediately snap frozen at −80 °C.

Culture of mouse monocytes and macrophages

Bone marrow cells were collected by crushing the hips, femurs, and tibias of female mice in 50 ml of sterile PBS, filtered through a 70-µm cell strainer, and centrifuged for 5 min at 450*g*. Red blood cells were lysed using 0.2% NaCl solution, followed by 1.6% NaCl solution. Bone marrow cells were filtered through a 70-µm cell strainers and centrifuged for 5 min at 450*g*. For BMDM differentiation, cells were counted and seeded in IMDM supplemented with 20% FBS, 20% L929-conditioned media containing M-CSF, antibiotics (penicillin G 100 U ml^{-1} and streptomycin sulfate 100 U ml^{-1}), 2 mM L-glutamine and 5 µM 2-mercaptoethanol. Four days after culture, fresh medium was added to the cells. At day 7 after plating, cells were stimulated as described below. Monocytes were isolated from total bone marrow cells using the mouse Monocyte Isolation Kit (BM, Miltenyi Biotec), following manufacturer's instructions. At the end of the isolation procedure, cells were >90–95% CD11b$^+$Ly6G$^-$Ly6C$^+$ as assessed by flow cytometry. Monocytes were counted and seeded in U-bottom 96-well plates at a density of 1×10^5 cells per well in RPMI supplemented with 10% FBS, antibiotics (penicillin G 100 U ml^{-1} and streptomycin sulfate 100 U ml^{-1}) and 2 mM L-glutamine. One hour after plating, monocytes were stimulated as described below.

Ex vivo stimulation of mouse cells

Cells were stimulated with TNF (10 ng ml^{-1}), PGE_2 (1 µM) and/or IL-1β (10 ng ml^{-1}). For stimulation with TCM, KPC cells were stimulated or not for 24 h with either IL-1β (10 ng ml^{-1}), COX2 inhibitor SC-236 (Cayman Chemical) (10 µM), or both. At the end of the stimulation, TCM was collected, centrifuged for 5 min at 450*g* to remove cellular debris, filtered through 0.22-µm strainer and stored at −80 °C. Before BMDM stimulation, thawed TCM was incubated at 37 °C for 30 min with anti-TNF (25 µg ml^{-1}; Clone XT3.11, InVivoMAb, BioXCell) or isotype control rat IgG1 anti-horseradish peroxidase (25 µg ml^{-1}; Clone HRPN, InVivoMAb, BioXCell). To rule out any carryover effect of COX2 inhibitor, fresh SC-236 (10 µM) was added to the TCM before stimulating BMDMs.

Generation and culture of mouse PDAC spheroids

For the establishment of mouse pancreatic tumour spheroid culture, 1×10^4 wild-type and COX2-KO KPC cells were resuspended in 50 µl Matrigel, plated in 4-well culture plates (Nunc) and grew in Mouse Complete Medium (Advanced DMEM/F12) supplemented with 10 mM HEPES, antibiotics (penicillin G 100 U ml^{-1} and streptomycin sulfate 100 U ml^{-1}), 1% GlutaMax, B-27 supplement, 10 mM nicotinamide, 1.25 mM *N*–acetylcysteine, 10 ng ml^{-1} recombinant human R–spondin1, 100 ng ml^{-1} recombinant human FGF10, 100 ng ml^{-1} recombinant human Noggin, 500 nM A83–01, 50 ng ml^{-1} recombinant human EGF, 10 nM Gastrin1 and 10.5 µM Y–27632. Spheroid cultures were split at confluence by dissolving Matrigel in cold splitting medium (Advanced DMEM/F12 supplemented with 10 mM Hepes, 1% GlutaMAX and antibiotics (100 U ml^{-1} penicillin G and 100 U ml^{-1} streptomycin sulfate)). Spheroids were then mechanically disrupted with a 21G needle syringe, centrifuged for 5 min at 300*g*, and washed with splitting medium. After a second centrifugation, dissociated spheroids were resuspended in Matrigel and spotted as domes (50 µl per dome) in 4-well culture plates with Mouse Complete Medium. For orthotopic injections, wild-type and COX2-KO KPC-derived spheroids were collected after 6 passages in cold splitting medium and centrifuged at 300*g* for 5 min at 8 °C. Spheroids were then mechanically dissociated, centrifuged at 300*g* for 5 min, and resuspended in a solution of 25% Matrigel in PBS. Dissociated spheroids (1×10^6 cells in 50 µl) were injected orthotopically in immune-competent mice as described above.

Generation and culture of mouse PDAC organoids

Mouse PDAC organoids from IL1R1 wild-type or IL1R1-KO KPC cells were generated according to previously published protocol[56]. In brief, IL1R1 wild-type or IL1R1-KO KPC cells were subcutaneously injected into C57BL/6 N mice as described above. At 11 days dpi, tumours were explanted and manually minced into 1–2 mm^3 pieces in splitting medium, incubated for 1–2 h at 37 °C in pre-warmed digestion solution (splitting medium supplemented with 0.125 mg ml^{-1} collagenase type I, 0.125 mg ml^{-1} dispase II and 0.1 mg ml^{-1} DNase I), and further mechanically dissociated by vigorously pipetting. Dissociated samples were then filtered through a 70 µm cell strainer and washed with cold wash medium (DMEM high glucose supplemented with 1% FBS and antibiotics (100 U ml^{-1} penicillin G and 100 U ml^{-1} streptomycin sulfate)). Cells were pelleted at 300*g* for 5 min at 8 °C and washed twice with wash medium. Finally, tumour cells were resuspended in cold Matrigel, plated into 50 µl dome per well. After Matrigel solidification, 500 µl of warm mouse complete medium supplemented with 10.5 µM ROCK inhibitor were added to each well.

In vitro stimulation of mouse PDAC organoids. Four domes of organoids (passage 3) obtained from either IL1R1 wild-type ($n = 4$) or IL1R1-KO ($n = 4$) tumours were incubated in dispase solution (splitting medium supplemented with 2 mg ml^{-1} dispase II) for 20 min at 37 °C, to allow matrix dissociation. Matrix-free organoids were centrifuged at 300*g* for 5 min at 8 °C, and dissociated by incubation with TrypLE digestion enzyme at 37 °C for 10 min, followed by addition of Dispase Solution supplemented with 0.1 mg ml^{-1} DNase I for 10 min. Cells were counted and seeded at 5×10^3 single cells per well in 4 wells of 8-well glass bottom µ-Slides (Ibidi) in a final volume of 100 µl Matrigel per well. Cultures were maintained in mouse complete medium supplemented with 10.5 µM ROCK inhibitor and stimulated with 10 ng ml^{-1} IL-1β where indicated, replacing the medium and the stimulus every 72 h for a total of five days.

Analysis of organoid-forming efficiency. For freshly prepared organoids, the forming efficiency was assessed after 6 days of culture. Each tumour ($n = 4$ per group) was plated in 8 domes, and for each dome four different brightfield images were captured to allow the counting of live organoids. Then, the mean number of organoids per field, normalized for the volume of the tumour of origin, was calculated.

For organoids stimulated with IL-1β, samples were fixed for 20 min in 4% PFA at 37 °C and processed for immunofluorescence analysis. In brief, after fixation, organoid cultures were permeabilized with PBS + 0.5% Triton X-100 at 37 °C for 30 min and then incubated in blocking buffer (PBS + 5% BSA + 10% Donkey Serum (Jackson Immunoresearch) + 0.5% Triton X-100) at 37 °C for 30 min. Samples were then incubated with Alexa Fluor 488 Phalloidin (Invitrogen A12379, 1:200) in 1% BSA for 3 h at room temperature. Nuclei were counterstained with DAPI for 10 min at room temperature. Samples were imaged on an Olympus FluoVIEW 3000 RS confocal laser scanning system using UPLXAPO 4×/0.16 objective, by acquiring 3 × 3 grids and optical sections of 33 µm each (1,95 AU) were collected for each well to cover the entire Matrigel area.

Data processing. Image segmentation was performed using the machine learning tool of the Arivis Vision 4D software (ZeissAG) using annotated ROIs as training input. Identified image objects were filtered by sphericity (>0.6) and volume (>10^3 µm^3). The volume and the number of organoids for each well were calculated and exported for statistical analyses. The same parameters for organoid identification were applied to all the imaged samples.

In vitro stimulation of tumour cells and organoids with IL-1β for gene expression analysis

KC, KPC cell lines (2D) and KPC-derived organoids (3D) were cultured as described above and stimulated with IL-1β to the final concentration of 10 ng ml^{-1} for the indicated time points or left untreated. At the end of the stimulation, KPC organoids were dissolved in cold Cell Recovery Solution (Gibco) at 4 °C for 20 min in agitation, centrifuged at 400*g* for 5 min at 4 °C, and resuspended in lysis buffer (ReliaPrep RNA Cell Miniprep System, Promega). Bulk and scRNA-seq were performed as described below.

Lentiviral transduction of KPC cells

Il1r1 cDNA was synthetized and cloned in the pCCLsin.PPT.hPGK.GFP.wpre plasmid by GenScript DNA Synthesis service. Lentiviral vectors were produced, concentrated and titrated as previously described[57]. For KPC transduction, single IL1R1-KO clones (2×10^5 cells) were transduced with a multiplicity of infection of 10. Two weeks after transduction, IL1R1$^+$ cells were sorted (FACSAria instrument; BD Biosciences) and expanded in vitro for tumour inoculation. Polyclonal IL1R1-reconstituted pools were generated mixing an equal amount of five validated clones. The presence of the targeted protein was further validated by western blot analyses.

Flow cytometry

If not differently stated, single-cell suspensions were incubated with mouse FcγIII/II receptor (CD16/CD32) blocking antibody for 10 min on ice and pelleted by centrifugation. Cell viability was assessed by Aqua Live/Dead staining, applied for 30 min at 4 °C. Surface staining was then performed with fluorophore-conjugated primary antibodies for 30 min at 4 °C. For intracellular staining, samples were fixed with IC Fixation Buffer (Biolegend) and permeabilized with Intracellular Staining Perm Wash Buffer 10X (Biolegend) according to manufacturer's instructions. For detection of intracellular IFNγ and TNF, tumour-draining lymph nodes were processed as described above. Single-cell suspensions were incubated in a 96-well plate with Cell Activation Cocktail with Brefeldin A (Biolegend) for 3 h at 37 °C, and then stained as described above. To assess cell apoptosis and viability, KC and KPC cells (wild-type and COX2-KO) were washed with cold PBS and resuspended in annexin V binding buffer (PE Annexin V Apoptosis Detection kit, Biolegend). Cells were stained following manufacturer's instructions. For the quantification of the intracellular IL-1β in monocytes, total bone marrow cells were seeded in a 48-well plate at a density of 2×10^6 cells per well in IMDM supplemented with 10% FBS, antibiotics (penicillin G 100 U ml^{-1} and streptomycin sulfate 100 U ml^{-1}) and 2 mM L-glutamine and stimulated as indicated. After stimulation, samples were processed for flow cytometry analysis as reported. After exclusion of doublets and dead cells, monocytes were gated as CD11b$^+$Ly6G$^-$Ly6C$^+$. Absolute cell count was performed using Precision Count Beads (Biolegend), following manufacturer's instructions. All samples were acquired on BD FACSymphony and FACSCanto II using DIVA software v.8.0.2 (BD Biosciences). Data were analysed with FlowJo Software (v. 10.8.1). Gating strategies of flow cytometry analysis are reported in Supplementary Fig. 2.

Cell proliferation assay

KC or KPC cells were seeded in a 96-well plate at a density of 1×10^4 cells per well in technical triplicate. After 4, 24, 48 and 72 h of culture, 10 µl per well of WST-1 reagent (Abcam) was added and cells were incubated for 30 min in standard culture conditions. After incubation, OD values (450 nm) were acquired at Multiskan GO Microplate Spectrophotometer (Thermo Scientific) and proliferation was calculated as fold change over the 4 h.

RT-qPCR

Total RNA was extracted using the ReliaPrep RNA Cell Miniprep System (Promega) and quantified with NanoDrop 8000. Single-stranded cDNA was synthesized using ImProm-II Reverse Transcription System (Promega) starting from 400-500 ng total RNA. For monocytes isolated from total bone marrow, cDNA was synthesized using SuperScript II (Thermo Scientific), amplified via PCR with KAPA HiFi HotStart (Roche) and purified with AMPure XP beads (Thermo Scientific). Sample concentration was assessed by Qubit 3.0 and size distribution by an Agilent 4200 Tapestation system. Amplification of target genes was performed with Fast SYBR Master Mix on a ViiA7 Real-Time PCR System. A complete list of primer pairs used is reported in the Supplementary Table 4.

Analyses of cell culture supernatant

Mouse BMDMs, bone marrow monocytes and tumour cells were stimulated as indicated. For quantification of IL-1β, mouse BMDMs and bone marrow monocytes were stimulated for 4 h as indicated and ATP (5 mM) was added for the last 30 min of stimulation. Supernatants were collected and centrifuged to remove cellular debris. IL-1β (Mouse IL-1 beta Uncoated ELISA, Invitrogen) and M-CSF (DuoSet ELISA Mouse M-CSF; R&D) were measured following manufacturer's instructions. Absorbance was measured on a Multiskan GO Microplate Spectrophotometer. Other human and mouse cytokines were measured using Bio-Plex Pro Mouse Chemokine 31-Plex Assays (Bio-Rad) and Bio-Plex Pro Human Cytokine Screening Panel, 48-Plex (Bio-Rad), according to the manufacturer's indications. Acquisition was performed using Luminex instruments and analysed with Bio-plex manager (Bio-Rad) software.

PGE_2 levels were quantified either in the supernatants of human tissue samples, obtained as described above, or in the supernatants of KC, KPC and Panc02 cell lines. PDAC cells were seeded at 1×10^6 cells per 10-cm dish and cultured for 24–48 h in 6 ml of complete medium. Supernatants were collected and centrifuged to remove cellular debris. PGE_2 (Prostaglandin E_2 Express ELISA kit, Cayman Chemical) was measured following manufacturer's instructions. Absorbance was measured on a Multiskan GO Microplate Spectrophotometer. When indicated, PGE_2 levels were normalized by tissue weight.

Extraction of prostaglandins by solid phase extraction purification

Prostaglandins were extracted as previously described[58] with minor modifications. In brief, 35 mg of tissue was homogenized in 3 ml of 15% methanol in water at pH 3 (containing formic acid 0.04%) containing PGE_2-d4 and PGD_2-d4 (40 ng each) as internal standards and 0.005% BHT to prevent prostaglandin oxidation, using an electric pestle. The homogenate was then vortexed for 5 min and subjected to 10 min of centrifugation (2,000*g*) at 4 °C to remove the precipitated proteins. The supernatant was loaded onto an OASIS HLB prime vac Cartridge (3cc) and allowed to completely enter the packing material. The cartridge was washed with 3 ml 15% methanol and 3 ml water. The prostaglandins were eluted from the cartridge with 3 ml ethyl acetate containing 1% methanol. The eluted samples were dried under nitrogen and resuspended with 50 µl acetonitrile:water (1:2) and stored at −20 °C until liquid chromatography–tandem mass spectrometry (LC–MS/MS) analysis. For PGE_2 and PGD_2 absolute quantification, calibration curves were prepared by spiking increasing amount of PGA1 (from 0.0625 ng to 625 ng) in the same sample matrix (mouse or human control sample). The calibration curve point samples were then processed as described above, including the addition of PGE_2-d4 and PGD_2-d4 (40 ng each) for the extraction yield correction.

Chromatographic separation of PGE_2 and PGD_2 and their LC–MS/MS detection

Samples were directly analysed using the UPLC 1290 (Agilent Technologies) coupled to the TripleTOF 5600+ mass spectrometer (SCIEX) (ProMeFa, Proteomics and Metabolomics Facility, Ospedale San Raffaele, Milan, Italy). Chromatographic separations occurred on C18 column (ACQUITY UPLC HSS T3 Column, Waters, 1.8 µm, 2.1 mm × 100 mm) by directly injecting 10 µl of samples (1/5 of the original sample). Metabolites were separated using a flow rate set at 0.4 ml min^{-1} and a gradient of solvent A (water, 0.1% formic acid) and solvent B (acetonitrile, 0.1% formic acid). The gradient, in negative mode, started from 25% B hold for 2 min; increased up to 40% B in 16 min; increased again up to 90% in 1 min; maintained constant at 90% B for 4 min; decreased to 25% B in 1 min and maintained at 25% for 2 min. The column was set at 50 °C while the samples were kept at 4 °C. Full scan spectra were acquired in the mass range from *m/z* 50 to 500. Automated calibration was performed using an external calibrant delivery system which infuses APCI negative calibration solution every 5 samples injection. A product ion experiment mode was used to monitor PGE_2 and PGD_2 mass (at 351.2 *m/z*) as well as internal standards PGE_2-d4 and PGD_2-d4 (355.4 *m/z*). PGA1 at 335.4 *m/z* was followed for the calibration curves. The source parameters were: gas 1: 33 psi, gas 2: 58 psi, curtain gas: 25 psi, temperature: 500 °C and ion spray voltage floating: −4,500 V, DP: −80 V, CE: 44 V.

Immunofluorescence staining

For immunofluorescence analysis of macrophage spatial distribution, tissues were fixed overnight in 4% paraformaldehyde at 4 °C, washed in PBS and placed in 30% sucrose for 12–24 h. Afterwards, tissues were placed in a 2:1 mixture of 30% sucrose and optical cutting temperature (OCT) compound (Bio Optica, 05-9801) for 30 min at 4 °C, embedded in OCT and snap frozen in dry ice. The 10-µm cryostat sections were fixed in paraformaldehyde (4% in PBS) at room temperature for 20 min, washed 3 times in 0.05% PBS-Tween (PBS-T) and incubated with blocking buffer (0.05% PBS-T + 0.3% Triton X-100 + 5% BSA) at room temperature for 1 h. Sections were stained overnight at 4 °C with the following primary antibodies: rat anti-mouse F4/80 (Abcam ab6640, 1:200) or rabbit anti-mouse F4/80 (Abcam ab30042, 1:500), goat anti-mouse IL-1β (R&D Systems AF-401-NA, 1:100), rat anti-mouse FOLR2 (BioLegend 153302, 1:100), rabbit anti-mouse KRT19 (Abcam ab52625, 1:500), goat anti-mouse CD31 (R&D Systems AF3628, 1:500), rat anti-mouse VEGFR2 (BD Pharmingen 550549, 1:100) or rabbit anti-mouse PDGFRα (Abcam ab203491, 1:500). Sections were washed three times in 0.05% PBS-T, and incubated with the following secondary antibodies: donkey anti-rat IgG Alexa Fluor Plus 488 (Invitrogen A48269, 1:500), donkey anti-goat IgG Alexa Fluor Plus 555 (Invitrogen A32816, 1:500), donkey anti-rabbit IgG Alexa Fluor Plus 647 (Invitrogen A32795, 1:500). After three washes in 0.05% PBS-T, cell nuclei were stained with DAPI (Sigma-Aldrich Merck, MBD0015) at room temperature for 15 min and coverslips were mounted onto slides with FluorSave Reagent (Sigma-Aldrich Merck, 345789). Digital images were acquired on a MAVIG RS-G4 scanning confocal microscope (Caliber I.D.) using a 20× air objective or a 40× oil objective.

Immunofluorescence analysis of macrophage spatial distribution

Quantitative analysis of immunofluorescence images was performed using QuPath v0.4.1[59]. For each image, tissue-specific expression of cytokeratin 19 (KRT19) was used to annotate tumour areas and discriminate them from the adjacent stroma. Equally sized ROIs were randomly selected within the annotated 'tumour' ($DAPI^+KRT19^+$) or 'stromal' ($DAPI^+KRT19^-$) areas. Within each ROI, cell segmentation was performed using the 'cell detection' command based on the nuclear DAPI stain and thresholds were applied on fluorescence signals to create classifiers for cell-type identification. Specifically, F4/80 signal was used to classify cells as macrophages and compute their abundance in annotated ROIs. Similarly, the macrophage classifier was combined with classifiers based on IL-1β and FOLR2 signals to detect double-positive cells. Quantification was performed by computing the frequency of $F4/80^+$, $F4/80^+IL\text{-}1\beta^+$ and $F4/80^+FOLR2^+$ cells in $n = 10$–20 ROIs per tissue section, equally distributed between tumour and stromal compartments. Additionally, the frequency of macrophages was quantified in normal adjacent tissue from orthotopic PDAC mice and in healthy pancreas from wild-type controls. For distance analysis, the frequency of $F4/80^+IL\text{-}1\beta^+$ and $F4/80^+FOLR2^+$ macrophages was calculated within concentric partitioning rings annotated around the tumour margin (identified by KRT19 staining), with a cumulative 50-µm expansion in the adjacent stroma. The same parameters for segmentation and cell-type classification were applied to all samples from the same experiment.

Immunofluorescence analysis of IL-1β$^+$ TAMs in areas of angiogenesis

Quantitative analysis of IL-1β$^+$ TAMs in areas of angiogenesis was carried out with QuPath v0.4.1. Cell segmentation was performed on whole-tissue sections (comprising tumour and stroma) using the 'Cell detection' command based on the nuclear DAPI stain and object classifiers were set up to detect $CD31^+VEGFR2^+$ endothelial cells. The 'Density map' command was then used to split the tissue section into areas with 'high' and 'low' density of $CD31^+VEGFR2^+$ endothelial cells, and quantify the frequency of $F4/80^+IL\text{-}1\beta^+$ cells within these discrete tissue annotations.

Immunofluorescence analysis of IL-1β$^+$ TAMs in areas of hypoxia

Tumour hypoxia was labelled in vivo with Hypoxyprobe, following the manufacturer's instructions. In brief, pimonidazole (Hypoxyprobe-1, 60 mg kg^{-1} of body weight) was intraperitoneally injected in end-stage orthotopic KPC-bearing mice 60 min before euthanasia. Fresh tumour biopsies were washed in PBS, embedded in OCT compound and snap frozen in dry ice. Ten-micrometre cryostat sections were processed for immunofluorescence staining as described above, using the following primary antibodies: rat anti-mouse F4/80 (Abcam ab6640, 1:200), rabbit anti-mouse KRT19 (Abcam ab52625, 1:500), goat anti-mouse IL-1β (R&D Systems AF-401-NA, 1:100), anti-pimonidazole (Hypoxyprobe PAb2627AP, 1:20). Digital images were acquired on a MAVIG RS-G4 scanning confocal microscope (Caliber I.D.) using a 20× air objective.

Quantitative analysis was carried out with QuPath v0.4.1, by performing DAPI-based cell segmentation of the whole tumour and stroma and using the 'Density map' command to define annotations comprising areas with high density of cells stained for Hypoxyprobe. The ensuing density maps were then used to annotate tissue regions as 'hypoxic' or 'non-hypoxic' and quantify the frequency of $F4/80^+$ $IL\text{-}1\beta^+$ cells within these compartments.

Immunohistochemistry staining of human PDAC

Immunohistochemistry staining of human PDAC tissue was performed using the Discovery Ultra (Roche/Ventana) platform. In brief, 5-µm tissue sections collected from FFPE blocks of human PDAC were deparaffinized, subjected to antigen retrieval with Discovery CC1 solution (Roche/Ventana, 950-500) for 60 min and blocked with Discovery Inhibitor (Roche/Ventana, 760-4840) for 8 min. Tissue sections were sequentially stained for 30 min at room temperature with the following primary antibodies: rabbit anti-human NLRP3 (Sigma-Aldrich Merck HPA012878; 1:150), mouse anti-human CD163 (MRQ-26, Cell Marque 163M-18, pre-diluted), mouse anti-human FOLR2 (Invitrogen MA5-26933, 1:100), mouse anti-human cytokeratin 8 and 18 (B22.1 and B23.1, Cell Marque 818M-90, pre-diluted). For each staining cycle, incubation with primary antibody was followed by incubation with Discovery UltraMap anti-Ms HRP (Roche/Ventana, 760-4313) or Discovery UltraMap anti-Rb HRP (Roche/Ventana, 760-4315) for 20 min at room temperature, and then with one of the following fluorophores at 1:100 dilution for 4-8 min at room temperature: Discovery FITC kit (Roche/Ventana, 760-232), Discovery Red 610 kit (Roche/Ventana, 760-245), Discovery Cy5 (Roche/Ventana, 760-238). Tissue sections were neutralized with Discovery Inhibitor at the end of each staining cycle to avoid cross-reactivity. Finally, tissue sections were counterstained with DAPI and coverslips were mounted onto slides using Vectashield Antifade Mounting Medium (Vector Laboratories, H-1000-10). Digital images were acquired on a MAVIG RS-G4 scanning confocal microscope (Caliber I.D.) using a 20× air objective.

Western blot analyses

Cells were lysed in RIPA lysis buffer, containing 10 mM Tris-HCl pH 8, 1 mM EDTA pH 8, 140 mM NaCl, 1% Triton X-100, 0.1% SDS, 0.1% deoxycholate and protease and phosphatase inhibitors. Protein concentrations were measured with the Pierce BCA Protein Assay Kit. Lysates were then electrophoresed on Tris-glycine SDS–PAGE gels and transferred on nitrocellulose membranes (Amersham Protran Premium 0.45 µm NC). Membranes were blocked in PBS-T buffer added with 5% BSA or 5% milk (1 h at room temperature), followed by overnight incubation with primary antibodies at 4 °C: anti-IκBα (9242 S, Cell Signaling, 1:1,000), anti-IL1R1 (ab229051, Abcam, 1:1,000) and anti-COX2 (160106, Cayman Chemical, 1:100). The following day, membranes were washed and incubated for 1 h at room temperature with HRP-conjugated secondary antibody. Membranes were developed either with Clarity Western ECL Substrate (Bio-Rad) or Westar Supernova (Cyanagen). Protein loading was assessed by detection with anti-β-actin (A1978, Sigma-Aldrich, 1:2,000) or anti-vinculin (13901 S, Cell Signaling, 1:1,000). Western blot analyses were performed using Image Lab Software v6.1. Uncropped and unprocessed scans of western blots are reported in Supplementary Fig. 1.

Generation and processing of scRNA-seq data

Data generation. Human and mouse samples were collected and dissociated as described above. For the patient LiMeT PDAC15, cells were enriched in the myeloid fraction as $CD45^+CD3^-CD19^-$ by sorting (FACSAria, BD Biosciences). For heterotopic and orthotopic KC tumours, cells were enriched in the myeloid fraction as $CD45^+Cd11b^+$ via sorting and scRNA-seq libraries generated using the Chromium Single Cell 3' Reagent Kit v2, according to the manufacturers' instructions. For mouse KPC organoids, Matrigel domes containing the organoids were dissolved in Cell Recovery Solution (Gibco) for 30 min on ice, manually inverting the tubes every 5 min. After addition of cold splitting medium, organoid suspension was centrifuged and supernatant was removed prior to incubation in TrypLE Express (Gibco) for 20 min on an orbital shaker at 37 °C. The larger cellular aggregates were allowed to settle by gravity, and the single-cell suspension was collected from the supernatant without interfering with the lower fraction. Upon centrifugation at 400*g* for 5 min at 4 °C, cells were resuspended in ultrapure BSA (400 µg ml^{-1}) (Invitrogen) for downstream processing.

Unless otherwise stated, scRNA-seq libraries were generated using a microfluidics-based approach on Chromium Single-Cell Controller (10X Genomics) using the Chromium Single Cell 3' Reagent Kit v3.1, according to the manufacturers' instructions. In brief, single cells were partitioned in gel beads in emulsion (GEMs) and lysed, followed by RNA barcoding, reverse transcription and PCR amplification (13–15 cycles). The concentration of the scRNA-seq libraries was determined using Qubit 3.0 and size distribution was assessed using an Agilent 4200 TapeStation system. Libraries were sequenced on an Illumina NovaSeq 6000 instrument (paired-end, 150 bp read length).

Data processing. Fastq files were processed with Cell Ranger (v 4.0.0)[60], using default parameters. Reads were aligned to reference genome mm10 for mouse samples and hg38 for human samples (references version 2020-A, 10X Genomics). Only confidently mapped reads with valid barcodes and unique molecular identifiers (UMIs) were retained to compute a gene expression matrix containing the number of UMI for every cell and gene. Gene counts were imported in R environment (v 4.0.3) and processed with Seurat (v 4.0.3). When creating the Seurat object, genes expressed in less than 3 cells were removed. Putative doublets were identified and discarded using scDblFinder R package (v 1.4.0)[61] by imputing doublet rates (dbr) equal to 0.07 for mouse sample and 0.05 for human samples. Dbr were established in agreement with the number of loaded cells and following the 10X Genomics guidelines. Cells expressing less than 1,000 UMI counts were discarded. Cells expressing less than 200 genes (mouse sample), or less than 500 genes (human sample) were also excluded. Lastly, cells with a ratio of mitochondrial versus endogenous genes expression exceeding 0.25 (mouse sample) or 0.40 (human sample) were discarded. Raw expression data were normalized applying $\log_2$ transformation with NormalizeData function, scaled using ScaleData function, regressing on percentage of mitochondrial gene expression and cell cycle scores, previously computed using CellCycleScoring function. The top 3,000 genes with the highest standardized variance were computed using FindVariableFeatures function (selection.method = "vst"). Principal component analysis (PCA) was computed using RunPCA function with default parameters.

Batch correction. PCA embeddings were corrected for sample batch by applying alternative algorithms to the same Seurat object through the Seurat Wrapper package (v 0.3.0). For both human and mouse data, when analysing the whole or tumour cells dataset, batch effect was corrected employing matching mutual nearest neighbour (MNN) algorithm[62], implemented by RunFastMNN function using default parameters. For the analysis of mononuclear phagocytes and TAMs, batch correction was achieved with the Harmony algorithm (v 0.1.0)[63], implemented by RunHarmony function using the first 30 PCA dimensions and default theta (theta = 3 for human dataset).

Graph-based clustering and differential gene expression analyses. Shared nearest neighbour (SNN) graph was computed using the FindNeighbors function, taking as input the first 20 PCA dimensions. Cell clusters were defined using Louvain algorithm with the FindCluster function. For visualization in two dimensions uniform manifold approximation and projection (UMAP)[64] was used. Cluster-specific

genes were identified using FindAllMarkers function with option only.pos = TRUE and min.pct = 0.1, setting a cut-off of FDR < 0.01.

Inference of copy number variants. Single-cell copy number variants were inferred using CopyKAT R package (v 1.0.5)[65]. CopyKAT estimates the genome copy number profile of single cells employing an integrative Bayesian segmentation approach combined with hierarchical clustering to identify putative aneuploid cells. CopyKAT was run separately on each human sample, taking the raw count matrix of all cells as input and adjusting the segmentation parameter KS.cut to either 0.1 or 0.15 according to data quality.

Human–mouse comparison of TAM clusters. We performed a pre-ranked GSEA analysis with clusterProfiler R package (v 3.18.1)[66] on mouse TAM genes ranked by log_2FC (each TAM subset vs other TAMs) using as gene sets mouse orthologues of human TAMs marker genes obtained using biomaRt (v 2.46.3)[67] database. To identify shared signatures for each human and mouse TAM cluster, we computed overlaps between marker genes identified using logfc.threshold = 0.8.

RNA velocity and single-cell trajectories. Mouse classical monocytes and TAMs from pancreatic and blood samples were analysed together as previously described. Batch effect correction was performed by MNN algorithm[62], using the RunFastMNN function with default parameters. The first 20 MNN-corrected principal components were used to compute the two-dimensional embedding using the diffusion map-based algorithm Palantir[68], implemented with the RunPalantirDiffusionMap function from SeuratExtend R package (v 0.4.2). Cell clusters were defined according to marker-based manual annotation previously done on each dataset. The Seurat object was then converted into Scanpy format (v 1.6.0)[69] using SeuratDisk (v 0.0.0.9019) and the following analyses were performed in Python environment (v 3.6.10). To annotate spliced and unspliced reads, cell-barcode sorted bam files from Cell Ranger output were processed using Velocyto pipeline (v 0.17.17)[70]. The scVelo Python package (v 0.2.2)[71] was used to compute RNA velocity vectors for each gene, employing dynamical modelling to estimate splicing kinetics. Using CellRank package (v 1.2.0)[20], RNA velocity and transcriptomic similarity information were combined in single kernel to compute a cell-cell transition matrix. Generalized Perron cluster cluster analysis (GPCCA) estimator[72] was used to identify macrostates. Terminal states were inferred by inspecting the coarse-grained transition matrix and were then used to compute absorption probabilities. Focusing on the classical monocyte–*Il1b*$^+$ TAM lineage, genes whose expression correlates with absorption probabilities towards *Il1b*$^+$ TAMs terminal state were identified as potential lineage drivers.

Optimal transport analysis. To infer cell trajectories, we applied Waddington optimal transport[19] on our scRNA-seq mouse time-course data. Optimal transport model was fit to classical monocytes and TAMs from pancreatic and blood samples, setting $\varepsilon = 0.05$, $\lambda 1 = 1$ and $\lambda 2 = 50$ to compute transport maps. Based on them, we computed cell fate probabilities using cell populations at day 30 as endpoint.

Gene set enrichment analysis. Hallmarks gene sets were retrieved from msigdbr (v 7.5.1)[73]. For GO biological processes gene sets, we used org.Hs.eg.db (v 3.12.0) and org.Mm.eg.db (v 3.12.0) as genome wide annotations for human and mouse respectively. Gene sets of cytokine-induced signatures were derived from in vitro stimulation experiments on mouse bone marrow-derived macrophages[22,25] (Supplementary Table 4).

IL1B gene expression in human cell types. To evaluate the expression of *IL1B* across all human cell types, we reanalysed scRNA-seq data including neutrophils in the dataset. Neutrophils were retrieved lowering the cut-offs on UMI counts and genes per cell to 500 and 100, respectively. Data were processed as previously described, with the exception that counts were normalized with SCTransform function in Seurat.

Re-analysis of human PDAC cells in naive samples. Tumour cells from untreated participants were analysed separately as previously described. We computed new embedding and clustering on cells showing variable expression of the T1RS signature (clusters 1,3,5 at resolution 0.3) and then we performed trajectory analysis with slingshot[31] (v. 1.8.0) on the MNN space. We correlated gene expression with pseudotime, computed with slingPseudotime function. To evaluate if cell trajectory reflected the acquisition of the expression of T1RS signature we performed GSEA analyses on gene list ranked by correlation values. Finally, to define which ligand–receptor interaction in the crosstalk between IL1B$^+$ TAMs and tumour cells drives the acquisition of the T1RS gene expression pattern through the trajectory, we performed a cell-cell communication analysis with NicheNet[32] (v. 1.1.1). We interrogated NicheNet database using IL1B$^+$ TAMs as sender cells and tumour cells as receiver cells. Putative ligands were selected filtering for genes expressed in IL1B$^+$ TAMs subset (percentage of cells > 15% and log_2FC(IL1B$^+$ TAMs/other TAMs) > 0.5), while putative receptors were selected filtering for genes expressed in the tumour cells (percentage of cells > 15% in clusters 1,3 and 5). We used markers of the cluster at the endpoint of the trajectory (log_2FC > 1 and min.pct = 30%) as target genes for ligand prioritization.

scRNA-seq datasets collected in this study. We collected published scRNA-seq data on human PDAC and normal adjacent tissue (CRA001160)[27]; immune cells from idiopathic or hereditary pancreatitis and normal pancreas (GSE165045)[30]; pancreatic epithelial cells from GEMMs of PDAC progression (GSE207943)[28]. For these datasets we downloaded: raw fastqs, raw count matrices and normalized counts, respectively. Data were processed as previously described.

scRNA-seq dataset from patients with pancreatitis. Raw counts matrices of immune cells from idiopathic or hereditary pancreatitis and normal pancreata were filtered to discard cells expressing less than 200 genes, less than 1,000 UMIs and with a ratio of mitochondrial versus endogenous genes expression exceeding 0.20. Cells were processed as previously described, using 2,000 variable features. For the analysis of macrophages, anchoring-based transfer learning[74] was used to perform annotation, using our TAM dataset as reference. Anchors for transfer learning were computed using the FindTransferAnchors Seurat function. Reference labels were then projected onto query macrophages using the TransferData function. Macrophages from pancreatitis and donor pancreata were annotated according to our reference classification if the prediction score exceeded 0.75, otherwise were left unlabelled.

scRNA-seq datasets from other mouse models. scRNA-seq datasets from GEMM mouse models and wild-type and COX2-KO KPC were processed as previously described. For scRNA-seq data derived from heterotopic and orthotopic KC tumours we corrected batch effect employing Harmony algorithm (v 0.1.0)[63], implemented by RunHarmony function using the first 30 PCA dimensions and theta = 1. For the reclustering of mononuclear phagocytes, batch correction was achieved with the Harmony algorithm (v 0.1.0) on the first 30 PCA dimensions and default theta. Differentially expressed genes in the comparison between cells from wild-type and COX2-KO tumours were computed using FindAllMarkers function with option only.pos = FALSE, min.pct = 0.1, setting a cut-off of FDR < 0.01 and average log_2FC > 0.5.

Generation and processing of spatial transcriptomic data

Visium spatial gene expression. Data generation. Spatial transcriptomics data were generated using the Visium Spatial Gene Expression Reagent Kits (10X Genomics) according to the manufacturer's

instruction. Tumour biopsies from day 30 orthotopic PDAC mice were gently washed in PBS, snap frozen via bathing in liquid nitrogen-chilled isopentane and embedded in OCT compound. Five to ten sections were collected to evaluate RNA quality at TapeStation system (Agilent). The tissue blocks were then processed to retrieve 2 non-sequential 10 µm sections (100 µm apart), which were placed within the 6.5 × 6.5 mm capture areas of a Visium slide equilibrated at cryostat temperature (−20 °C). Sections were immediately fixed in chilled methanol at −20 °C for 30 min and stained via immunofluorescence using buffers supplemented with Recombinant RNase inhibitor (Takara 2313 A, 2 U μl^{-1}) to prevent RNA degradation. Whole-slide images were acquired using the MAVIG RS-G4 (Caliber I.D.) confocal microscope at 20× magnification. Barcoded libraries were generated by permeabilizing tissue sections at 37 °C for 15 min and performing in situ reverse transcription at 53 °C for 45 min, followed by second-strand synthesis at 65 °C for 15 min. cDNA was denatured and transferred to tubes for PCR amplification and library construction, including fragmentation, adapter ligation and sample indexing. The quality of both amplified cDNA and final libraries was determined at TapeStation system (Agilent). Visium libraries were sequenced on an Illumina NovaSeq 6000 instrument (paired-end, 150 bp read length).

Data processing. Spatial transcriptomic data were aligned to their corresponding immunofluorescence image, using SpaceRanger (v 1.2.0) with default parameters. We excluded spots with a number of UMI lower than 100 and without DAPI staining in the corresponding overlaid image, resulting in a dataset of 3,274 and 3,496 spots for A1 and B1 sections, respectively. To infer cell-type proportions within each spot, we performed cell-type deconvolution using DestVI (v 0.1)[75]. We first trained the single-cell latent variable model (scLVM) on the scRNA-seq dataset obtained by retaining transcriptomic data from samples collected 30 days post-tumour inoculation, analysed and annotated as described previously. We then trained the spatial transcriptomic latent variable model on the spatial transcriptomic dataset and we computed cell-type proportions for each spot with get_proportions() function. To assess spatial variability of macrophage transcriptome, spatial transcriptome spots enriched in monocytes and macrophages were selected using the default secondary cut-off, set by DestVI on their proportion distributions, obtaining a dataset of 671 spots for A1 and 1,119 spots for B1. We computed the gamma latent space with get_gamma() function, obtaining 5 gamma values, and the Spatial Principal Components (Spatial PCs) using the get_spatial_components() function. Finally, gene expression values were imputed using get_scale_for_ct() function, extracting six different gene expression matrices from the negative binomial distribution, as predicted by the trained scLVM applied to spatial transcriptome latent space. The mean gene expression values computed on these expression matrices were used for downstream analysis. Spot enrichments for specific gene sets were evaluated using runPAGEEnrich() function from Giotto R package (v 1.1.2)[76]. For A1 spatial transcriptome dataset, we performed clustering analysis with Seurat package (v 4.2.0): spot read counts were normalized with SCTransform() function and PCA performed with RunPCA() function. Top 20 PCs were used to obtain clusters at 0.3 resolution using FindNeighbors() and FindClusters() functions. Marker genes of spots belonging to cluster 4 or cluster 6 were ranked by $\log_2$FC and used to perform GSEA analysis for selected GO Biological Processes.

Annotation of spatial transcriptome spots. Single-channel grayscale immunofluorescence images for sections A1 and B1 were imported in CellProfiler (v. 4.1.3)[77], rescaled using RescaleIntensity() function, and imported as composite images in Squidpy (v 1.2.3)[78]. DAPI-based cell nuclei detection was carried out with Stardist (v 0.8.3)using the pre-trained 2D versatile algorithm for fluorescence data, to create mask binary files. In parallel, single-channel image crops were generated for every spatial transcriptome spot. Resulting images and masks were exported to Cell Profiler, where nuclei were filtered based on size and cell boundaries were reconstructed using the 'distance' option. A median filter was applied to F4/80, PDGFRa and KRT19 signal intensity to classify cells as positive or negative for each individual marker. Results were exported to R, double- and triple- positive cells were filtered out, and the fraction of single F4/80$^+$, PDGFRa$^+$ or KRT19$^+$ cells was calculated for all the spots. Finally, spatial transcriptome spots were annotated as 'tumour' or 'stroma', according to transcript or protein expression obtained from spatial transcriptome or immunofluorescence data, respectively. For immunofluorescence-based annotation, the percentage of KRT19$^+$ cells as calculated by CellProfiler was used to classify spots as tumour (per cent of KRT19$^+$ ≥ 60%) or stroma (per cent of KRT19$^+$ < 60%). For spatial transcriptome-based annotation, DestVI deconvolution output was used to define tumour spots as those where the sum of percentages of cancer, ductal and acinar cells was ≥60%. Similarly, stromal spots were defined as those where the sum of endothelial cells and cancer-associated fibroblasts was ≥40%. Spots that did not fall in these two categories, were annotated as tumour or stroma according to the most enriched cell type.

Molecular Cartography. Data generation. Ten-micrometre sections were collected from fresh frozen PDAC tissues, placed within the capture areas of cold slides, and sent to Resolve Biosciences on dry ice for sample processing. Upon arrival, tissue sections were thawed, fixed with 4% Formaldehyde (Sigma-Aldrich F8775) in PBS for 20 min at 4 °C, and used for Molecular Cartography (100-plex combinatorial single molecule fluorescence in situ hybridization) according to the manufacturer's instructions (protocol 1.3; available for download from Resolve's website for registered users). In brief, tissue sections were hybridized at 37 °C for 24 h with oligonucleotides probes specific for the selected target genes (see Supplementary Table 9). Probes were designed using Resolve's proprietary algorithm, as previously reported[79]. Afterwards, probe binding was revealed with fluorescent tags in a multi-step automated imaging process, repeating colour development, imaging and decolorization for a total of 8 cycles on a Zeiss Celldiscoverer 7 instrument, using a 50× water immersion objective. The resulting raw data images were pre-processed for background correction, aligned to perform spot segmentation, analysed to decode the resulting signals and to finally assign each detected transcript to *xyz* coordinates, as previously reported[79].

Cell segmentation. We segmented cell nuclei in the DAPI image with Cellpose[80] (v. 2.2) using the pre-trained nuclei model, with automated estimation of diameter parameter. Subsequently, cells were segmented on transcript coordinates with Baysor[81] (v. 0.5.0) using DAPI segments as prior with the following parameters: –n-clusters 1–prior-segmentation-confidence 0.2 -m 3. Finally, we computed cells outlines by applying the convex hull algorithm, using chull R function, on transcripts assigned to each individual cell by Baysor.

Cell filtering and annotation. We imported Baysor output files and segmentation into a Seurat object with a custom function. Cells expressing less than 4 genes or more then 25 genes, along with cells with less than 10 transcripts were discarded. Gene counts were normalized with SCTransform Seurat function with clip.range set form −10 to 10. Then, we performed PCA and we computed clustering and dimensionality reduction as previously described for scRNA-seq data. Finally, we computed markers for all cluster and annotated cell types.

Spatial neighbourhood analysis. For each cluster we defined a set of cells in its spatial neighbourhood, then we computed which clusters were significatively over-represented in this neighbourhood set. In brief, for each cell we computed k-nearest neighbours within spatial coordinates space using kNN function from dbscan R package[82] (v. 1.1-11), with *k* set to 40 and maximum distance set to 400 pixels. We selected the set of nearest neighbours of all cells belonging to the same cluster and we counted the number of cells from all different cluster within this set of nearest neighbours. We then computed significance using randomly annotated data as null distribution. Specifically, we reannotated cells randomly 1,000 times, maintaining cluster

dimensionality and, for each randomization, we computed again the number of cells from all clusters in the set of nearest neighbours of each cluster.

Spatial correlation of gene expression. We computed gene expression spatial correlation of all genes with CXCL1. First, we computed the spatial lag expression vector of CXCL1[83]. Lag expression vector of a gene reports for each cell the summed expression of its *k*-nearest neighbours. In brief, we used lag.listw from spded R package (v. 1.2-8) to compute the spatial lag vector for CXCL1, considering for each cell its 20 nearest neighbours, with maximum distance set to 400 pixels, defined with the kNN function. We then correlated the real expression of each gene with the spatial lag vector of CXCL1. Genes that show high spatial correlation with CXCL1 are those genes that are more expressed in cells that are close to cells expressing CXCL1 at highest level.

Spatial transcriptomic datasets collected in this study. We downloaded raw count matrices of published GeoMX data[84] (GSE226829). We performed normalization with voom function of limma R package[85] (v. 3.46.0).

Generation and processing of bulk RNA-seq data

Data generation. Total RNA was purified using the ReliaPrep RNA Cell Miniprep System and RNA-seq libraries were generated using the Smart-seq2 method[86] with minor modification. In brief, 5 ng of RNA were retrotranscribed, cDNA was PCR-amplified (15 cycles) and purified with AMPure XP beads. After purification, the concentration was determined using Qubit 3.0 and size distribution was assessed using Agilent 4200 TapeStation system. Then, the tagmentation reaction was performed starting from 0.5 ng of cDNA for 30 min at 55 °C and the enrichment PCR was carried out using 12 cycles. Libraries were then purified with AMPure XP beads, quantified using Qubit 3.0, assessed for fragment size distribution on an Agilent 4200 TapeStation system. Sequencing was performed on an Illumina NovaSeq6000 (single-end, 75 bp read length) following manufacturer's instruction.

Data processing. Reads were aligned to the mm10 reference genome using STAR aligner (v STAR_2.5.3a)[87]. Read counts matrices were computed using the featureCounts function from Rsubread package (v 2.0.1)[88], using RefSeq *Mus musculus* transcriptome (mm10) annotation[89], setting minMQS option to 255. Further analyses were performed in R environment (v 3.6.3) with edgeR R package (v 3.28.1)[90]. Expressed genes read counts were normalized using the calcNormFactors function, with the trimmed mean of M-values (TMM) method[91]. The estimateDisp function was used to estimate dispersion. Differential gene expression across conditions was computed by fitting a negative binomial generalized linear model, with the glmQLFit function, followed by a quasi-likelihood *F*-test, with the glmQLFTest function, including sample replicates as covariates in the design matrix. Reads per kilo base per million (RPKM) values were computed for each gene with the rpkm function.

Definition of TNF-plus-PGE_2 synergized genes. RNA-seq data were generated and pre-processed as described above. Genes not passing the expression cut-off of RPKM > 1 in at least two samples in the dataset were filtered out. For each timepoint we defined TNF-PGE_2-inducible genes comparing expression levels in the TNF + PGE_2 condition versus untreated, PGE_2 alone or TNF-alone conditions, setting $\log_2$FC(RPKM) ≥ 1.5 and FDR < 0.01 as cut-offs. We also filtered out genes not reaching RPKM > 1.5 in at least 2 samples within each comparison. Finally, for each timepoint, we defined PGE_2–TNF synergized genes selecting genes passing previously defined cut-offs in all tested comparisons. For GSEA analysis we considered genes defined as PGE_2–TNF synergized in at least one timepoint.

Definition of T1RS gene signature. We analysed bulk and single-cell RNA-seq data on KC, KPC cells and KPC organoids stimulated with IL-1β in vitro. For each timepoint of stimulation, we defined IL-1β-inducible genes comparing expression levels in the IL-1β condition versus untreated, setting $\log_2$FC(RPKM) ≥ 1 and FDR < 0.05 as cut-offs. For each experimental condition we defined lists of IL-1β-inducible genes, selecting genes passing the defined cut-offs in at least one timepoint. Intersection of these gene lists led us to the identification of a set of genes commonly induced by IL-1β in all experimental conditions, namely the T1RS signature.

RNA-seq datasets collected in this study. We collected published RNA-seq data on pancreatic epithelial cells from *Kras*-wild-type and mutant *Kras* mice treated either with caerulein, IL-33 or left untreated (GSE132326, GSE154543)[15]; mouse pancreatic spheroids derived from pancreas either pre-exposed or not exposed to inflammation (GSE180211)[15]. For these datasets raw count matrices were downloaded and analysed as previously described. In addition, we collected published RNA-seq data of monocytes isolated from peripheral blood of patients with PDAC and healthy donors (E-MTAB-11190)[17]. For these data, fastq files were downloaded and processed as previously described, using hg38 as reference genome (reference version 2020-A, 10X Genomics).

TCGA data analyses. Using the TCGAbiolinks R package (v 2.23.2)[92], we downloaded transcriptomic data and clinical data from the pancreatic adenocarcinoma (PAAD) cohort for pancreatic cancer (n = 178). Survival analysis on primary tumour samples was performed using the survival (v 3.2-10) and survminer (v 0.4.9) R packages.

Survival analysis of TAM markers and T1RS genes in the PAAD cohort. To evaluate the prognostic significance of TAM marker genes, we obtained TAM cluster-specific genes by performing differential gene expression analysis (each TAM cluster vs other TAM clusters) and filtering for $\log_2$FC ≥ 1. On such gene lists, we evaluated MNP specificity by differential gene expression analysis, selecting genes with $\log_2$FC ≥ 2 in MNP compared to other cell types identified in our scRNA-seq data. The effect on patient prognosis was assessed by Cox beta regression coefficient on genes for which the fit was significant according to Wald test *P* values corrected for multiple testing. Univariate Cox regression model was fit for the expression of each gene or for the expression of each gene normalized for CD68 expression as continuous variables, for the evaluation of T1RS signature or TAM marker genes respectively.

Survival analysis on the IL1B$^+$ TAM gene signature. The six-gene prognostic signature for IL1B$^+$ TAMs, obtained as previously described, was used to stratified patients for survival analysis. The mean expression of the signature, normalized by CD68 expression, was used to group samples into high and low groups according to the upper and the lower quartile respectively. Cox regression model was fit to compare the high group against the low group, extracting the hazard ratio and its associated *P* value.

Association of T1RS and IL1B$^+$ TAM signatures. Using the TCGAbiolinks R package (v 2.28.3), we downloaded transcriptomic data and clinical data from the aforementioned cohort. We grouped patients based on the mean expression of the six-gene IL1B$^+$ TAM signature normalized by CD68 expression into high, intermediate and low groups according to the upper and the lower quartile of the score distribution. To examine association between IL1B$^+$ TAMs and T1RS signature, we then computed the mean of $\log_2$-transformed expression values of T1RS signature genes for each group of patients.

Cell-type deconvolution of TCGA PDAC samples. To estimate macrophage proportion in TCGA samples we used CIBERSORTx[93] online tool to deconvolute cell fractions using our annotated scRNA-seq

human PDAC dataset as reference. To build the signature matrix file, we first down-sampled our scRNA-seq human PDAC dataset, randomly selecting 200 cells for each annotated cell type. We then ran CIBERSORTx to generate cell-type signature matrices and impute the relative cell fractions in each tumour sample, enabling S-mode batch correction.

Quantification and statistical analyses

Results are illustrated as mean ± s.d. or mean ± s.e.m. Graphs show data from at least two independent repeats. Significance was defined as $P < 0.05$. Statistical analysis was conducted either using GraphPad Prism v9.0 (GraphPad Software) or R v3.4.1 (R project). Statistical tests, exact value of *n* and what *n* represents are mentioned in the figure legends. Statistical tests with adjustment for multiple comparisons and exact *P* values are reported in the Source Data.

Reporting summary

Further information on research design is available in the Nature Portfolio Reporting Summary linked to this article.

Data availability

Single-cell, spatial transcriptomic and bulk RNA-seq data have been deposited at NCBI GEO data repository under accession number GSE217847. Data reanalysed for this study are available under the following accession codes: CRA001160 (scRNA-seq of human PDAC and NAT), GSE165045 (scRNA-seq of patients with pancreatitis), GSE207943 (scRNA-seq of mouse PDAC GEMM), GSE226829 (GeoMX data of human PDAC), GSE132326 and GSE154543 (RNA-seq of epithelial cells from mouse PDAC), GSE180211 (RNA-seq of pancreatic spheroids), and E-MTAB-11190 (RNA-seq of blood monocytes from patients with PDAC). Source data are provided with this paper.

Code availability

Codes used for the analyses is available at https://github.com/ostunilab/PDAC_Nature_2023.

51. Olive, K. P. et al. Inhibition of Hedgehog signaling enhances delivery of chemotherapy in a mouse model of pancreatic cancer. *Science* **324**, 1457–1461 (2009).
52. Cappello, P. et al. Vaccination with ENO1 DNA prolongs survival of genetically engineered mice with pancreatic cancer. *Gastroenterology* **144**, 1098–1106 (2013).
53. Corbett, T. H. et al. Induction and chemotherapeutic response of two transplantable ductal adenocarcinomas of the pancreas in C57BL/6 mice. *Cancer Res.* **44**, 717–726 (1984).
54. Labun, K. et al. CHOPCHOP v3: expanding the CRISPR web toolbox beyond genome editing. *Nucleic Acids Res.* **47**, W171–W174 (2019).
55. Pelly, V. S. et al. Anti-inflammatory drugs remodel the tumor immune environment to enhance immune checkpoint blockade efficacy. *Cancer Discov.* **11**, 2602–2619 (2021).
56. Baker, L. A. & Tuveson, D. A. Generation and culture of tumor and metastatic organoids from murine models of pancreatic ductal adenocarcinoma. *Methods Mol. Biol.* **1882**, 117–133 (2019).
57. Milani, M. et al. Genome editing for scalable production of alloantigen-free lentiviral vectors for in vivo gene therapy. *EMBO Mol. Med.* **9**, 1558–1573 (2017).
58. Golovko, M. Y. & Murphy, E. J. An improved LC–MS/MS procedure for brain prostanoid analysis using brain fixation with head-focused microwave irradiation and liquid–liquid extraction. *J. Lipid Res.* **49**, 893–902 (2008).
59. Bankhead, P. et al. QuPath: open source software for digital pathology image analysis. *Sci. Rep.* **7**, 16878 (2017).
60. Zheng, G. X. et al. Massively parallel digital transcriptional profiling of single cells. *Nat. Commun.* **8**, 14049 (2017).
61. Germain, P. L., Lun, A., Garcia Meixide, C., Macnair, W. & Robinson, M. D. Doublet identification in single-cell sequencing data using scDblFinder. *F1000Res* **10**, 979 (2021).
62. Haghverdi, L., Lun, A. T. L., Morgan, M. D. & Marioni, J. C. Batch effects in single-cell RNA-sequencing data are corrected by matching mutual nearest neighbors. *Nat. Biotechnol.* **36**, 421–427 (2018).
63. Korsunsky, I. et al. Fast, sensitive and accurate integration of single-cell data with Harmony. *Nat. Methods* **16**, 1289–1296 (2019).
64. Becht, E. et al. Dimensionality reduction for visualizing single-cell data using UMAP. *Nat. Biotechnol.* **37**, 38–44 (2019).
65. Gao, R. et al. Delineating copy number and clonal substructure in human tumors from single-cell transcriptomes. *Nat. Biotechnol.* **39**, 599–608 (2021).
66. Yu, G., Wang, L. G., Han, Y. & He, Q. Y. clusterProfiler: an R package for comparing biological themes among gene clusters. *OMICS* **16**, 284–287 (2012).
67. Durinck, S., Spellman, P. T., Birney, E. & Huber, W. Mapping identifiers for the integration of genomic datasets with the R/Bioconductor package biomaRt. *Nat. Protoc.* **4**, 1184–1191 (2009).
68. Setty, M. et al. Characterization of cell fate probabilities in single-cell data with Palantir. *Nat. Biotechnol.* **37**, 451–460 (2019).
69. Wolf, F. A., Angerer, P. & Theis, F. J. SCANPY: large-scale single-cell gene expression data analysis. *Genome Biol.* **19**, 15 (2018).
70. La Manno, G. et al. RNA velocity of single cells. *Nature* **560**, 494–498 (2018).
71. Bergen, V., Lange, M., Peidli, S., Wolf, F. A. & Theis, F. J. Generalizing RNA velocity to transient cell states through dynamical modeling. *Nat. Biotechnol.* **38**, 1408–1414 (2020).
72. Reuter, B., Weber, M., Fackeldey, K., Roblitz, S. & Garcia, M. E. Generalized Markov state modeling method for nonequilibrium biomolecular dynamics: exemplified on amyloid beta conformational dynamics driven by an oscillating electric field. *J. Chem. Theory Comput.* **14**, 3579–3594 (2018).
73. Liberzon, A. et al. The Molecular Signatures Database (MSigDB) hallmark gene set collection. *Cell Syst* **1**, 417–425 (2015).
74. Stuart, T. et al. Comprehensive integration of single-cell data. *Cell* **177**, 1888–1902.e1821 (2019).
75. Lopez, R. et al. DestVI identifies continuums of cell types in spatial transcriptomics data. *Nat. Biotechnol.* **40**, 1360–1369 (2022).
76. Dries, R. et al. Giotto: a toolbox for integrative analysis and visualization of spatial expression data. *Genome Biol.* **22**, 78 (2021).
77. Stirling, D. R. et al. CellProfiler 4: improvements in speed, utility and usability. *BMC Bioinformatics* **22**, 433 (2021).
78. Palla, G. et al. Squidpy: a scalable framework for spatial omics analysis. *Nat. Methods* **19**, 171–178 (2022).
79. Guilliams, M. et al. Spatial proteogenomics reveals distinct and evolutionarily conserved hepatic macrophage niches. *Cell* **185**, 379–396.e338 (2022).
80. Stringer, C., Wang, T., Michaelos, M. & Pachitariu, M. Cellpose: a generalist algorithm for cellular segmentation. *Nat. Methods* **18**, 100–106 (2021).
81. Petukhov, V. et al. Cell segmentation in imaging-based spatial transcriptomics. *Nat. Biotechnol.* **40**, 345–354 (2022).
82. Hahsler, M., Piekenbrock, M. & Doran, D. dbscan: fast density-based clustering with R. *J Stat Softw* **91**, 1–30 (2019).
83. Bergenstrahle, J., Larsson, L. & Lundeberg, J. Seamless integration of image and molecular analysis for spatial transcriptomics workflows. *BMC Genomics* **21**, 482 (2020).
84. Carpenter, E. S. et al. Analysis of donor pancreata defines the transcriptomic signature and microenvironment of early pre-neoplastic pancreatic lesions. *Cancer Discov.* **13**, 1324–1345 (2023).
85. Ritchie, M. E. et al. limma powers differential expression analyses for RNA-sequencing and microarray studies. *Nucleic Acids Res.* **43**, e47 (2015).
86. Picelli, S. et al. Full-length RNA-seq from single cells using Smart-seq2. *Nat. Protoc.* **9**, 171–181 (2014).
87. Dobin, A. et al. STAR: ultrafast universal RNA-seq aligner. *Bioinformatics* **29**, 15–21 (2013).
88. Liao, Y., Smyth, G. K. & Shi, W. The R package Rsubread is easier, faster, cheaper and better for alignment and quantification of RNA sequencing reads. *Nucleic Acids Res.* **47**, e47 (2019).
89. Pruitt, K. D., Tatusova, T. & Maglott, D. R. NCBI reference sequences (RefSeq): a curated non-redundant sequence database of genomes, transcripts and proteins. *Nucleic Acids Res.* **35**, D61–65 (2007).
90. Robinson, M. D., McCarthy, D. J. & Smyth, G. K. edgeR: a Bioconductor package for differential expression analysis of digital gene expression data. *Bioinformatics* **26**, 139–140 (2010).
91. Robinson, M. D. & Oshlack, A. A scaling normalization method for differential expression analysis of RNA-seq data. *Genome Biol.* **11**, R25 (2010).
92. Colaprico, A. et al. TCGAbiolinks: an R/Bioconductor package for integrative analysis of TCGA data. *Nucleic Acids Res.* **44**, e71 (2016).
93. Newman, A. M. et al. Determining cell type abundance and expression from bulk tissues with digital cytometry. *Nat. Biotechnol.* **37**, 773–782 (2019).

Acknowledgements The authors thank M. A. Cappelluti and A. Lombardo for help with CRISPR–Cas9 gene targeting experiments; G. Bhat and D. Bonanomi for help with immunofluorescence analyses; C. Garlanda for providing *Il1r1*$^{-/-}$ mice; I. Zanoni, G. Natoli, B. Amati, A. Hidalgo, A. Ditadi and all members of the R.O. laboratory for discussions and/or critical reading of the manuscript. We thank the following Centers and facilities of Ospedale San Raffaele: Center for Omics Sciences (COSR), Proteomics and Metabolomics Facility (ProMeFa), Flow cytometry Resource, Advanced Cytometry Technical Applications Laboratory (FRACTAL), Advanced Light and Electron Microscopy BioImaging Center (ALEMBIC); Preclinical Imaging Facility, Centro Risorse Biologiche (CRB-OSR); Centro Universitario di Statistica per le Scienze Biomediche (CUSSB) at Vita-Salute San Raffaele University. Figures were created with Adobe Illustrator and BioRender.com. F.M.V., L.M. and V. Cuzzola conducted this study as partial fulfilment of a PhD in Molecular Medicine at Vita-Salute San Raffaele University. F.L.T. and C.L. conducted this study as partial fulfilment of a PhD in Complex Systems for Quantitative Biomedicine at University of Turin. N.C. and E.M. received support from fellowships from Fondazione Umberto Veronesi (FUV). P. Cappello and F.N. are supported by grants from the Italian Association for Cancer Research (AIRC) (IG 19931 and 26341) and Fondazione CRT (2019-1887 and 2020-0719). This study was supported by grants to R.O. from the European Research Council (ERC) (ERC Starting Grant 759532, X-TAM), AIRC (MFAG 20247, Bridge Grant 27844, and AIRC 5×1000 special program 22737), and the Italian Ministry of Health (GR-201602362156, GR-2021-12374094). Research in the R.O. laboratory is supported by grants from the Italian Telethon Foundation (SR-Tiget Grant Award F04).

Author contributions N.C., F.L.T., F.M.V. and G.B. contributed to the design of the study, analysed data, prepared figures and edited the manuscript. N.C. and F.M.V. performed or contributed to all experiments, with help from L.M., S. Barresi, E.M., E.D., A.C., M.S.F.N., S. Brugiapaglia, A.S. and P. Cappello. F.L.T. and G.B. performed all computational analyses, with help from C.L. and E.L. V. Cuzzola and M.G. performed spatial gene expression experiments, with help from M.S.L. and C.D. M.P. and P. Canevazzi performed spheroid and organoid culture experiments. G.D. performed lineage tracing experiments. D.D. and A.A. performed mass spectrometry analyses. S.C. and M.F. selected and recruited study participants. A. Mortellaro, V. Corbo, Z.L. and A. Mondino provided resources. P.D., L.P., C.T., F.N., M.I., L.G.N., F.G., C.B. and L.N. provided key scientific inputs. R.O. conceptualized and coordinated the study, acquired funding, analysed the data and wrote the paper. All authors read and edited the manuscript.

Competing interests The authors declare no competing interests.

Additional information

Supplementary information The online version contains supplementary material available at https://doi.org/10.1038/s41586-023-06685-2.

Correspondence and requests for materials should be addressed to Nicoletta Caronni or Renato Ostuni.

Peer review information *Nature* thanks Cecilia Garlanda, Elvira Mass and the other, anonymous, reviewer(s) for their contribution to the peer review of this work. Peer review reports are available.

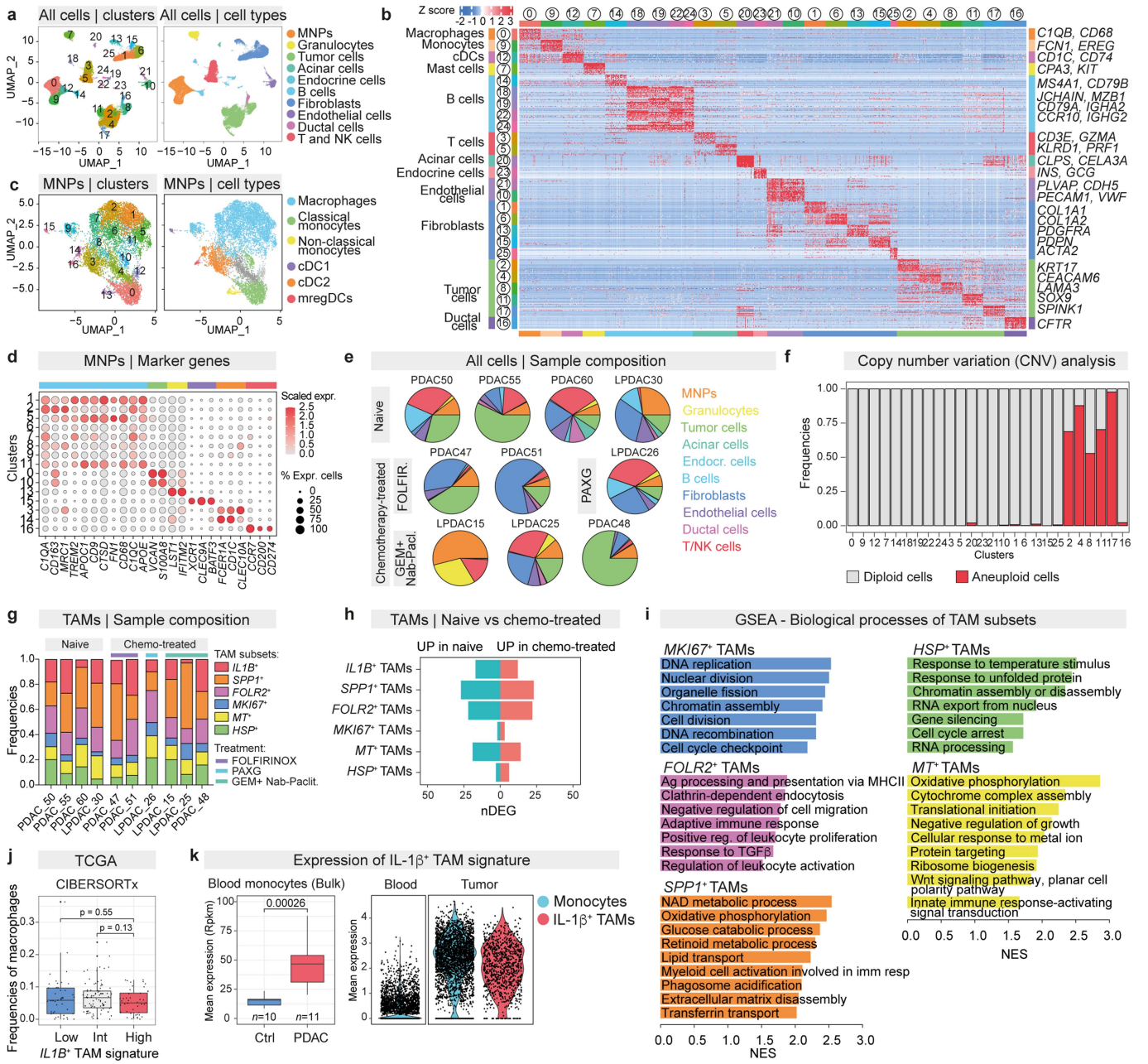

Extended Data Fig. 1 | scRNA-seq analyses of PDAC patients. a, UMAP of scRNA-Seq of all cells from PDAC patients. Colors and numbers indicate scRNA-Seq clusters (left) or cell type annotations (right). **b**, Heatmap of scaled expression of top 25 marker genes for each scRNA-Seq cluster. Selected transcripts are indicated. **c**, UMAP of scRNA-Seq of mononuclear phagocytes (MNPs) from PDAC patients. Colors and numbers indicate scRNA-Seq clusters (left) or cell type annotations (right). **d**, Dot plot of scaled expression of selected marker genes for each MNP cluster. **e**, Relative abundance (scRNA-Seq) of the indicated cell types for individual naïve or chemotherapy-treated PDAC patients. GEM+Nab-Pacl., gemcitabine+Nab-paclitaxel; FOLFIR., FOLFIRINOX; PAXG, cisplatin+Nab-paclitaxel, capecitabine, gemcitabine. **f**, Frequencies of diploid or aneuploid cells for each cluster, as predicted by copy number variation (CNV) analysis with CopyKAT. **g**, Frequencies of TAM subsets (scRNA-Seq) for individual naïve or chemotherapy-treated PDAC patients. GEM+Nab-Pacl., gemcitabine+Nab-paclitaxel; FOLFIR., FOLFIRINOX; PAXG, cisplatin+Nab-paclitaxel, capecitabine, gemcitabine. **h**, Number of differentially expressed genes (DEGs) in TAM subsets between chemotherapy-treated and naïve PDAC patients. **i)** GSEA (Gene Ontologies biological processes, GO BP) on genes ranked by $\log_2$FC between each TAM subset versus other TAMs. NES, Normalized Enrichment Score. **j**, Calculated frequencies of macrophages (CIBERSORTx deconvolution) in TCGA PDAC patients stratified according to expression levels of the *IL1B*$^+$ TAM gene signature. Significance is computed by two-sided Mann-Whitney test. The box extends from the lower to upper quartile values of the data, with a line at the median. The whiskers extend from the box to show the range of the data no further than 1.5 * IQR (Inter-quartile range) from the hinges. **k**, Mean expression of the *IL1B*$^+$ TAM gene signature in blood monocytes (bulk RNA-Seq) from healthy donors (Ctrl, n = 10) and PDAC patients (left, n = 11), and in blood or tumor monocytes or IL-1β$^+$ TAMs from PDAC patients (right). Significance is computed by two-sided Mann-Whitney test. Sample size is indicated. The box extends from the lower to upper quartile values of the data, with a line at the median. The whiskers extend from the box to show the range of the data no further than 1.5 * IQR (Inter-quartile range) from the hinges.

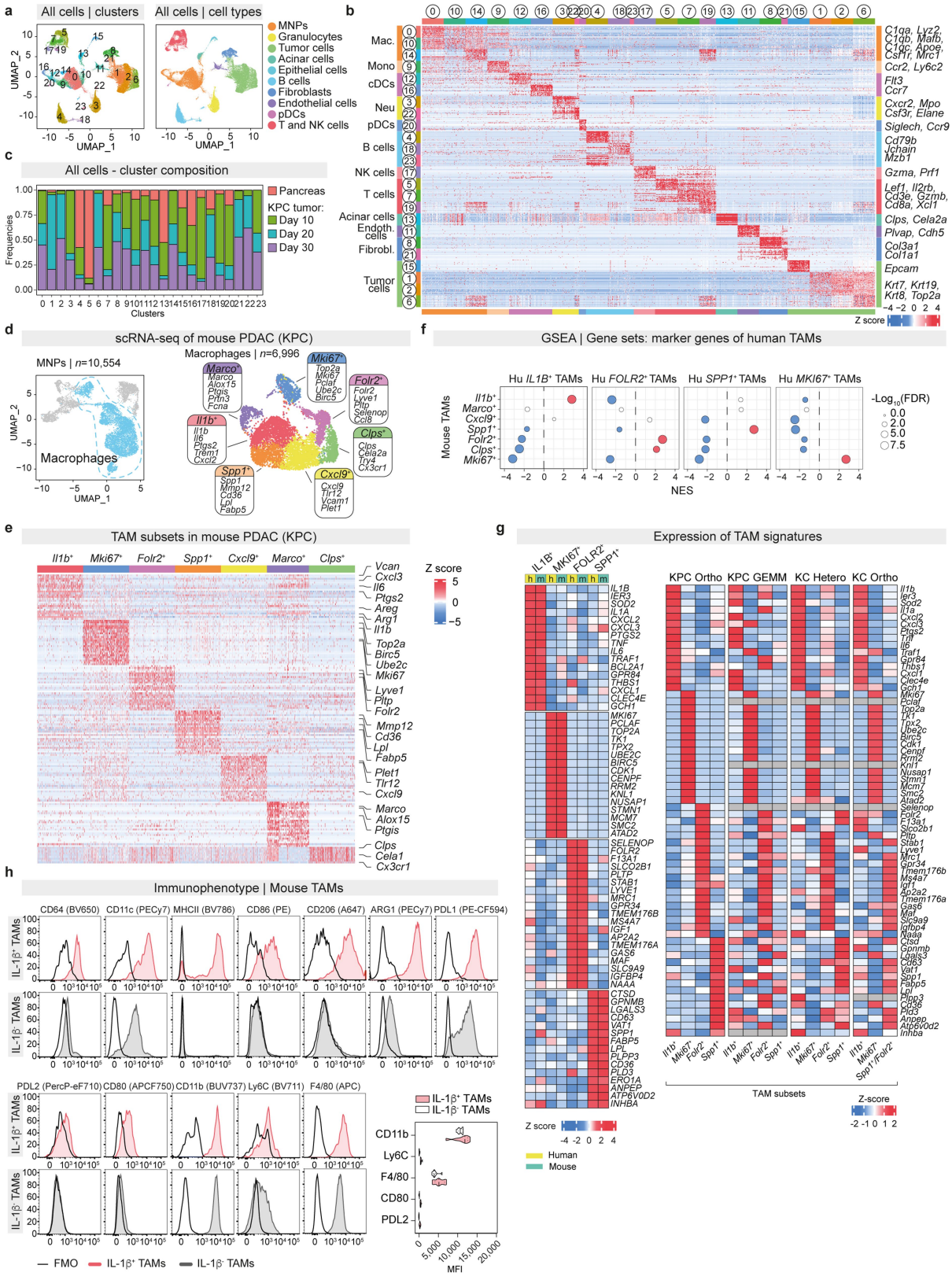

Extended Data Fig. 2 | See next page for caption.

Extended Data Fig. 2 | scRNA-seq analyses of mouse PDAC models. a, UMAP of scRNA-Seq of all cells from mouse PDAC (orthotopic KPC). Colors and numbers indicate scRNA-Seq clusters (left) or cell type annotations (right). **b**, Heatmap of scaled expression of top 25 marker genes for each scRNA-Seq cluster. Selected transcripts are indicated. **c**, Frequencies (scRNA-Seq) of cells from the indicated experimental conditions and time points in each cluster. **d**, UMAP of scRNA-Seq of mononuclear phagocytes (MNPs) (left) or macrophages (right) from mouse PDAC (orthotopic KPC). **e**, Heatmap of scaled expression of top 25 marker genes for each mouse TAM subset. Selected transcripts are indicated. **f**, GSEA (marker genes of human TAM subsets) on genes ranked by log_2FC between each mouse TAM subset versus other TAMs. NES, Normalized Enrichment Score. **g**, Heatmap of scaled gene expression of species-conserved marker genes in human or mouse TAM subsets (left), or in mouse TAM subsets from the indicated PDAC models (right). Only clusters of TAMs conserved between species are reported. **h**, Expression (flow cytometry) of the indicated markers (CD11b, Ly6C and F4/80, n = 8; CD80 and PD-L2, n = 27) by IL-1β$^+$ TAMs (red) and IL-1β$^-$ TAMs (grey). Representative histograms and median fluorescence intensity (MFI) values are shown. Black lines represent fluorescence minus one control (FMO).

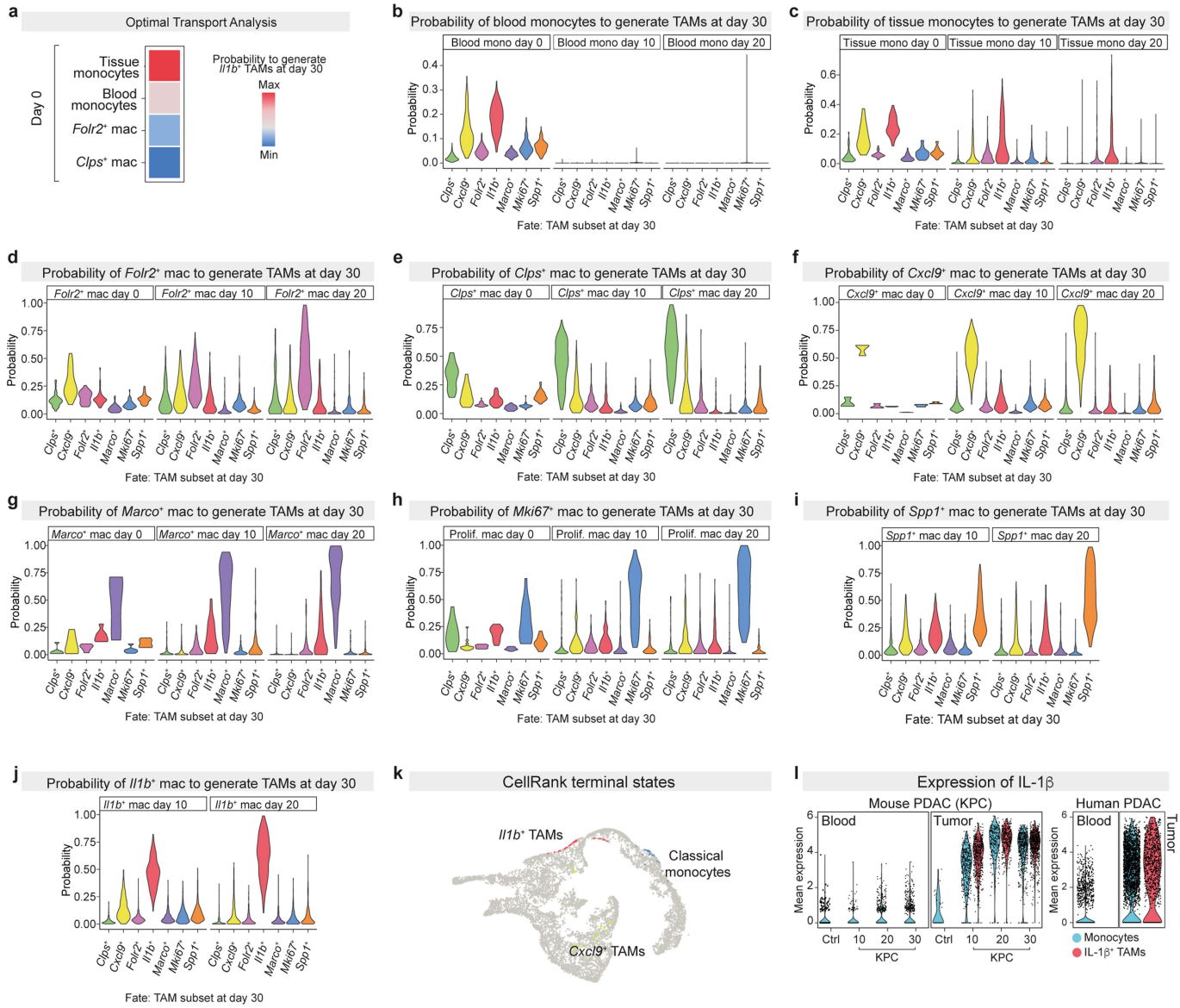

Extended Data Fig. 3 | Ontogeny of IL-1β$^+$ TAMs. a, Scaled mean fate probabilities (Optimal Transport Analysis, OTA) to acquire IL-1β$^+$ TAM identity (at day 30) for the indicated cell populations in mouse PDAC (orthotopic KPC). **b-j**, Fate probabilities (OTA) to acquire the transcriptional programs of the indicated TAM subsets in mouse PDAC (orthotopic KPC) by blood monocytes (**b**), tissue monocytes (**c**), *Folr2*$^+$ macrophages (**d**), *Clps*$^+$ macrophages (**e**), *Cxcl9*$^+$ macrophages (**f**), *Marco*$^+$ macrophages (**g**), *Mki67*$^+$ macrophages (**h**), *Spp1*$^+$ TAMs (**i**) and *Il1b*$^+$ TAMs (**j**). Probability values are shown for all time points. **k**, Cells identified as terminal states (CellRank) in tSNE embedding of mouse macrophages and monocytes from tissue and blood samples. **i**, Mean expression (scRNA-Seq) of *Il1b* in monocytes and IL-1β$^+$ TAMs from control pancreas (Ctrl) and PDAC (orthotopic KPC) at the indicated time points (left), or in human monocytes and IL-1β$^+$ TAMs from blood and tumor samples of PDAC patients (right).

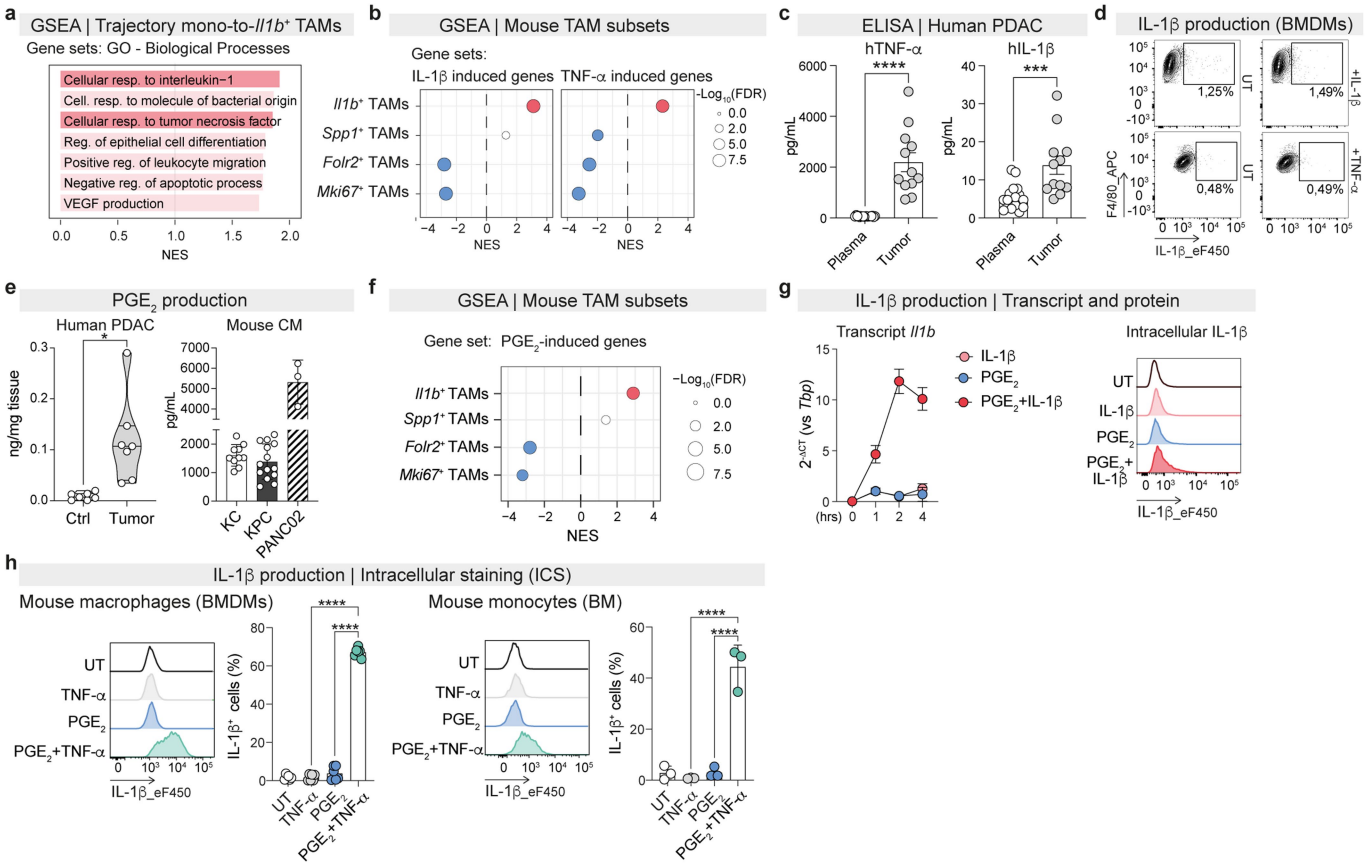

Extended Data Fig. 4 | Elicitation of the IL-1β$^+$ TAM state by PGE$_2$ and TNF-α. **a**, GSEA (GO BP) on genes ranked by correlation with absorption probability of the monocyte-to-*Il1b*$^+$ TAM transition. Selected terms are shown. **b**, GSEA on genes ranked by log$_2$FC between each mouse TAM subset versus other TAMs. Gene sets: IL-1β-induced or TNF-α-induced genes. NES, Normalized Enrichment Score. **c**, Concentration (mean ± SEM) of TNF-α (n = 18) and IL-1β (n = 17) in plasma and tumor of PDAC patients (n = 12). ***p < 0.001 ****p < 0.0001 (unpaired student's two-tailed t test). **d**, Expression of IL-1β (intracellular staining) in mouse BMDMs treated for 6 h with IL-1β or TNF-α. **e**, Quantification of PGE$_2$ in human PDAC samples and control (Ctrl) matched normal adjacent tissue (n = 7/group) by mass spectrometry (left), or in culture supernatants of KPC (n = 14), KC (n = 10) and PANC02 (n = 3) PDAC cells by ELISA (mean±SD, right). *p < 0.05 (paired student's two-tailed t test). **f**, GSEA (PGE$_2$-induced genes) on genes ranked by log$_2$FC between each mouse TAM subset versus other TAMs (orthotopic KPC). NES, Normalized Enrichment Score. **g**, Transcript (mean ± SD, left) or protein (intracellular staining, right) expression of IL-1β in BMDMs stimulated as indicated (n = 2). **h**, Expression (intracellular staining) of IL-1β in BMDMs (n = 6, left) or BM monocytes (n = 3, right) stimulated as indicated. ****p < 0.0001 (one-way ANOVA).

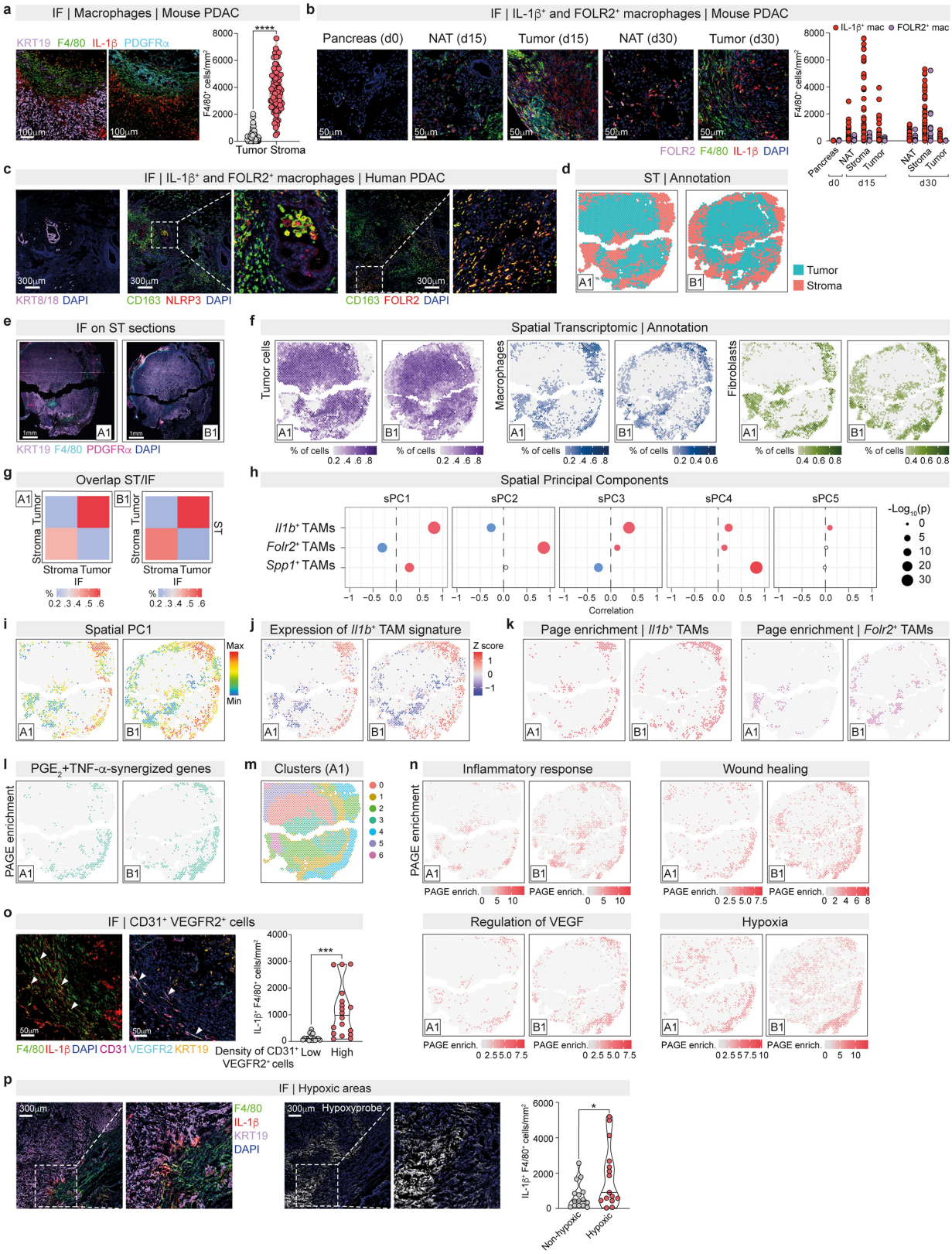

Extended Data Fig. 5 | See next page for caption.

Extended Data Fig. 5 | Spatial distribution of IL-1β$^+$ TAMs. a, Left panels. Selected regions of interest showing signal intensity (IF staining) of KRT19 (tumor cells), F4/80 (macrophages), PDGFR-α (fibroblasts) and IL-1β in mouse PDAC (orthotopic KPC, end-stage). Right panels. Quantification of macrophages (cells/mm^2) in stromal or tumor areas (n = 2 mice, n = 4 sections/mouse, n = 10 ROI/area). ****p < 0.0001 (unpaired student's two-tailed t test). **b**, Left panels. Selected regions of interest showing signal intensity (IF staining) of FOLR2, F4/80, IL-1β, and DAPI in control pancreas (day 0), mouse PDAC (orthotopic KPC), or normal adjacent tissue (NAT) at the indicated time points. Right panels. Quantification of IL-1β$^+$ and FOLR2$^+$ macrophages (cells/mm^2) in stromal, tumor areas or NAT areas. Ctrl pancreas, n = 2 mice, n = 2 sections/mouse, n = 10 ROI/section; Day 15 PDAC, n = 4 mice, n = 2 sections/mouse, n = 5 ROI/areas; Day 30 PDAC, n = 5 mice, n = 2 sections/mouse, n = 10 ROI/areas. **c**, Selected regions of interest with inset magnifications showing signal intensity (IF staining) of KRT8-18, CD163, NLRP3, and DAPI (middle), or CD163, FOLR2 and DAPI (right) on consecutive sections of human PDAC samples. **d**, Annotation (see Methods) of tumor or stromal areas in spatial transcriptomics data (Visium) for the indicated tissue sections of mouse PDAC (orthotopic KPC, end-stage). **e**, Signal intensity (IF staining) of KRT19, F4/80, PDGFR-α and DAPI for the indicated tissue sections of mouse PDAC (orthotopic KPC, end-stage). **f**, Percentages (DestVI deconvolution) of tumor cells (left), macrophages (middle) and fibroblasts (right) in spatial transcriptomics data (Visium) for the indicated tissue sections of mouse PDAC (orthotopic KPC, end-stage). **g**, Percentage of spots with concordant annotation as stroma or tumor by spatial transcriptomics (Visium) and IF staining for the indicated tissue sections of mouse PDAC (orthotopic KPC, end-stage). **h**, Correlation values (red, positive; blue, negative; white, non-significant) between mean gene expression (Visium) of marker genes of the indicated TAM subsets (DestVI generative model, see Methods) and spatial principal components (sPC) coordinates for spots of a selected tissue section (A1) of mouse PDAC (orthotopic KPC, end-stage). **i**, Coordinates of spatial Principal Component 1 (sPC1) of macrophage-enriched spots (DestVI deconvolution) in spatial transcriptomics data (Visium) for the indicated tissue sections of mouse PDAC (orthotopic KPC, end-stage). **j**, Scaled mean expression of marker genes of IL-1β$^+$ TAMs (DestVI generative model) in macrophage-enriched spots (DestVI deconvolution) in spatial transcriptomics data (Visium) for the indicated tissue sections of mouse PDAC (orthotopic KPC, end-stage). **k**, Enrichment (PAGE) of expression of marker genes of IL-1β$^+$ TAMs (left) or FOLR2$^+$ TAMs (right) in macrophage-enriched spots (DestVI deconvolution) in spatial transcriptomics data (Visium) for the indicated tissue sections of mouse PDAC (orthotopic KPC, end-stage). Colors indicate macrophage-enriched ST spots with significance (estimated on all spots) of p < 0.001. **l**, Enrichment (PAGE) of expression of PGE_2 + TNF-α synergized genes in macrophage-enriched spots (DestVI deconvolution) in spatial transcriptomics data (Visium) for the indicated tissue sections of mouse PDAC (orthotopic KPC, end-stage). Colors indicate macrophage-enriched ST spots with significance (estimated on all spots) of p < 0.001. **m**, Louvain clustering of spots in spatial transcriptomics data (Visium) for a selected tissue section (A1) of mouse PDAC (orthotopic KPC, end-stage). **n**, Enrichment (PAGE) of expression of genes belonging to the indicated GO BPs in spatial transcriptomics data (Visium) for the indicated tissue sections of mouse PDAC (orthotopic KPC, end-stage). GSEA was performed on genes ranked by log_2FC between cluster 4 versus other spots. Colors indicate spots with significance (estimated on all spots) of p < 0.001. **o**, Signal intensity (IF staining) of F4/80, IL-1β, and DAPI (left), or of CD31, VEGFR2 and KRT19 (middle) in consecutive sections of mouse PDAC (orthotopic KPC, end-stage). Arrows indicate IL-1β$^+$ F4/80$^+$ cells (left) and CD31$^+$ VEGFR2$^+$ cells (middle). Quantification of IL-1β$^+$ F4/80$^+$ cells in areas with high and low density of CD31$^+$ VEGFR2$^+$ cells (right, n = 5 mice, n = 2 sections/mouse). ***p < 0.001 (unpaired student's two tailed t test). **p**, Signal intensity (IF staining) of F4/80, IL-1β and KRT19 (left), or of anti-Hypoxyprobe (middle) in consecutive sections of mouse PDAC (orthotopic KPC, end-stage). Quantification of IL-1β$^+$ F4/80$^+$ cells in hypoxic and non-hypoxic areas (right, n = 3 mice, n = 2 sections/mouse). *p < 0.05 (unpaired student's two tailed t test).

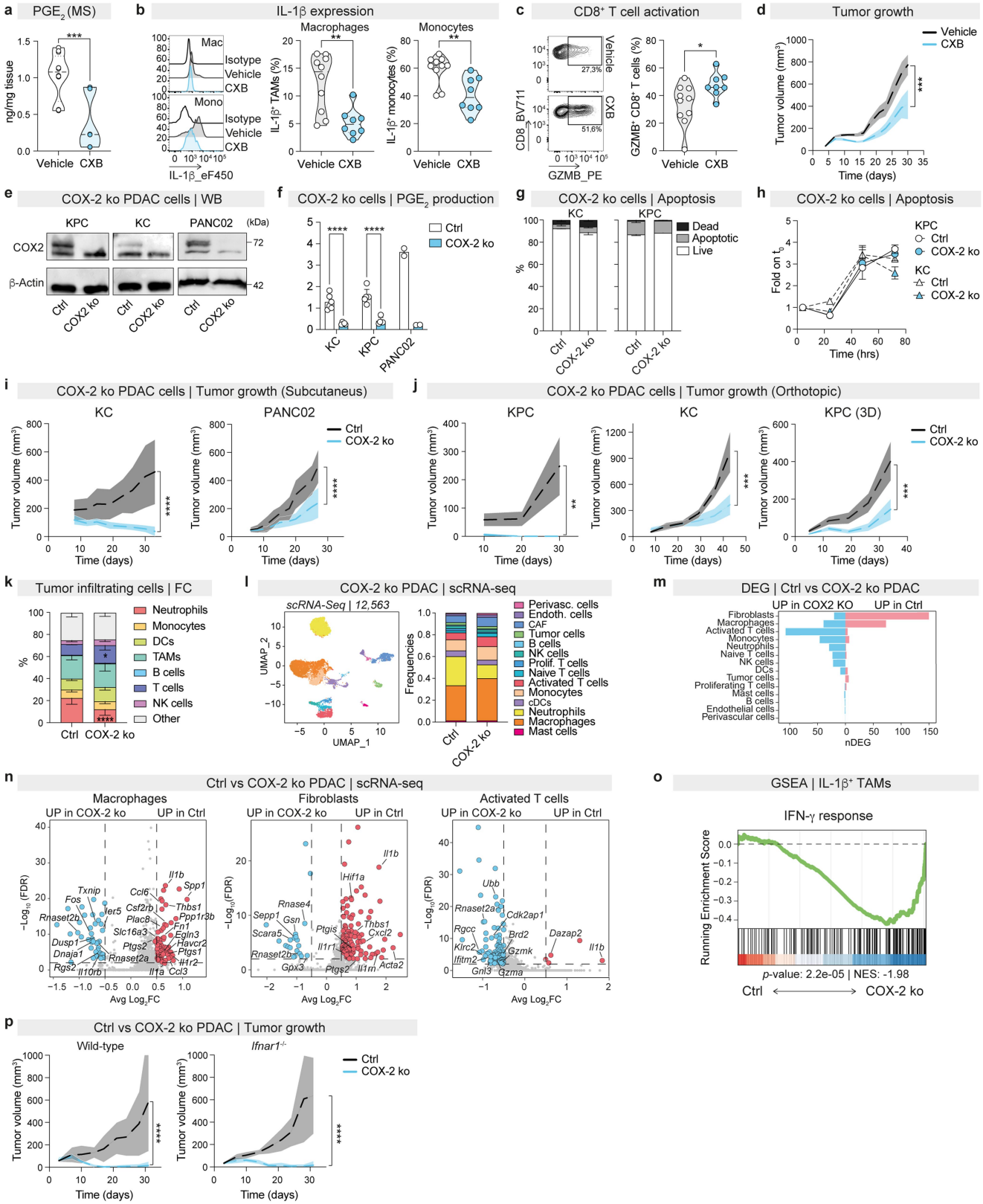

Extended Data Fig. 6 | See next page for caption.

Extended Data Fig. 6 | Targeting PGE_2 reprograms the pancreatic TME. **a**, Quantification of PGE_2 (mass spectrometry) in lysates of mouse PDAC (subcutaneous KPC, end-stage) from mice treated with celecoxib (CXB, n = 3) or vehicle (n = 4). ***p < 0.001 (unpaired student's two tailed t test). **b**, Expression of IL-1β (intracellular staining) in macrophages and monocytes in mouse PDAC (subcutaneous KPC, end-stage) from mice treated with celecoxib (CXB, n = 8) or vehicle (n = 10). **p < 0.01 (unpaired t test). **c**, Contour plots (left) and frequency (right) of $GZMB^+$ $CD8^+$ T cells in mouse PDAC (subcutaneous KPC, end-stage) from mice treated with celecoxib (CXB, n = 8) or vehicle (n = 10). *p < 0.05 (unpaired student's two tailed t test). **d**, Growth curves (mean±SEM) of mouse PDAC (subcutaneous KPC) in mice treated with celecoxib (CXB, n = 10) or vehicle (n = 10). ***p < 0.001 (two-way ANOVA). **e**, Expression (western blot) of COX-2 and β-Actin in the indicated control and COX-2 ko mouse PDAC cell lines. **f**, Quantification of PGE_2 (ELISA, mean±SD) in the culture supernatant of the indicated control (KC, n = 6; KPC, n = 6; PANC02, n = 2) and COX-2 KO (KC, n = 5; KPC, n = 5; PANC02, n = 2) mouse PDAC cell lines. ****p < 0.0001 (2-way ANOVA). **g**, Expression (mean±SD) of Annexin V and/or 7AAD cells by the indicated control (n = 2) and COX-2 ko (n = 2) mouse PDAC cells. **h**, Proliferation in vitro (WST-1 assay, mean±SEM) of the indicated control (n = 2) and COX-2 ko (n = 2) mouse PDAC cells. **i**, Growth curves (mean±SD) of control (subcutaneous KC, n = 8; subcutaneous PANC02, n = 10) and COX-2 ko PDAC cells (subcutaneous KC, n = 10; subcutaneous PANC02, n = 7) in wild-type mice. ****p < 0.0001 (two-way ANOVA). **j**, Growth curves (mean ± SEM) of control (Ctrl) and COX-2 ko PDAC cells (orthotopic KPC, n = 5/group, left; orthotopic KC, n = 4/group, middle) or spheroids (3D, orthotopic KPC, n = 9/group, right) in wild-type mice. **p < 0.01, ***p < 0.001 (two-way ANOVA). **k**, Frequencies (flow cytometry) of the indicated cell types in control or COX-2 ko PDAC (subcutaneous KPC, day 6, n = 5/group). *p < 0.05, ****p < 0.0001 (two-way ANOVA). **l**, UMAP showing clustering (left) and bar plots showing frequencies (right, scRNA-Seq) of the indicated cell types in control or COX-2 ko PDAC (subcutaneous KPC, day 7). **m**, Number of differentially expressed genes (DEG, scRNA-Seq) for the indicated cell types between control and COX-2 ko PDAC (subcutaneous KPC, day 7). **n**, Volcano plots of differentially expressed genes for macrophages (left), fibroblasts (middle) and activated T cells (right) between control (Ctrl) and COX-2 ko PDAC (subcutaneous KPC, day 7). Selected genes for each population are highlighted. FC, fold change. FDR, false discovery rate. **o**, GSEA (IFN-γ response genes,) on genes ranked by log_2FC between $IL\text{-}1\beta^+$ TAMs from control (Ctrl) versus COX-2 ko PDAC (subcutaneous KPC, day 7). NES, Normalized Enrichment Score. **p**, Growth curves (mean ± SD) of control (Ctrl) and COX-2 ko PDAC cells (subcutaneous KPC) in wild-type mice (n = 4 Ctrl, n = 5 COX-2 ko, left) or *Ifnar1*$^{-/-}$ (n = 5 Ctrl, n = 5 COX-2 ko, right) mice. ****p < 0.0001 (two-way ANOVA).

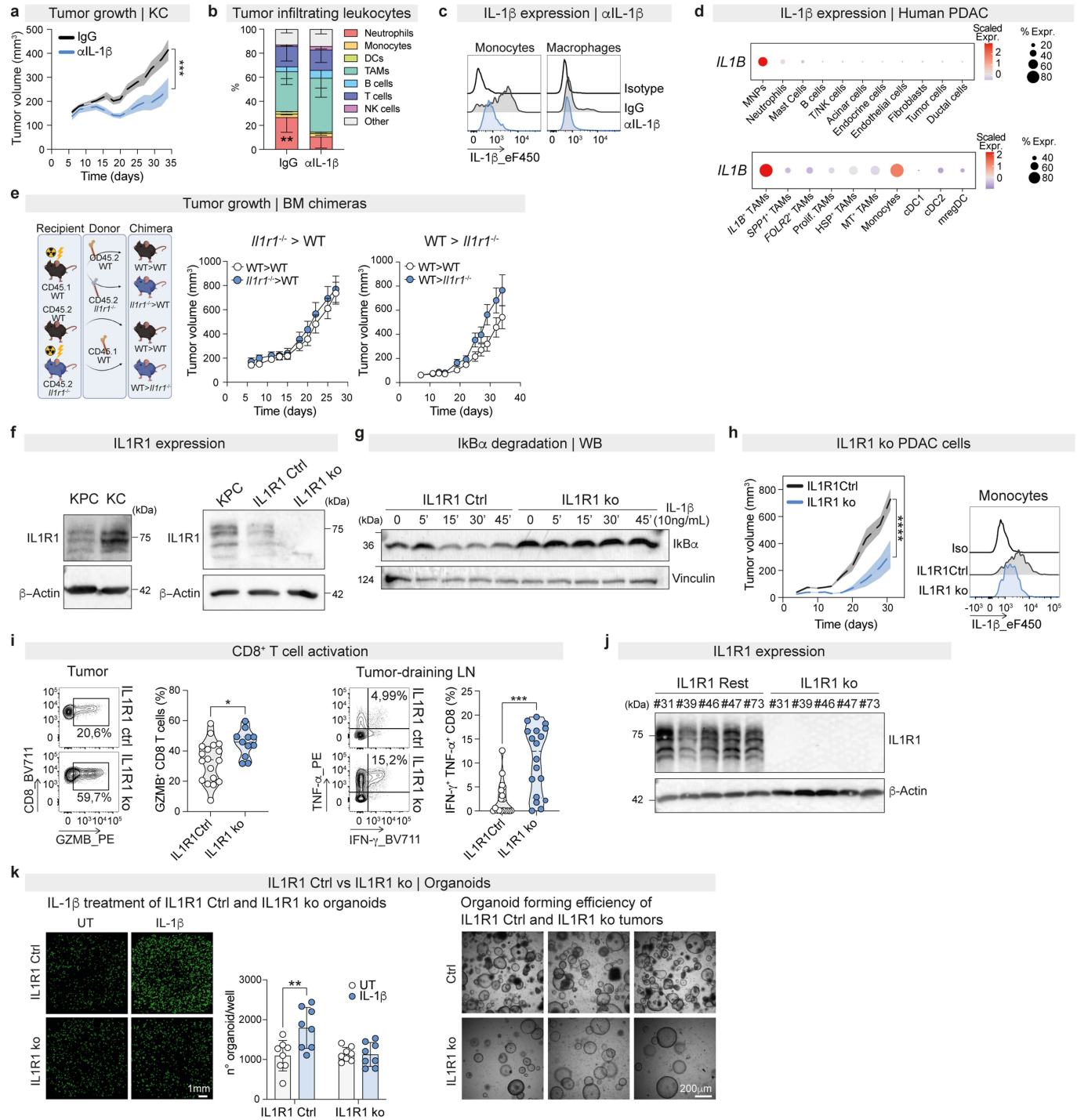

Extended Data Fig. 7 | See next page for caption.

Extended Data Fig. 7 | Tumor cell-intrinsic IL-1β signaling promotes PDAC growth. a, Growth curves (mean±SEM) of PDAC cells (subcutaneous KC) in mice treated with anti-IL-1β (n = 8) or isotype control (IgG, n = 10). ***p < 0.001 (two-way ANOVA). **b**, Frequencies (flow cytometry, mean±SD) of the indicated cell types in PDAC (subcutaneous KPC, end-stage) of mice treated with anti-IL-1β (n = 7) or isotype control (IgG, n = 10). **p < 0.01 (two-way ANOVA). **c**, Expression of IL-1β (intracellular staining) in monocytes (left) or macrophages (right) in PDAC (subcutaneous KPC, end-stage) of mice treated with anti-IL-1β or isotype control (IgG). **d**, Dot plots of scaled *IL1B* expression (scRNA-Seq) in the indicated cell populations (top) or myeloid cell subsets (bottom) in human PDAC samples. **e**, Schematic representation (left) and growth curves (mean ± SEM) of PDAC (subcutaneous KPC) in the indicated bone marrow (BM) chimeric mice (n = 10 WT > WT, *Il1r1*$^{-/-}$>WT; n = 11 WT> *Il1r1*$^{-/-}$) (two-way ANOVA). **f**, Expression of IL-1R1 and β-actin (western blot) in whole cell lysates of the indicated parental, control (Ctrl) or IL-1R1 ko PDAC cells. **g**, Expression of IκBα (western blot) in whole cell lysates of control or IL-1R1 ko PDAC cells (KPC) upon stimulation with IL-1β for the indicated time points. **h**, Growth curves of tumors (mean ± SEM, right) and expression of IL-1β in tumor-infiltrating monocytes (intracellular staining, right) from control (Ctrl) or IL1-R1 ko PDAC (subcutaneous KPC, n = 8/group). ****p < 0.0001 (two-way ANOVA). **i**, Contour plots (left) and frequencies (right) of activated CD8$^+$ T cells in tumors (subcutaneous KPC, n = 18 Ctrl, n = 11 IL-1R1 ko, left) or tumor-draining lymph nodes (subcutaneous KPC, n = 18 Ctrl, n = 18 IL-1R1 ko, right) from control (Ctrl) or IL1-R1 ko PDAC. ***p < 0.001, * p < 0.05 (unpaired student's two-tailed t test). **j**, Expression of IL-1R1 and β-actin (western blot) in whole cell lysates of IL-1R1 ko or IL-1R1-reconstituted IL-1R1 ko (IL1R1 Rest) PDAC (KPC) cells. Numbers denote clone ID. **k**, Representative images (left) and quantification (mean ± SD, middle) of organoids generated from control (Ctrl) and IL-1R1 ko PDAC cells (KPC) treated with vehicle or with IL-1β for 5 days (n = 8 wells/condition; the entire Matrigel area was collected for each well). **p < 0.01 (2-way ANOVA). Representative images (right) of organoids generated from explanted control (Ctrl) and IL-1R1 ko PDAC (subcutaneous KPC, day 11).

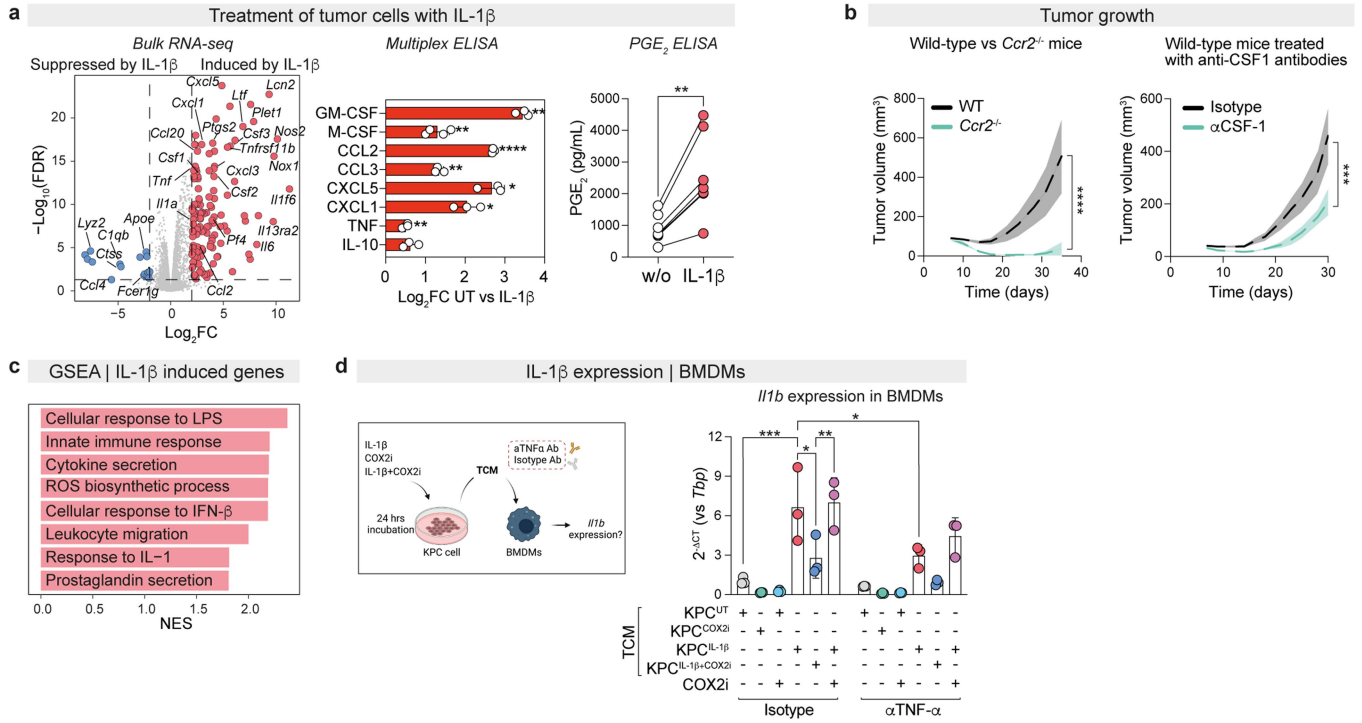

Extended Data Fig. 8 | Consequences of IL-1β signaling in tumor cells. **a**, Volcano plot (left) of genes up-regulated (red) or down-regulated (blue) in PDAC (KPC) cells treated with IL-1β for 24 h (UT n = 3, IL-1β n = 2). Selected genes are highlighted. Quantification (ELISA) of the indicated cytokines (mean ± SD, n = 3, unpaired two-tailed student's t test, middle) or PGE_2 (n = 7, paired two-tailed student's t test, right) in the supernatant of PDAC cells (KPC) cells treated with IL-1β 24 h. *p < 0.5, **p < 0.01, ****p < 0.0001. **b**, Growth curves (mean±SEM) of PDAC cells (subcutaneous KPC) in wild-type and *Ccr2*$^{-/-}$ mice (left, n = 5/group) or in wild-type mice treated with an anti-CSF-1 antibody (αCSF-1, n = 8) or isotype control (IgG, n = 10). ****p < 0.0001 (two-way ANOVA). **c**, GSEA (GO BP) on genes ranked by log_2FC between PDAC cells (KPC) treated with IL-1β versus untreated controls. NES, Normalized Enrichment Score. **d**, Scheme of the experiment (left) and expression of *Il1b* (RT-qPCR, mean±SD) in BMDMs treated for 2 h with tumor-conditioned media (TCM) of mouse PDAC cells (KPC) from the following conditions: untreated (KPC^{UT}) or treated for 24 h with a COX-2 inhibitor (KPC^{COX2i}), IL-1β ($KPC^{IL\text{-}1\beta}$), IL-1β + COX-2 inhibitor ($KPC^{IL\text{-}1\beta+COX2i}$). A control condition of BMDMs stimulated with vehicle or COX-2 inhibitor (COX2i) is shown. Isotype control or an anti-TNF-α antibody (αTNF-α) groups were included for each condition (n = 3). *p < 0.05 **p < 0.01 ***p < 0.001 (two-way ANOVA).

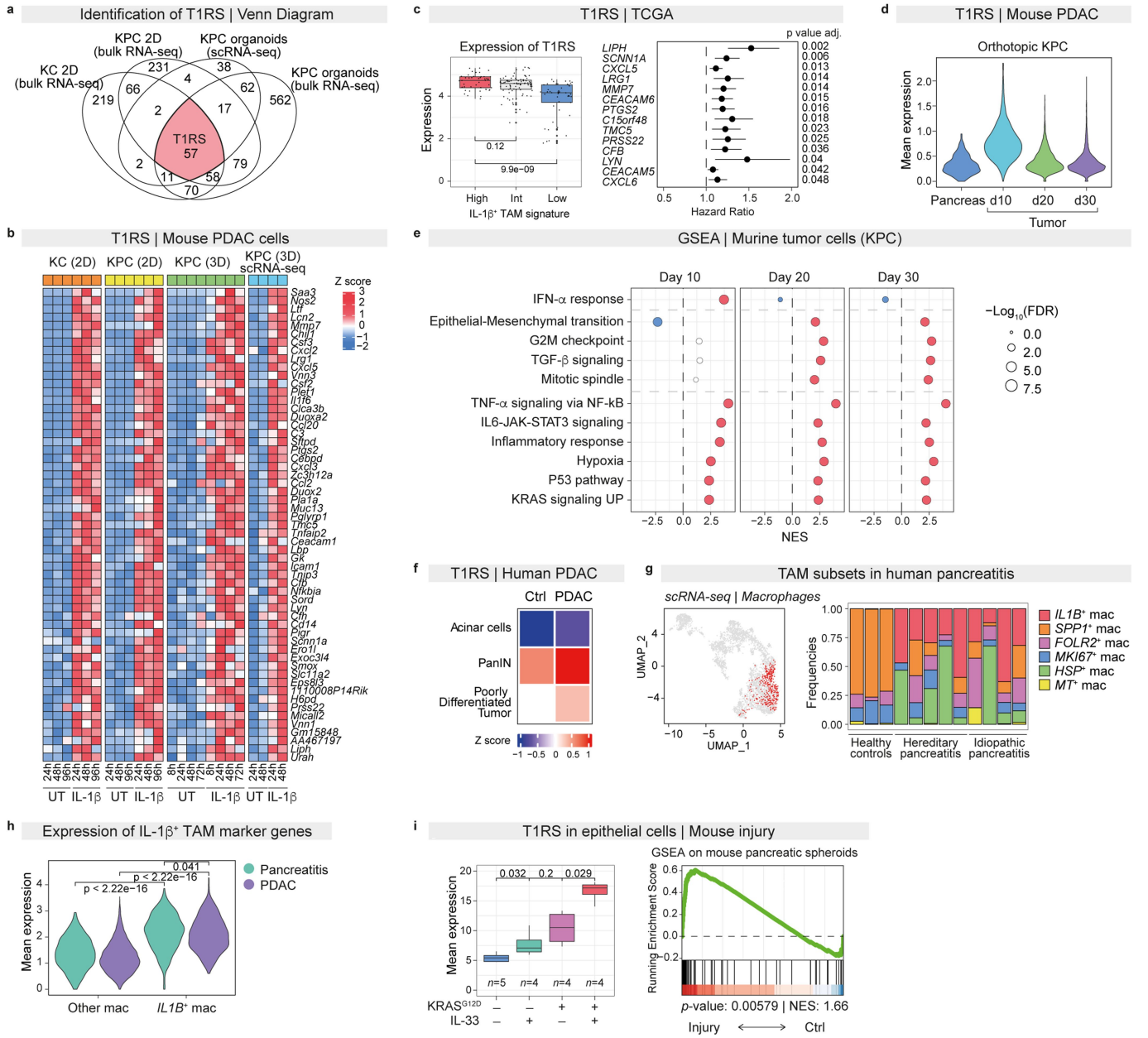

Extended Data Fig. 9 | Inflammatory reprogramming of PDAC cells. **a**, Venn diagram of genes up-regulated (bulk RNA-Seq or scRNA-Seq) upon treatment with IL-1β in the indicated mouse PDAC models. The tumor-intrinsic IL-1β response signature (T1RS) is composed by the 57 genes commonly up-regulated by IL-1β in all conditions. **b**, Heatmap of scaled expression (bulk RNA-Seq or scRNA-Seq) of T1RS genes in the indicated mouse PDAC models, left untreated or stimulated with IL-1β for the indicated time points. **c**, Mean expression of human orthologs of T1RS genes (TCGA) in PDAC patients stratified for the levels of expression of the *IL1B*$^+$ TAM signature (left). The box extends from the lower to upper quartile values of the data, with a line at the median. The whiskers extend from the box to show the range of the data no further than 1.5 * IQR (Inter-quartile range) from the hinges. Hazard ratios (right) obtained by fitting univariate Cox model on gene expression of T1RS genes in TCGA PDAC cohort. Only genes with significant adjusted p-values are reported. **d**, Mean expression (scRNA-Seq) of T1RS genes in pancreatic epithelial cells and tumor cells from control pancreas or mouse PDAC (orthotopic KPC) in the indicated time points. **e**, GSEA (MSigDB hallmark genes) on genes ranked by $\log_2$FC between tumor versus healthy pancreas cells at the indicated time points (orthotopic KPC). NES, Normalized Enrichment Score. FDR, False Discovery Rate. **f**, Heatmap of scaled mean expression (GeoMx) of human orthologs of T1RS genes in the indicated regions of interest (ROIs) of healthy donors and PDAC patients. PanIN, pancreatic intraepithelial neoplasia. **g**, UMAP (left) and frequencies (scRNA-Seq, right) of the indicated macrophage subsets in the pancreas of healthy controls or patient with hereditary or idiopathic pancreatitis). Cells corresponding to IL-1β$^+$ TAMs are annotated in red. **h**, Mean expression (scRNA-Seq) of IL-1β$^+$ TAM marker genes in IL-1β$^+$ TAMs (or other TAMs) from PDAC patients and in macrophages corresponding to IL-1β$^+$ TAMs (or other macrophages) in pancreatitis patients. Significance is computed by two-sided Mann-Whitney test. **i**, Left, mean expression of T1RS genes in pancreatic epithelial cells from mice control or mutated *Kras* and treated with vehicle or IL-33. Significance (two-sided Mann-Whitney test) is shown. Sample size is indicated. The box extends from the lower to upper quartile values of the data, with a line at the median. The whiskers extend from the box to show the range of the data no further than 1.5 * IQR (Inter-quartile range) from the hinges. Right, GSEA (T1RS genes) on genes ranked by $\log_2$FC between spheroids generated from injured or control pancreas. NES, Normalized Enrichment Score.

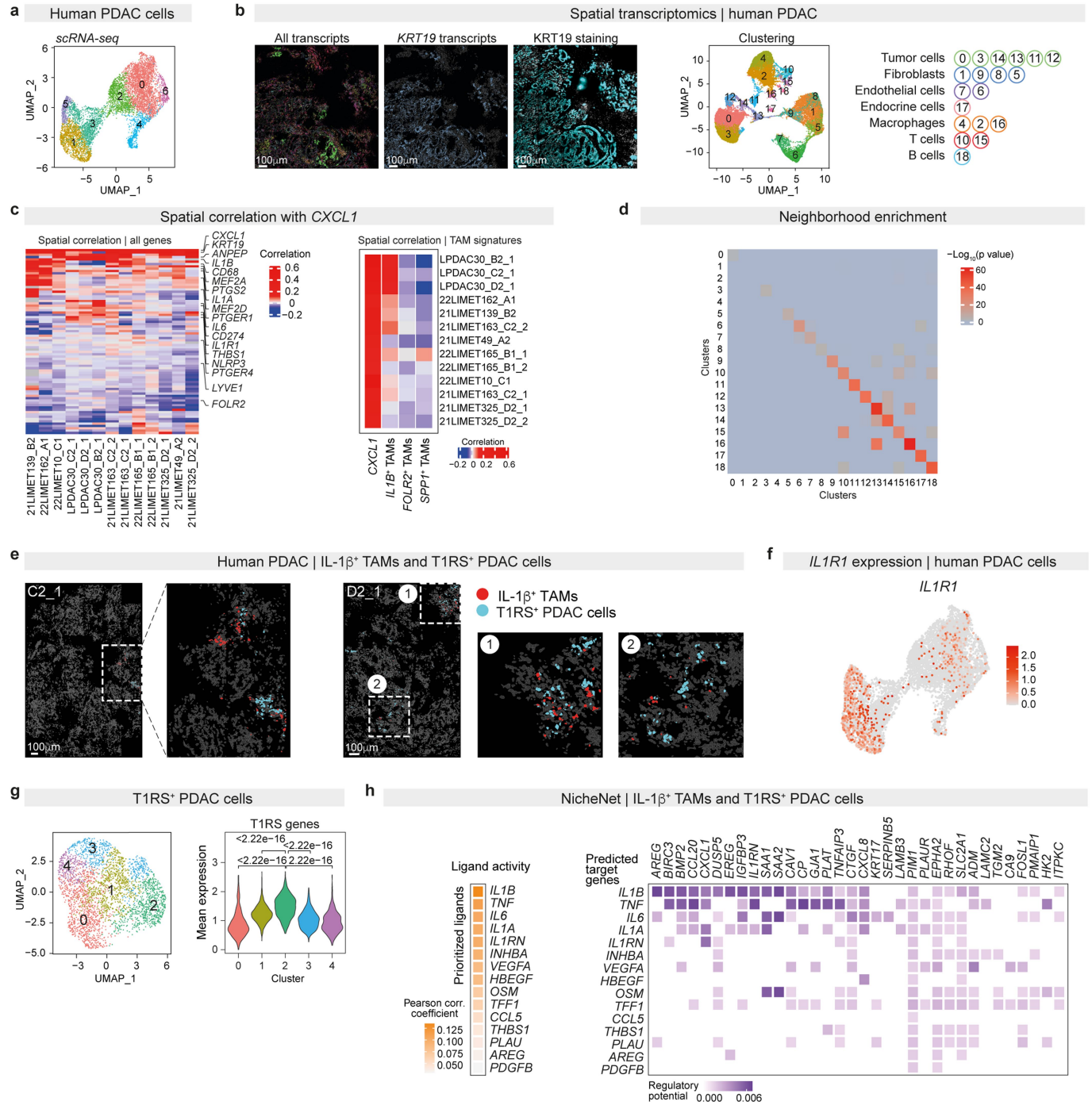

Extended Data Fig. 10 | Spatial analyses of IL-1β$^+$ TAMs and T1RS$^+$ PDAC cells. a, UMAP plot of scRNA-Seq data of PDAC cells from chemotherapy-naïve patients. Colors and numbers indicate cluster identity. **b**, Left panels. Selected region of interest (LPDAC30 B2_1) showing expression (Molecular Cartography) of all (563,761) detected transcripts or *KRT19*, as well as signal intensity (IF staining) of KRT19. Right panels. UMAP of spatial gene expression data (Molecular Cartography) of cells from all sections collected from patient LPDAC30. Colors and numbers indicate cluster identity and corresponding annotations. **c**, Heatmaps of spatial correlation of gene expression (see Methods) with *CXCL1* of genes of the spatial transcriptome panel (left) or of marker genes of TAM subsets (right). **d**, Heatmap of spatial neighborhood significance between the indicated clusters (see Methods). **e**, Selected regions of interest (LPDAC30 C2_1, left. LPDAC30 D2_1, right) showing co-localization of IL-1β$^+$ TAMs (red) and T1RS$^+$ PDAC cells (light blue) in spatial gene expression analyses. Numbers indicate insets and their magnifications. **f**, UMAP showing expression (scRNA-Seq) of IL1R1 in PDAC cells from chemotherapy-naïve patients. **g**, UMAP of scRNA-Seq data (left) and violin plot showing mean expression of T1RS genes (right) of PDAC cells selected for pseudotime analysis. Colors and numbers indicate cluster identity. Significance is computed by two-sided Mann-Whitney test. **h**, Heatmaps (NicheNet) of ligand activity (Pearson correlation coefficient) of top-ranking ligands expressed by IL-1β$^+$ TAMs (left) and their regulatory potential on predicted target genes expressed by T1RS$^+$ PDAC cells (right).

nature portfolio

Corresponding author(s): Renato Ostuni
Nicoletta Caronni

Last updated by author(s): Sep 13, 2023

Reporting Summary

Nature Portfolio wishes to improve the reproducibility of the work that we publish. This form provides structure for consistency and transparency in reporting. For further information on Nature Portfolio policies, see our Editorial Policies and the Editorial Policy Checklist.

Statistics

For all statistical analyses, confirm that the following items are present in the figure legend, table legend, main text, or Methods section.

n/a	Confirmed	
☐	☒	The exact sample size (*n*) for each experimental group/condition, given as a discrete number and unit of measurement
☐	☒	A statement on whether measurements were taken from distinct samples or whether the same sample was measured repeatedly
☐	☒	The statistical test(s) used AND whether they are one- or two-sided *Only common tests should be described solely by name; describe more complex techniques in the Methods section.*
☒	☐	A description of all covariates tested
☐	☒	A description of any assumptions or corrections, such as tests of normality and adjustment for multiple comparisons
☐	☒	A full description of the statistical parameters including central tendency (e.g. means) or other basic estimates (e.g. regression coefficient) AND variation (e.g. standard deviation) or associated estimates of uncertainty (e.g. confidence intervals)
☐	☒	For null hypothesis testing, the test statistic (e.g. *F*, *t*, *r*) with confidence intervals, effect sizes, degrees of freedom and *P* value noted *Give P values as exact values whenever suitable.*
☒	☐	For Bayesian analysis, information on the choice of priors and Markov chain Monte Carlo settings
☒	☐	For hierarchical and complex designs, identification of the appropriate level for tests and full reporting of outcomes
☒	☐	Estimates of effect sizes (e.g. Cohen's *d*, Pearson's *r*), indicating how they were calculated

Our web collection on statistics for biologists contains articles on many of the points above.

Software and code

Policy information about availability of computer code

Data collection	Flow cytometry data were collected at: BD FACSymphony A5 SORP Cytometer or FACS Canto II (BD Bioscience) using DIVA software v.8.0.2 (BD Bioscience). Immunofluorescence images were acquired on a MAVIG RS-G4 scanning confocal microscope (Caliber I.D.) or FluoVIEW 3000 RS (Olympus). ELISA multiplex assay data were collected using the Luminex xMAP system (Biorad). Bulk and single-cell RNA-Sequencing libraries were sequenced on NovaSeq6000 instruments (Illumina). Molecular Cartography oligonucleotides probes were designed using Resolve Biosciences proprietary algorithm. Probe binding was revealed with fluorescent tags in a multi-step automated imaging process on a Zeiss Celldiscoverer 7 instrument.
Data analysis	Flow cytometry data were analyzed with FlowJo (Treestar) version v10.8.1. Quantitative analysis of immunofluorescence images was performed using QuPath v0.4.1 or Machine Learning Tool of the Arivis Vision 4D software (ZeissAG). Western Blot analyses were performed using Image Lab software, version v6.1. ELISA multiplex assay results were analysed with Bio-plex Manager software (Biorad). Bulk RNA-Seq data were aligned with STAR v2.5.3a and further analyzed in R environment (v 3.6.3). sc-RNA-Seq data were pre-processed with Cell Ranger v4 (10X Genomics) and further analysed with Seurat package (v4.2.0) in R environment (v4.0.3). Spatial transcriptomic data were pre-processed with Space Ranger (v1.2.0, 10x Genomics) and further analyzed in R environment (v4.0.3). For Molecular Cartography data, cell segmentation was performed using Cellpose (v. 2.2) and Baysor (v. 0.5.0). Detailed description of computation methods is provided in Methods section. Statistical analysis was conducted either using GraphPad Prism v9.0 (GraphPad Software) or R v3.4.1 (R project).

Codes used for the analyses are available at: https://github.com/ostunilab/PDAC_Nature_2023.

For manuscripts utilizing custom algorithms or software that are central to the research but not yet described in published literature, software must be made available to editors and reviewers. We strongly encourage code deposition in a community repository (e.g. GitHub). See the Nature Portfolio guidelines for submitting code & software for further information.

Data

Policy information about availability of data

All manuscripts must include a data availability statement. This statement should provide the following information, where applicable:

- Accession codes, unique identifiers, or web links for publicly available datasets
- A description of any restrictions on data availability
- For clinical datasets or third party data, please ensure that the statement adheres to our policy

Data Availability Single-cell, Spatial Transcriptomic and bulk RNA-seq data have been deposited at NCBI GEO data repository under the accession number GSE217847, https://www.ncbi.nlm.nih.gov/geo/query/acc.cgi?acc=GSE217847. Data reanalyzed for this study are available under the following accession codes: CRA001160, https://ngdc.cncb.ac.cn/gsa/browse/CRA001160 (scRNA-Seq of human PDAC and NAT); GSE165045, https://www.ncbi.nlm.nih.gov/geo/query/acc.cgi?acc=GSE165045 (scRNA-Seq of pancreatitis patients); GSE207943, https://www.ncbi.nlm.nih.gov/geo/query/acc.cgi?acc=GSE207943 (scRNA-Seq of mouse PDAC GEMM); GSE226829, https://www.ncbi.nlm.nih.gov/geo/query/acc.cgi?acc=GSE226829 (GeoMX data of human PDAC); GSE132326, https://www.ncbi.nlm.nih.gov/geo/query/acc.cgi?acc=GSE132326 and GSE154543, https://www.ncbi.nlm.nih.gov/geo/query/acc.cgi?acc=GSE154543 (RNA-Seq of epithelial cells from mouse PDAC); GSE180211, https://www.ncbi.nlm.nih.gov/geo/query/acc.cgi?acc=GSE180211 (RNA-Seq of pancreatic spheroids); E-MTAB-11190, https://www.ebi.ac.uk/biostudies/arrayexpress/studies/E-MTAB-11190 (RNA-Seq of blood monocytes from PDAC patients).

Human research participants

Policy information about studies involving human research participants and Sex and Gender in Research.

Reporting on sex and gender	Age and sex of enrolled participants are reported in Supplementary Table 1.
Population characteristics	We collected different demographic and clinical informations. Age and sex, as well as anonymized clinical information of enrolled participants are reported in Supplementary Tables 1.
Recruitment	Participant were recruited by the Department of Pancreatic Surgery at Ospedale San Raffaele (Milano, Italy), between July 2020 and May 2022. Patients with primary PDAC tumors that are candidates for surgical resection with radical intent of the primary tumor (upfront surgery or after neoadjuvant therapy) have been enrolled.
Ethics oversight	Collection of biological samples was compliant to the Declaration of Helsinki and to the General Data Protection Regulation and it was approved by Ospedale San Raffaele ethic committee. Informed consent was obtained from all study participants Protocols: NEU-IPMN; LIMET.

Note that full information on the approval of the study protocol must also be provided in the manuscript.

Field-specific reporting

Please select the one below that is the best fit for your research. If you are not sure, read the appropriate sections before making your selection.

☒ Life sciences ☐ Behavioural & social sciences ☐ Ecological, evolutionary & environmental sciences

For a reference copy of the document with all sections, see nature.com/documents/nr-reporting-summary-flat.pdf

Life sciences study design

All studies must disclose on these points even when the disclosure is negative.

Sample size	No statistical method was used to predetermine sample size. Sample sizes were estimated based on preliminary experiments, with an effort to achieve a minimum of n=3, mostly n=8 mice per treatment group, which proved sufficient to determine reproducible results.
Data exclusions	No data were excluded from the analysis. Datasets used for the specific analyses are reported in the Methods section.
Replication	The number of replicates for each experiment is indicated in figure legends. All experiments were repeated multiple times in different cohorts as stated in the individual figure legends. Key observations from RNA-Seq studies have been validated with independent methods.
Randomization	Mice were allocated randomly to the experimental groups.
Blinding	Blinding was used to measure tumor growth curves, both when using electronic caliper and ultrasound analysis and for immunofluorescence

Blinding

analysis. For the other experiments, for instance flow cytometry, RT-qPCR, ELISA and sequencing experiments that are based on objective measurements, blinding was not required.

Reporting for specific materials, systems and methods

We require information from authors about some types of materials, experimental systems and methods used in many studies. Here, indicate whether each material, system or method listed is relevant to your study. If you are not sure if a list item applies to your research, read the appropriate section before selecting a response.

Materials & experimental systems

n/a	Involved in the study
☐	☒ Antibodies
☐	☒ Eukaryotic cell lines
☒	☐ Palaeontology and archaeology
☐	☒ Animals and other organisms
☒	☐ Clinical data
☒	☐ Dual use research of concern

Methods

n/a	Involved in the study
☒	☐ ChIP-seq
☐	☒ Flow cytometry
☒	☐ MRI-based neuroimaging

Antibodies

Antibodies used

Antibodies for flow-cytometry:
Rat anti-mouse Arginase 1 Monoclonal Antibody (A1exF5), PE-Cyanine7; eBioscience, Thermo Fischer Scientific; Cat# 25-3697-82; 1:300
Hamster anti-mouse CD3e Monoclonal Antibody (145-2C11), BV650; BD Bioscience; Cat# 564378; 1:100
Hamster anti-mouse CD3e Monoclonal Antibody (145-1C11), APC; BioLegend; Cat# 100312; 1:100
Rat anti-mouse CD4 Monoclonal Antibody (GK1.5), PE-Cyanine7; eBioscience, Thermo Fischer Scientific; Cat# 25-0041-82; 1:300
Rat anti-mouse CD8a Monoclonal Antibody (53-6.7), FITC; BD Bioscience; Cat# 553030; 1:200
Rat anti-mouse CD8a Monoclonal Antibody (53-6.7), BV711; BD Bioscience; Ca# 563046; 1:100
Rat anti mouse CD11b Monoclonal Antibody (M1/70), BUV737; BD Bioscience; Cat# 612801; 1:200
Rat anti mouse CD11b Monoclonal Antibody (M1/70), APC; BioLegend; Cat# 101212; 1:200
Hamster anti-mouse CD11c Monoclonal Antibody (N418), PE-Cyanine7; eBioscience, Thermo Fischer Scientific; Cat# 25-0114-82; 1:200
Hamster anti-mouse CD11c Monoclonal Antibody (N418), BUV395; BD Bioscience; Cat# 744180; 1:200
Rat anti mouse CD16/CD32 Monoclonal Antibody (93), TruStain FcX; BioLegend; Cat# 101320; 1:100
Rat anti-mouse CD19 Monoclonal Antibody (6D5), FITC; BioLegend; Cat# 115505; 1:200
Rat anti-mouse CD19 Monoclonal Antibody (6D5), PE; BioLegend; Cat# 115508; 1:200
Rat anti-mouse CD45 Monoclonal Antibody (30-F11), FITC; BD Bioscience; Cat# 553079; 1:200
Rat anti-mouse CD45 Monoclonal Antibody (30-F11), PerCP-Cyanine5.5; eBioscience, Thermo Fischer Scientific; Cat# 45-0451-80; 1:200
Rat anti-mouse CD45 Monoclonal Antibody (30-F11), BUV395; BD Bioscience; Cat# 564279; 1:100
Mouse anti-mouse CD45.1 Monoclonal Antibody (A20), BV650; BioLegend; Cat# 110735; 1:100
Mouse anti-mouse CD45.2 Monoclonal Antibody (104), BV786; BD Bioscience; Cat# 563686; 1:100
Mouse anti-mouse CD45.2 Monoclonal Antibody (104), BUV737; BD Bioscience; Cat# 612778; 1:100
Mouse anti-mouse CD64 Monoclonal Antibody (X54-5/7.1), BV650; BD Bioscience; Cat# 740622; 1:100
Hamster anti-mouse CD80 Monoclonal Antibody (16-10A1), APC/Fire 750; BioLegend; Cat# 104740; 1:100
Rat anti-mouse CD86 Monoclonal Antibody (GL1), PE; eBioscience, Thermo Fischer Scientific; Cat# 12-0862-82; 1:100
Rat anti-mouse CD115 (CSF-1R) Monoclonal Antibody (AFS98), PE/Dazzle 594; BioLegend; Cat# 135528; 1:100
Rat anti-mouse CD206 (MMR) Monoclonal Antibody (C068C2), Alexa Fluor 647; BioLegend; Cat# 141712; 1:200
Rat anti-mouse CD273 (PDL2) Monoclonal Antibody (122), PerCP-eFluor710; eBioscience, Thermo Fischer Scientific; Cat# 46-9972-82; 1:100
Rat anti-mouse CD274 (PDL1) Monoclonal Antibody (MIH5), PE-CF594; BD Bioscience; Cat# 567032; 1:100
Rat anti-mouse F4/80 Monoclonal Antibody (BM8), APC; eBioscience, Thermo Fischer Scientific; Cat# 17480182; 1:50
Rat anti-mouse F4/80 Monoclonal Antibody (BM8), PE; eBioscience, Thermo Fischer Scientific; Cat# 12480182; 1:50
Rat anti-mouse I-A/I-E (MHCII) Monoclonal Antibody (M5/114.15.2), BV785; BioLegend; Cat# 107645; 1:400
Mouse anti-human Granzyme B Monoclonal Antibody (GB12), PE; Thermo Fischer Scientific; Cat# MHGB04; 1:50
Rat anti-mouse IFNg Monoclonal Antibody (XMG1.2), BV711; BioLegend; Cat# 505836; 1:100
Rat anti-mouse IL1b (Pro-Form) Monoclonal Antibody (NJTEN3), eFluor450; eBioscience, Thermo Fischer Scientific; Cat# 48-7114-82; 1:100
Rat IgG1 kappa Isotype Control (eBRG1), eFluor450; eBioscience, Thermo Fischer Scientific; Cat# 48-4301-82; 1:100
Rat anti-mouse Ly6C Monoclonal Antibody (HK1.4), BV711; BioLegend; Cat# 128037; 1:500
Rat anti-mouse Ly6C Monoclonal Antibody (HK1.4), APC-eFluor 780; BioLegend; Cat# 47-5932-82; 1:200
Rat anti-mouse Ly6G Monoclonal Antibody (1A8), FITC; BD Bioscience; Cat# 561105; 1:200
Rat anti-mouse Ly6G Monoclonal Antibody (1A8), APC-Cyanine7; BioLegend; Cat# 127624; 1:200
Mouse anti-mouse NK1.1 Monoclonal Antibody (PK136), BV785; BioLegend; Cat# 108749; 1:100
Mouse anti-mouse NK1.1 Monoclonal Antibody (PK136), BUV395; BD Bioscience; Cat# 564144; 1:100
Rat anti-mouse Siglec-F Monoclonal Antibody (E50-2440), PerCP-Cyanine5.5; BD Bioscience; Cat# 565526; 1:100
Rat anti-mouse TNFa Monoclonal Antibody (MP6-XT22), PE; BioLegend; Cat# 506306; 1:100
Mouse anti-human CD45 Monoclonal Antibody (HI30), PE; BioLegend; Cat# 304008; 1:200
Mouse anti-human CD19 Monoclonal Antibody (HIB19), BV510; BioLegend; Cat# 302242; 1:50

Mouse anti-human CD3 Monoclonal Antibody (OKT3), BV510; BioLegend; Cat# 317332; 1:100

Depleting/blocking antibodies:
InVivoMAb anti-mouse NK1.1 (PK136); BioXcell; Cat# BE0036
InVivoMAb mouse IgG2a isotype control (C1.18.4); BioXcell; Cat# BE0085
Ultra-LEAF Purified anti-Asialo-GM-1 (Poly21460); BioLegend; Cat#146002
InVivoMAb anti-mouse CSF1 (5A1); BioXCell; Cat# BE0204
InVivoMAb rat IgG1 isotype control, anti-horseradish peroxidase (HRPN); BioXcell; Cat# BE0088
InVivoMAb anti-mouse/rat IL-1β (B122); BioXCell; Cat# BE0246
InVivoMAb polyclonal Armenian hamster IgG; BioXCell; Cat# BE0091
InVivoMAb anti mouse CD8a (2.43); BioXCell; Cat# BE0061
InVivoMAb rat IgG2b isotype control (LTF-2); BioXCell; Cat# BE0090

Antibodies for Western Blot analysis:
Rabbit anti-IKappaB-alpha (L35A5) Polyclonal Antibody; Cell Signaling Technology; Cat# 9242S; 1:1000
Mouse anti-beta-Actin Monoclonal Antibody (AC-15), Unconjugated; Sigma-Aldrich; Cat# A1978; 1:1000
Rabbit anti-Vinculin Monoclonal Antibody (E1E9V); Cell Signaling Technology; Cat# 13901; 1:1000
Rabbit anti-IL1R1 Monoclonal Antibody (EPR22198-36); Abcam; Cat# ab229051; 1:1000
Rabbit anti-Cox2 Polyclonal Antibody (aa 570-598); Cayman Chemical; Cat# 160106; 1:200

Antibodies for immunofluorescence and immunohistochemistry:
Rat anti F4/80 Monoclonal Antibody (C1:A3-1); Abcam; Cat# ab6640; 1.200
Rabbit anti F4/80 Monoclonal Antibody (EPR26545-166); Abcam; Cat# ab300421; 1:500
Rabbit anti Cytokeratin 19 Monoclonal Antibody (EP1580Y); Abcam; Cat# ab52625; 1:1000
Goat anti IL-1b Polyclonal Antibody; R&D System; Cat# AF-401-NA; 1:100
Rat anti FOLR2 (10/FR2); BioLegend; Cat# 153302; 1:100
Goat anti CD31 Polyclonal Antibody; R&D Systems; Cat# AF3628; 1:500
Rat anti VEGFR2 (Avas 12a1); BD Pharmingen; Cat# 550549; 1:100
Rabbit anti PDGFRα (EPR22059-270); Abcam; Cat# ab203491; 1:500
Rabbit anti-pimonidazole; Hypoxyprobe; Cat# PAb2627AP; 1:20
Donkey anti-Rat IgG (H+L) Highly Cross-Adsorbed Secondary Antibody, Alexa Fluor™ Plus 488; Thermo Fisher Scientific; Cat# A48269; 1:500
Donkey anti-Goat IgG (H+L) Highly Cross-Adsorbed Secondary Antibody, Alexa Fluor™ Plus 555; Thermo Fisher Scientific; Cat# A32816; 1:500
Donkey anti-Rabbit IgG (H+L) Highly Cross-Adsorbed Secondary Antibody, Alexa Fluor™ Plus 647; Thermo Fisher Scientific; Cat# A32795; 1:500
Rabbit anti-human NLRP3 Polyclonal Antibody; Sigma-Aldrich Merck; Cat# HPA012878; 1:150
Mouse anti-human CD163 (MRQ-26); Cell Marque; 163M-18, pre-diluted
Mouse anti-human FOLR2 (OTI4G6); Invitrogen; Cat# MA5-26933; 1:100
Mouse anti-human Cytokeratin 8 (B22.1) & 18 (B23.1); Cell Marque; 818M-90, pre-diluted

Validation

All antibodies for flow cytometry used in this study were purchased from BD Bioscience, BioLegend or Thermo Fischer Scientific. All antibodies used are suitable for flow-cytometric analyses and were characterized and validated by providers. These indications are available on the manufacturer's websites (https://www.biolegend.com/en-us/quality/quality-control; https://www.bdbiosciences.com/en-us/products/reagents/flow-cytometry-reagents/research-reagents/quality-and-reproducibility). Blocking antibodies were previously validated by the vendor. For the depletion experiments, we assessed depletion of target populations by flow cytometry staining of circulating and tumor-infiltrating cells.
For IF and IHC stainings negative controls (isotype and secondary antibody staining) were performed.

Eukaryotic cell lines

Policy information about cell lines and Sex and Gender in Research

Cell line source(s)	KPC (K8484), KC (DT6606) and Panc02 cell lines were kindly provided by Lorenzo Piemonti (PMID: 19460966, PMID: 14706336, PMID: 6692374). KPC cell line was established from a tumor-bearing female animal; KC cell line was established from a male tumor-bearing mouse; Panc02 was established from a chemically-induced tumor-bearing male mouse.
Authentication	KC, KPC and Panc02 cells were generated as described in (PMID: 19460966, PMID: 14706336, PMID: 6692374) and not authenticated.
Mycoplasma contamination	All cell lines were routinely tested and were negative for Mycoplasma
Commonly misidentified lines (See ICLAC register)	No commonly misidentified lines were used in the study

Animals and other research organisms

Policy information about studies involving animals; ARRIVE guidelines recommended for reporting animal research, and Sex and Gender in Research

Laboratory animals	These strains were used in the study: C57BL/6N (Charles River); Ly5.1 (Charles River); IFNAR KO (Jackson Laboratories, kindly provided by Matteo Iannacone); IL1R1 KO (Jackson catalog, kindly provided by Cecilia Garlanda); CCR2 KO (Jackson Laboratories, kindly provided by Matteo Iannacone); Ms4a3Cre-RosaTdT (Florent Ginhoux). Mice at 8-12 weeks of age were used in the study. Animals were maintained in Specific pathogen-free (SPF) animal research facilities with a 12h/12h dark/light cycle and standardized temperature (22 +/- 2°C) and humidity (55 +/- 5%).
Wild animals	The study did not involve wild animals
Reporting on sex	In this study, both male and female animals were used. In particular, KPC cell lines were inoculated in C57BL/6N female animals, KC and Panc02 cells in C57BL/6N male mice.
Field-collected samples	No field-collected samples are included
Ethics oversight	All experiments and procedures were performed according to protocols approved by the Institutional Animal Care and Use Committee (IACUC) at San Raffaele Scientific Institute animal facilities and authorized by the Italian Ministry of Health in accordance with the Italian Laws (D.L.vo 116/92), which enforce the EU 86/609 Directive (approval number #449/2018-PR; #962/2020-PR and #908/2021-PR).

Note that full information on the approval of the study protocol must also be provided in the manuscript.

Flow Cytometry

Plots

Confirm that:

☒ The axis labels state the marker and fluorochrome used (e.g. CD4-FITC).

☒ The axis scales are clearly visible. Include numbers along axes only for bottom left plot of group (a 'group' is an analysis of identical markers).

☒ All plots are contour plots with outliers or pseudocolor plots.

☒ A numerical value for number of cells or percentage (with statistics) is provided.

Methodology

Sample preparation	Human and murine PB samples were incubated with Red Blood Cell (RBC) lysis buffer (Biolegend) for 10 minutes on ice and washed with Phosphate Buffered Saline (PBS). Cells were centrifuged for 5 minutes at 450 x g and resuspended in the appropriate buffer for down-stream application. Freshly resected human PDAC samples were minced in small pieces and digested with the Tumor Dissociation kit, human (Miltenyi Biotec). Similarly, murine healthy pancreas and tumors were manually minced in small pieces and dissociated with the Tumor Dissociation kit, mouse (Miltenyi Biotec) following manufacturer's instructions. The obtained single cells suspensions were filtered on 70µm cell strainers, incubated with RBC lysis buffer for 10 minutes on ice and resuspended in the appropriate buffer for cell counting and down-stream application. In selected experiments, murine tumor-draining lymph nodes were smashed, filtered through a 70µm cell strainers, and resuspended in the appropriate buffer for down-stream application. For the collection of plasma samples, an aliquot of 300µl of blood collected into EDTA tubes was centrifuged 5 min at 10,000 x g. Plasma was transferred into a clean tube and re-centrifuged 5min at 10,000 x g. Plasma samples were frozen and stored at −80°C until use. Supernatants of human PDAC and normal adjacent tissues were generated by culturing weighted tissues (1 to 30mg) in 1mL of complete media in a 48 well-plate. After 48 hours, supernatants were collected, centrifuged for 5 minutes at 450 x g to remove cellular debris and stored at -80°C for downstream analysis. For mass-spectrometry experiments, tissue samples were chopped, weighted and immediately snap-frozen at -80°C.
Instrument	Flow cytometry samples were analysed at BD FACSymphony A5 SORP Cytometer or FACS Canto II (BD Bioscience). For sorting experiments, cells were sorted at FACSAria Fusion (BD Bioscience) cell sorter.
Software	Data were collected with BD Diva software (BD Biosciences) and analyzed with FlowJo (Tree Star, Inc.) v 10.8.1
Cell population abundance	The purity of sorted samples was analyzed by flow cytometry on the same instruments used for sorting.
Gating strategy	Pancreas/Tumor Myeloid Cells: Neutrophils CD45+CD11b+Ly6G+CD11c-F4/80-; Monocytes CD45+CD11b+Ly6C+Ly6G-CD11c-F4/80-; Macrophages/TAMs SSChighCD45+Ly6G-CD11b+F4/80+CD64+. IL1b expression was analyzed within Monocytes and Macrophage/TAM gates. TAMs were separated in IL1b+ and IL1b-. IL1b+ and IL1b- TAMs have been analyzed for the expression of the following markers: Ly6C CD64 CD11c MHCII CD80 CD86 PDL1 PDL2 CD206 Arg1 Tumor Lymphoid Cells: Total T cells SSClowCD45+CD19-NK1.1-CD3+; CD4 T cells CD3+CD8-CD4+; CD8 T cells CD3+CD8+CD4-; B cells CD45+CD3-NK1.1-CD19+; NK cells CD45+CD3-CD19-NK1.1+. Granzyme B expression was evaluated in CD8 T cells.

Tumor Draining Lymph node:
Total T Cells SSClowNK1.1-CD3+; CD4 T cells CD3+CD8-CD4+; CD8 T cells CD3+CD8+CD4-; NK cells CD3-NK1.1+. IFNg and TNFa expression were analyzed within CD8 T cell gate.

Whole blood:
Monocytes CD11b+Ly6G-CD115+Ly6C+

Total Bone marrow stimulation:
Neutrophils CD45+CD11b+Ly6G+; Monocytes CD45+CD11b+Ly6G-Ly6C+. IL1b expression was analyzed within Monocytes.

BMDMs stimulation:
Macrophages F4/80+. IL1b expression was evaluated within Macrophages.

☒ Tick this box to confirm that a figure exemplifying the gating strategy is provided in the Supplementary Information.